

**An Investigation of the Efficacy of a Water-Cooled Chill in
Improving the As-Cast Structure of the Main Bearing Bulkhead in
A319 Engine Blocks**

by

Farzaneh Farhang Mehr

M.A.Sc., The University of British Columbia, 2012

A THESIS SUBMITTED IN PARTIAL FULFILLMENT OF THE
REQUIREMENTS FOR THE DEGREE OF

DOCTOR OF PHILOSOPHY

in

The Faculty of Graduate and Postdoctoral Studies

(Materials Engineering)

THE UNIVERSITY OF BRITISH COLUMBIA

(Vancouver)

December 2017

©Farzaneh Farhang Mehr, 2017

Abstract

In recent years, the automotive industry has been increasing the production of small, high-power gas engines as part of several strategies to achieve the new “Corporate Average Fuel Economy” (CAFE) standards, while at the same time meeting consumer demand for increased performance. This trend requires an improvement in the thermal and mechanical fatigue durability of the aluminium alloys used in the production of the cylinder heads and engine blocks in these engines. In the absence of modifying alloy chemistry, which potentially has significant implications for downstream operations such as heat treating and machining, one viable way to improve fatigue performance is to reduce the length-scales of the microstructural features arising from solidification that limit fatigue life. This, in turn, may be achieved by increasing the cooling rate during solidification (reducing the solidification time). Conventionally, solid chills are employed in industry to achieve this. A potential means of improving the efficacy of these chills is to incorporate water cooling. To assess the effectiveness of this method, a water-cooled chill was designed at UBC and installed in a bonded-sand engine block mould package (1/4 section). Twelve experiments were conducted with both a conventional solid chill and with a water-cooled chill (with and without a delay in water cooling). The moulds were instrumented with thermocouples to measure the evolution of temperature at key locations in the casting, and “Linear Variable Displacement Transducers” (LVDTs) to measure the gap size at the interface between the chill and the casting. A coupled thermal-stress mathematical model was developed in “ABAQUS 2016” to reproduce the experimental conditions and provide insight into interfacial heat transport and gap dynamics. Overall, the experimental and modelling results show the gap dynamics are complex and play a critical role in governing heat transport. If implemented carefully, the adoption of water-cooled chill technology has the potential to improve the cast microstructure, hence, increase the fatigue durability of the engine blocks.

Lay Summary

To reduce fuel consumption and meet environmental requirements, the automotive industry is aiming to increase the use of small, powerful engines. As an example, there are now several 2.0-litre turbocharged engines in production, producing in excess of 240 hp. To meet the need for improved material performance in the engine blocks used in these high-output engines, a new method of water-cooling part of the mould is under exploration at UBC in partnership with “General Motors Co.” and “Nemak Canada Ltd.”. A series of experimental and numerical techniques were used to assess the capability of the new method to extract heat from a critical area of an A319 aluminium alloy engine block. The results show that this method has the potential to improve the in-service life of the engine block; thus, meeting industry’s requirements.

Preface

This dissertation includes the original research work I have done to examine the efficacy of a water-cooled chill in refining the microstructural length scales of the new generation of engine blocks made with the precision sand casting process, which may lead to improvement of fatigue performance of the part. To complete this research work, I performed the following major steps:

1. Designed a water-cooled chill based on the geometry of the solid chill currently being used in the industry to increase the heat extraction capacity of the chill from the casting.
2. Conducted multiple casting experiments with the solid chill and the water-cooled chill to examine the efficacy of the water-cooled chill in increasing the cooling rate in the bulkhead region of the casting.
3. Performed metallography tests on the samples extracted from the castings to evaluate the effect of the change in the cooling rate on the length scales of the Secondary Dendrite Arm Spacings (SDAS).
4. Developed a coupled thermal-stress model to aid in understanding the thermal and displacement behaviour of the interface between the casting and the chill.

The following publications, which include some preliminary experimental and mathematical modelling analysis of this research, have been published/accepted in the conference proceedings so far [1,2]:

1. Farzaneh Farhang Mehr, Steven Cockcroft, Daan Maijer, Robert MacKay, Wade Marquardt, “Assessment of the Impact of Water-Cooled Chill Technology on Microstructure Length-Scales in an A319 Engine Block Casting”, COM2017 (accepted).
2. F. Farhang Mehr, S. Cockcroft, D. Maijer, “A Coupled Thermal-Stress Model of A319 Alloy Chilled Sand Casting”, Shape Casting 6th International Symposium, The Minerals, Metals, and Materials Society (February 2016).
3. F. Farhang Mehr, S. Cockcroft, C. Reilly, D. Maijer, “Evaluation of the Casting/Chill Interface Thermal Behaviour during A319 Alloy Sand Casting Process”, Advances in the Science and Engineering of Casting Solidification: An MPMD Symposium Honoring Doru Michael Stefanescu, John Wiley & Sons, Inc., (March 2015)

In all of these publications, I am the primary author and contributor. My supervisor, Professor Steve Cockcroft, provided continuing support and guidance in every aspect of my work and played a major editorial contribution in the above-mentioned publications.

Table of Contents

Abstract	ii
Lay Summary	iii
Preface.....	iv
Table of Contents	vi
List of Tables	ix
List of Figures	x
List of Symbols	xvi
Glossary	xviii
Acknowledgments.....	xix
Dedication	xxi
1. Introduction	1
2. Literature Review	5
2.1. Sand Casting	5
2.2. How to Improve Fatigue Performance of Cast Components.....	7
2.3. The Solidification Sequence and Factors Affecting the Solidification Structure of A319 Alloy	10
2.4. Chill Technology	13
2.5. Casting-Mould Interfacial Heat Transfer.....	14
2.6. Quantification of Casting-Mould Interfacial Heat Transfer Coefficient	16
3. Scope and Objective	22
4. Experimental Methodology.....	24

4.1.	GM Mould Package Thermocouple Setup	24
4.2.	Highland Mould Package Thermocouple Setup	26
4.3.	The Geometries of The Solid Chill and The Water-Cooled Chill	28
4.4.	LVDT Installation.....	30
4.5.	Liquid Metal Pouring Process	37
4.6.	Metallography Test.....	37
5.	Model Development	39
5.1.	Governing Equations	39
5.1.1.	Thermal Analysis Formulation	39
5.1.2.	Stress Analysis Formulation	40
5.1.3.	Coupled Thermal-Stress Analysis Formulation	43
5.2.	Preliminary Two-Dimensional Model Development	43
5.2.1.	Two-Dimensional Model Domain.....	44
5.2.2.	Initial Conditions	44
5.2.3.	Basic Symmetry Boundary Conditions Applied to the 2-D Model.....	45
5.2.4.	Material Properties.....	46
5.2.5.	Solution Technique and Mesh	50
5.2.6.	Two-Dimensional Model Results	51
5.3.	Three-Dimensional Model Development	64
5.3.1.	Three-Dimensional Model Domain.....	64
5.3.2.	Initial Conditions	65
5.3.3.	Boundary Conditions	66

5.3.4. Material Properties.....	77
5.3.5. Solution Technique and Mesh	77
6. Results and Discussion	78
6.1. Solid Chill Casting.....	78
6.2. Water-Cooled Chill Castings.....	89
6.3. Delayed Water-Cooled Chill Castings.....	99
6.4. The Effect of Water Cooling on Cooling Rate and Interface Gap Size.....	108
6.5. SDAS Size Comparison.....	113
7. Summary, Conclusions, Contributions and Future Work	119
7.1. Conclusions.....	121
7.2. Contribution to the State-of-the-Art	122
7.3. Recommendations for Future Work	123
References.....	124

List of Tables

Table 2.1: A319 alloy chemistry for engine block precision sand casting process	10
Table 5.1: Initial conditions applied to the casting, the chill and the sand mould.....	45
Table 5.2: Thermo-physical properties of A319 alloy, bonded silica sand, and copper	47
Table 5.3: Mechanical properties of A319 alloy, bonded silica sand, and copper	49
Table 5.4: Mesh statistics, 2-D model	51
Table 5.5: Initial conditions applied to the chills and the sand mould cap.....	66
Table 5.6: Mesh statistics.....	77

List of Figures

Figure 1.1: Fuel efficiency regulations (CAFE normalized)	1
Figure 4.1: a) GM simplified mould package for a section of a 2.0-litre turbocharged 4-cylinder engine block, b) cast engine block section, c) thermocouple locations	25
Figure 4.2: a) Highland simplified mould package drag for a section of a 2.0-litre turbocharged 4-cylinder engine block, b) cast engine block section, c) thermocouple locations	27
Figure 4.3: Geometry of the simplified engine block section fabricated at Highland Ltd. (dimensions in mm)	28
Figure 4.4: a) H13 solid chill, b) side arch, c) the assembly of the solid chill and one of the two arches in the mould package, and d) dimensioned drawing of the solid chill and the solid chill arch extension for GM solid chill casting (dimensions in mm).....	29
Figure 4.5: a) H13 water-cooled chill, b) the place of the water-cooled chill in the mould system, c) dimensioned drawing of the water-cooled chill (dimensions in mm)	30
Figure 4.6: a) Transparent view of the water-cooled chill with the locations of casting and chill interface LVDTs and the chill thermocouples, b) solid view of the water-cooled chill with the locations of casting and chill interface LVDTs and the chill thermocouples, c) solid view of the water-cooled chill cut in half on the XY plane with the locations of casting and chill interface LVDTs (the same LVDT and thermocouple locations were drilled in the solid chill).....	31
Figure 4.7: LVDT installation process, a) the chill LVDT side view, b) the chill LVDT top view, c) complete LVDT assembly	33
Figure 4.8: Full GM mould casting setup a) solid chill, b) water-cooled chill.....	35
Figure 4.9: Full Highland mould casting setup a) solid chill, b) water-cooled chill	36
Figure 4.10: Locations for metallography test samples	38
Figure 5.1: The two-dimensional model domain with the sand, solid chill and casting geometries	44
Figure 5.2: 2-D model domain with basic symmetry boundary conditions.....	46

Figure 5.3: The mesh topographies in the 2-D model domains	50
Figure 5.4: Model domain and mechanical constraints applied to Case 1 a) without the mould geometry and b) including the mould geometry	53
Figure 5.5: Variation of the casting-chill IHTC with interface gap that was implemented to the 2-D model.....	55
Figure 5.6: Comparison between the Von-Mises stress results at 200 s obtained from Case 1(a) and 1(b) (deformation magnified by 10 times, and the pressure unit is in Pa).....	56
Figure 5.7: Comparison between interface gap behaviours obtained from experiment and models in Cases 1	57
Figure 5.8: Comparison between the Von-Mises stress results obtained from Case 1(b) at different times (deformation magnified by 10 times, and the pressure unit is in Pa).....	58
Figure 5.9: Comparison between interface gap behaviours obtained from experiment, Case 1(b), and Cases 2	60
Figure 5.10: The evolution of contact pressure at the pinch point in the casting-chill interface..	61
Figure 5.11: The evolution of contact pressure at the mould cap-chill interface	62
Figure 5.12: Comparison between interface gap behaviours obtained from experiment, and the sensitivity models.....	64
Figure 5.13: The three-dimensional model domain with a) solid view of the solid chill model assembly, b) transparent view of the solid chill model assembly, and c) transparent view of the water-cooled chill model assembly.....	65
Figure 5.14: The meshed model domain with mechanical and water cooling boundary conditions: (a) solid chill and (b) water-cooled chill.....	67
Figure 5.15: Boundary conditions at the casting-mould and the chill-mould interfaces (the same for the two chill).....	68
Figure 5.16: The schematic of the casting-chill interfaces with the applied boundary conditions (the same for the two chill configurations).....	69

Figure 5.17: Variation of the casting-chill IHTC with gap size implemented to the models	70
Figure 5.18: Casting-mould heat transfer coefficient implemented to the models.....	71
Figure 5.19: Thermocouple readings obtained from the side and barrel cores in the three castings	72
Figure 5.20: The schematic of the chill-mould interfaces (the same for the two chill configurations)	72
Figure 5.21: Temperature dependent heat transfer coefficient at the chill-mould cap boundaries	73
Figure 5.22: Time dependent heat transfer coefficient at the chill arch-mould interfaces	74
Figure 6.1: Thermocouple locations in the castings	78
Figure 6.2: Thermocouple locations in the chills.....	78
Figure 6.3: Temperature variation with time for various thermocouple locations within the casting and the solid chill	79
Figure 6.4: The evolution of the casting-chill interfacial gap with time in the solid chill experiment	81
Figure 6.5: Comparison between the solid chill model temperature predictions and the TC data at different locations	82
Figure 6.6: Comparison between the solid chill-casting interface gap size measurements with LVDTs and the model predictions	83
Figure 6.7: The evolution of the displacement in the casting, the chill, and the sand mould cap with time, and the temperature contours predicted by the solid chill model (The deformation is magnified by a factor of 10, and the temperature unit is in °C).....	85
Figure 6.8: The evolution of the contact pressure at the pinch point predicted by the solid chill model (The pressure unit is in Pa.)	88
Figure 6.9: The evolution of the contact pressure at the pinch point/contact area (the value is the average of the contact pressure on the contact area) predicted by the solid chill casting model..	89

Figure 6.10: Temperature variation with time for various thermocouple locations within the casting and the water-cooled chill.....	90
Figure 6.11: The evolution of the casting-chill interfacial gap with time in the water-cooled chill experiment.....	91
Figure 6.12: Comparison between the water-cooled chill model temperature predictions and the TC data at different locations in the bulkhead area	92
Figure 6.13: Comparison between the water-cooled chill-casting interface gap size measurements with LVDTs and the model predictions.....	93
Figure 6.14: The evolution of the displacement in the casting, the chill, and the sand mould cap with time, and the temperature contours predicted by the water-cooled chill model (The deformation is magnified by a factor of 10, and the temperature unit is in °C).....	95
Figure 6.15: Comparison between the gaps predicted by the models at the horizontal casting-chill interfaces	96
Figure 6.16: The evolution of the contact pressure at the pinch point predicted by the water-cooled chill model (The pressure unit is in Pa.)	98
Figure 6.17: The evolution of the contact pressure at the pinch point/contact area (the values are the average of the contact pressure on the contact area) predicted by the water-cooled chill casting model.....	99
Figure 6.18: Temperature variation with time for various thermocouple locations within the casting and the water-cooled chill with 10 s delay in water-cooling	100
Figure 6.19: The evolution of the casting-chill interfacial gap with time in the delayed water-cooled chill experiment	101
Figure 6.20: Comparison between the delayed water-cooled chill model temperature predictions and the TC data at different locations in the bulkhead area.....	102
Figure 6.21: Comparison between the delayed water-cooled chill casting interface gap size measurements with LVDTs and the model predictions	103

Figure 6.22: The evolution of the displacement in the casting, the chill, and the sand mould cap with time, and the temperature contours predicted by the delayed water-cooled chill model (The deformation is magnified by a factor of 10, and the temperature unit is in °C.).....	105
Figure 6.23: The evolution of the contact pressure at the pinch point predicted by the delayed water-cooled chill model (The pressure unit is in Pa.)	107
Figure 6.24: The evolution of the contact pressure at the pinch point/contact area (the values are the average of the contact pressure on the contact area) predicted by the delayed water-cooled chill casting model	108
Figure 6.25: Cooling curve comparison between solid chill, delayed water-cooled, and water-cooled chill conditions	109
Figure 6.26: Cooling curve comparison between solid chill, delayed water-cooled, and water-cooled chill conditions	109
Figure 6.27: Cooling curve comparison between solid chill, delayed water-cooled, and water-cooled chill conditions	110
Figure 6.28: Cooling curve comparison between solid chill, delayed water-cooled, and water-cooled chill conditions	110
Figure 6.29: Comparison between casting-chill interface gaps obtained from the three experimental conditions	112
Figure 6.30: Comparison between casting-chill interface gaps obtained from the three experimental conditions	113
Figure 6.31: The microstructure of a) solid chill casting and b) water-cooled chill casting at 5 mm distance from the chill.....	114
Figure 6.32: The microstructure of a) solid chill casting and b) water-cooled chill casting at 10 mm distance from the chill.....	115
Figure 6.33: The microstructure of a) solid chill casting and b) water-cooled chill casting at 15 mm distance from the chill.....	116

Figure 6.34: The microstructure of a) solid chill casting and b) water-cooled chill casting at 20 mm distance from the chill..... 117

Figure 6.35: Variation of SDAS with distance from the chills..... 118

Figure 6.36: Variation of SDAS with cooling rate (data obtained from the three casting experiments)..... 119

List of Symbols

SI Symbol	Quantity	Unit
A	Air Gap Width	m
A	Area	m^2
C_P	Specific Heat Capacity	$J \cdot K^{-1} \cdot kg^{-1}$
D	Diameter	m
E	Modulus of Elasticity	Pa
F_i	Force in i direction	N
h	Heat Transfer Coefficient	$W \cdot m^{-2} \cdot K$
H_e	Vickers Hardness	HV
k	Thermal Conductivity	$W \cdot m^{-1} \cdot K^{-1}$
L	Latent Heat of Fusion	$kJ \cdot kg^{-1}$
P	Pressure	Pa
q	Heat Flux	$W \cdot m^{-2}$
\dot{Q}	Heat Generation rate per unit volume	$J \cdot m^{-3} \cdot s^{-1}$
Q	Flow Rate	$m^3 \cdot s^{-1}$
R	Thermal Resistance	$W^{-2} \cdot m^2 \cdot K$
t	Time	s
T	Temperature	$^{\circ}C$
\dot{T}	Cooling Rate	$^{\circ}C \cdot s^{-1}$
U_i	Displacement in i direction	m
V	Velocity	$m \cdot s^{-1}$

SI Symbol	Quantity	Unit
α	The Coefficient of Linear Thermal Expansion	$^{\circ}\text{C}^{-1}$
γ_i	Material Parameter	-
ε	Emission Coefficient	-
ε_i	Normal Strain in i Direction	-
ε_{ij}	Shear Strain in j direction, on a plane with normal in i direction	-
μ	Viscosity	$\text{Pa}\cdot\text{s}$
ν	Poisson's Ratio	-
ρ	Density	$\text{kg}\cdot\text{m}^{-3}$
σ	Stephen-Boltzmann Constant	$\text{W}\cdot\text{m}^{-2}\cdot\text{K}^{-4}$
σ_i	Normal Stress in i direction	Pa
σ_y	Yield Stress	Pa
τ_{ij}	Shear Stress in j direction, on a plane with normal in i direction	Pa

Glossary

CAFE	Corporate Average Fuel Economy
DAS	Dendrite Arm Spacing
HCF	High-Cycle Fatigue
HTC	Heat Transfer Coefficient
IHCP	Inverse Heat Conduction Problem
IHTC	Interfacial Heat Transfer Coefficient
INT	Interface
LCF	Low-Cycle Fatigue
LVDT	Linear Variable Displacement Transducers
SDAS	Secondary Dendrite Arm Spacing
TC	Thermocouple

Acknowledgments

During the years of my graduate studies, I have been blessed to have so many supportive people around me, to each of whom I am deeply grateful.

Firstly, I would like to express my sincere gratitude and respect to my research supervisor, Professor Steve Cockcroft, for his unbelievably kind support, patience, and the never-ending encouragements, without which the completion of this research work would not have been possible. He not only taught me how to think critically and independently as a researcher but also how to be a good teacher. I am grateful to him for giving me the chance to explore other aspects of academia, such as teaching, developing and updating courses, and lab supervising. All of the valuable opportunities he provided me with, as well as always being available and enthusiastic about holding scientific discussions, helped me to build up my self-confidence and taught me how to perform a research independently. Thank you, and I owe you a lot.

I would also like to thank Professor Daan Maijer for his valuable advice, guidance, and encouragements during the course of my graduate studies. Thank you for giving me the chance to work with you and to learn from you, and thank you for always being so supportive and helpful.

I am grateful to Professor Chadwick Sinclair for his constructive feedback and advice on my thesis in the committee meetings. A heartfelt thank you to Professor Mark Jolly, my external dissertation reviewer for his thoughtful and helpful comments on my thesis.

I am very thankful to Dr. Carl Reilly and Dr. Yair Yacobi for their continuous help with the casting experiments and sharing their valuable research experiences to assist me with my thesis work during difficult times.

I would like to acknowledge the industrial partners of this project; “Nemak Canada” for providing the A319 alloy ingots and “General Motors Co.” for providing the bonded sand moulds. I would also like to acknowledge “Highland Foundry Ltd.”, in particular, Wade Marquardt, for re-designing the mould system and providing all the bonded sand mould packages needed for completing the experimental phase of this dissertation.

I am thankful to the machine shop technicians, Ross Mcleod, David Torok, and Carl Ng who helped to construct the experimental apparatus for the casting procedures. I would like to

acknowledge “Auto21” and the “Natural Sciences and Engineering Research Council of Canada” (NSERC) for their financial support during the course of this research.

Lastly, I would like to express my deepest respect and appreciation to my parents and my sisters, for their unconditional love, strong support, and continuous encouragements without which the completion of my graduate studies would not have been possible. Special thanks to all my friends who were always there for me and helped me to stay positive during tough circumstances.

To:

My parents,

My sisters,

and

All my beloved school teachers and university professors

1. Introduction

One current trend in the automotive industry is to produce small, lightweight, high-power gasoline and diesel engines. This is being driven by consumer demand to improve fuel economy without sacrificing performance and by increasingly stringent CAFE (Corporate Average Fuel Economy) requirements in North America and in Europe [3-5] – see Figure 1.1.

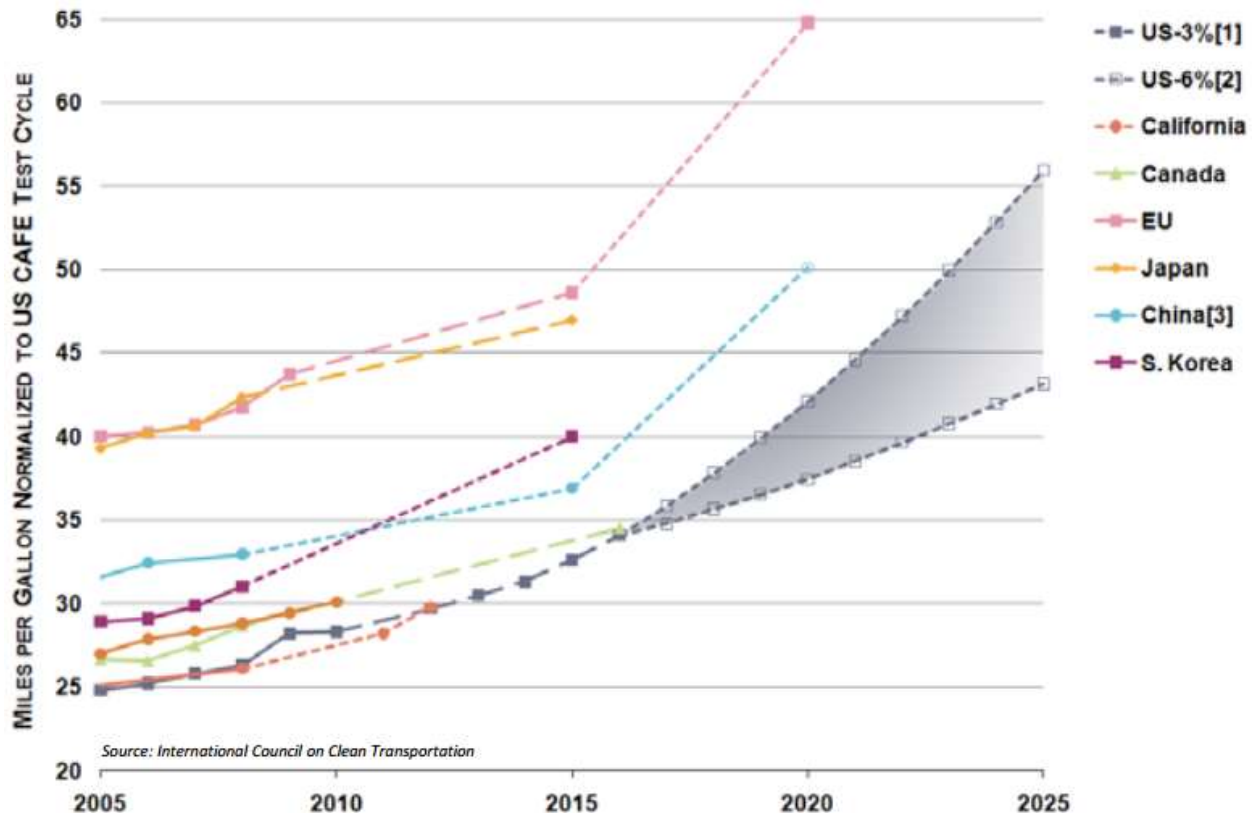


Figure 1.1: Fuel efficiency regulations (CAFE normalized) [3]

These engines are usually turbocharged in order to achieve the desired power density (i.e. higher power-to-cylinder displacement ratio). A turbocharger forces compressed air into the engine intake, allowing more air and fuel to be injected into the cylinder, which results in the production of more power in each combustion cycle. Coupled with a sophisticated engine management system, these engines can achieve good fuel economy under “normal” or “low-load” conditions and high power when needed. The advantages of using these high-power density engines include:

- Lower overall vehicle weight

- Smaller engine size
- Lower material cost
- Greater overall fuel efficiency
- Lower overall emissions
- Lower overall heat rejection

A consequence of following this trend is the need for an improvement in the thermal and mechanical fatigue properties of the engine blocks, particularly in the engine block main bearing bulkhead. One practical way to improve fatigue performance of a given alloy is to reduce the length scales of the as-cast microstructural features such as porosity and Secondary Dendrite Arm Spacing (SDAS).

The precision sand casting process is one of the manufacturing methods that is employed to manufacture engine blocks owing to its ability to produce parts with a high degree of design complexity, high durability, high level of soundness, and relatively good surface quality [4-7]. The utilization of a well-designed/placed metallic chill in the precision sand casting process offers the potential to increase the local cooling rate during solidification of the cast metal, thereby reducing the size of (refining) the microstructural discontinuities and improving fatigue properties in a given alloy system [4,8,9]. The challenges with this approach include avoiding the occurrence of cold shuts, and the formation of a columnar structure directly next to the chill, while still achieving the desired reduction in the length-scales of the microstructure.

From the standpoint of overall product quality, therefore, low initial cooling rates are desired to avoid laps and/or a columnar structure, followed by high cooling rates to reduce the microstructural length scales. One potential solution proposed to address these contrasting requirements is to adopt water-cooling in the chill. The strategy would be to postpone, or delay, the water cooling in the chill to reduce early heat extraction, and avoid cold-shuts, and then, to switch the water on at the desired time, to drastically increase the capacity of the chill to extract heat deep into the casting, thereby refining the microstructure and improving fatigue performance.

To have a closer look at this, the transport of heat from a casting to a metallic chill may be described using the following mathematical expression:

$$q = h_{Interface}(T_{Casting} - T_{Chill})$$

Equation 1.1

where q is the heat flux in ($W \cdot m^{-2}$), $h_{Interface}$ ($W \cdot m^{-2} \cdot K^{-1}$) is the interfacial heat transfer coefficient, $T_{Casting}$ is the surface temperature of the casting and T_{Chill} is the surface temperature of the chill. The employment of water-cooling maintains a large driving force for heat transport (bracketed term on the right hand side of Equation 1.1 via maintaining a low T_{Chill}). The other important term is the interfacial heat transfer coefficient, which represents the inverse of the resistance to heat transport across the interface. For example, the formation of a large gap, due to solidification shrinkage of the casting away from the chill would result in a large resistance (low $h_{Interface}$) and a reduction in heat transport. Conversely, if the casting contracts on the chill and contact pressure develops, the result would be a low resistance (high $h_{Interface}$).

Previous Work - Under the auspices of an M.A.Sc degree, work was completed to evaluate the effectiveness of a preheated water-cooled copper chill, in both moderating cooling rate in the casting directly adjacent to the chill and sustaining a large driving force for heat transfer across the casting-chill interface [10]. For this purpose, bonded sand wedge moulds instrumented with thermocouples were used. Two different chill configurations - a solid chill and a water-cooled chill - were placed into the mould. The geometries of the casting and the moulding system were based on a standard format used by NemaK Canada Ltd. to assess the microstructure and mechanical property variation with cooling rate. The thermocouples were used to acquire temperature data within the casting at varying distances from the chill and within the chill and to validate thermal-only models of the castings. In these castings, a low initial cooling rate was sought to avoid a columnar structure and cold shuts directly adjacent to the chill and a high, sustained cooling rate was sought to reduce the microstructural length scales deep into the casting, thereby highlighting a potential method of improving fatigue performance in the engine block. The results showed that this method has the potential to satisfy both proper filling and refinement of the microstructure.

Ph.D. Program - The goal of the research program described in this dissertation is to examine the potential of using water-cooled chill technology as a means of achieving refined microstructures in the main bearing bulkhead area of an A319 alloy engine block. The program of research builds on the M.A.Sc. work and uses a combination of experiments, with instrumented bonded sand moulds, and numerical modelling to understand and quantify the efficacy of a water-

cooled chill. The majority of the work conducted in the PhD program was focused on a simplified section of a 4-cylinder engine block. However, a preliminary thermal-stress analysis was undertaken at the beginning of the program using the wedge-shaped casting, utilized in the M.A.Sc. program, as a means of assessing the numerical approach to be adopted. The results of the thermal-stress analysis of the wedge-shaped casting are not included in this dissertation. A description of this work can be found in a paper published in the TMS conference proceedings, 2015 [2]. The numerical model used in the program is based on the commercial Finite Element code ABAQUS¹ and is formulated to conduct a fully coupled thermal-stress analysis. Particular focus is paid to the evolution of the interfacial resistance at the casting-chill interface and its impact on heat transfer.

¹ ABAQUS is the trademark for Dassault Systèmes.

2. Literature Review

Toward the goal of the research outlined in the introduction, the literature review will cover the following areas: 1) sand casting, 2) how to improve fatigue performance of cast components, 3) the solidification sequence and factors affecting the solidification structure of A319 alloy, 4) chill technology, 5) casting-mould interfacial heat transfer, and 6) quantification of casting-mould interfacial heat transfer coefficients.

2.1. Sand Casting

Casting processes have undergone continuous technological developments for over 7,000 years. For example, evidence of the first casting of metals, a copper frog, dates back to 5,000 BC in Mesopotamia. Since its discovery, casting has played a crucial role in the cultural and technological advancement of human society. Modern casting now embodies a broad range of technologically advanced commercial processes capable of producing high-performance parts, from a wide range of alloys with high geometric precision [11,12].

The sand casting process utilizes a mould system comprised of sand formed with a cavity in the shape of the component to be produced together with features to allow pouring and feeding of the metal into the mould cavity (defined as the gating and feeding system, respectively). A wide range of sand compositions and binders (to make the sand rigid and allow the pattern to be removed) may be used depending on the application. Some key dates with respect to sand casting include the first known use of sand moulding (645 BC, Chinese), the development of the first true foundry flask for sand casting (1709 England), the first system for making and curing sand moulds in one step (1953), the development of the lost foam process (1958) and the introduction/development of fast setting no-bake binders for sand (1960) [12-15].

Cosworth Casting Process - The “Cosworth” casting process, developed in 1987 [16], is a variant of the precision bonded sand casting process and is widely used in the commercial production of engine blocks and cylinder heads. The process consists of the following steps [7,17]:

- i. Mould fabrication (silica or zircon sand),
- ii. Mould filling,
- iii. Mould rollover

- iv. Cooling and solidification,
- v. Removal of the product from the mould

The advantages of the Cosworth precision sand casting process relative to other near-net shape casting processes in the production of engine blocks are: low production unit cost, the ability to produce geometrically complicated parts, high level of soundness, relatively accurate dimensional control, relatively good surface quality, and a high casting yield (the ratio of the weight of the final casting product to the weight of the liquid metal fed into the mould cavity)[4,17]. Proper design of a bottom-gated system reduces the metal surface turbulence while filling the mould cavity with liquid metal, hence, reduces the entrainment of oxide films. Additionally, the metal is pumped into the mould cavity is drawn from the centre of the furnace, further reducing oxide film entrainment. However, a drawback of a bottom-gated system is the unfavourable temperature gradient it develops, which is detrimental to proper feeding. The last molten metal fed into the mould is the hottest molten metal in the mould cavity and is placed at the bottom of the mould, whereas the solidifying part contains colder liquid and is placed on the top of the mould cavity. This issue is addressed in the Cosworth process by rotating the mould 180 degrees about the centre of the casting, right after the completion of the mould filling. The rollover process transforms the gating system to a feeding system and yields castings with a low solidification shrinkage-related defect content, good fatigue properties, and high durability [4,9,17].

The main limitation inherent (with respect to the microstructure of the final product) in the Cosworth casting process, as well as in the precision bonded sand casting process, is the low heat extraction rate from the casting due to the low thermal conductivity of the sand mould. This leads to slow solidification rates, which in turn result in relatively large SDAS, large dendrite cell size distributions, and large eutectic lamella spacing (including intermetallic β -Al₅FeSi platelets) in comparison to a die casting process for example. As one or more of these features may be detrimental to fatigue performance, reducing their size can result in a general improvement in the fatigue life of the component [17].

The main bearing bulkhead in an engine block, in particular, is required to have high fatigue strength due to the fact that it is subjected to high cyclic mechanical and thermal stresses during

in-service operations. Since the bulkhead is typically the thickest part in cross-sectional size within an engine block, it usually undergoes relatively slow solidification rates [6,18-21]. Utilizing the moulding system with a well-designed metallic chill (usually made of cast iron, steel, or copper) directly in contact with the bulkhead, or the main bearing saddle region, is one approach to increase the heat transfer rate and generate a finer cast microstructure, which leads to higher tensile and fatigue properties [4,6,9,22,23].

2.2. How to Improve Fatigue Performance of Cast Components

Fatigue can be defined as:

“The process of progressive localized permanent structural change occurring in a material subjected to conditions that produce fluctuating stresses and strains at some point or points and that may culminate in cracks or complete fracture after a sufficient number of fluctuations”[24].

Fatigue failure can have very severe consequences and is often catastrophic, as it can occur precipitously and without warning. Fatigue accounts for at least 90% of all in-service failures attributed to mechanical causes and is known as the most common mechanism under which engineering components fail [23-27].

The process of fatigue failure includes four stages:

- i. Nucleation or micro-crack initiation
- ii. Structurally dependent crack propagation (often called the "short crack" or "small crack" phase)
- iii. Macro-crack propagation or stable crack growth that can be characterized by linear elastic fracture mechanics, elastic-plastic fracture mechanics, or fully plastic fracture mechanics
- iv. Unstable or fast crack growth resulting in a catastrophic failure.

In terms of the overall fatigue life, the crack propagation stage dominates the low-cycle fatigue (LCF) life, and crack initiation stage controls the high-cycle fatigue (HCF) life [24].

The widespread application of cast Al-Si alloys in structural components persuaded researchers to study the fatigue and fracture behaviour of these alloys extensively. Several studies

[23,28-31] have reported that fatigue resistance of an alloy depends greatly on the microstructural discontinuities and the degree of the soundness of the product. Other factors include the mechanical properties of the alloy, surface flaws associated with the manufacturing process, and the residual stresses associated with the manufacturing process.

Microstructural Discontinuities – Microstructural discontinuities in cast metals include dendrites, grains (both columnar and equiaxed), eutectic and intermetallic phases, porosity (macro and micro), and entrained oxides (both films and particles). Small primary and secondary dendrite arm spacing (DAS and SDAS), fine grain size, fine eutectic phase morphology, all contribute to improved fatigue resistance [9,25,31-34]. In the case of porosity, for example, the crack initiation stage maybe reduced by the high-stress concentration region that develops adjacent to both the large individual pores and clusters of small pores. A number of studies [15,33,35-38] have proven that at a given stress, the fatigue life is controlled by pore size or a cluster of closely spaced pores; and that a fatigue crack can initiate after a relatively small number of cycles [29,31,39]. In several studies [18,31,40] porosity has been recognized as the major cause for rejection of the cast Al-Si components in structural applications which involve cyclic loading.

Virtually, all the microstructural discontinuities scale with the grain size, such that a casting with fine-grain structure, will exhibit improved in-service fatigue properties in comparison to another identical casting with a course structure. In addition to reducing the length scale, or size of the microstructural discontinuities, it is desirable to also avoid a columnar or oriented structure [38].

Mechanical/Material Properties – As indicated in several studies [23,32,41], a high yield stress and ultimate tensile strength, and narrow stress/strain hysteresis loop, also improve the fatigue resistance of the alloy. Whereas, in applications involving thermal cycling leading to thermal stresses, both a high thermal conductivity and low thermal expansion coefficient can enhance higher fatigue durability [25].

Surface Defects and Residual Stresses – As reported in the literature [24,42,43], most fatigue cracks nucleate at or close to the surface of a material. This is because the slip steps start to form at the surface of the part resulting in the accumulation of damage at the surface. In the presence of surface damages arising from the manufacturing process or from in-service wear-and-

tear, the crack initiation stage is significantly reduced due to stress concentration at the roots of the surface damages. In some conditions, where the size of a surface discontinuity is well below the critical value, repairing (e.g. polishing) the part will help to extend the fatigue life of the component. On the other hand, if the surface damage size is more than or equal to the critical value, it results in the rejection of the part.

There are a number of sources of surface defects in casting processes. Cold shuts, for example, often act as crack nuclei for fatigue fractures. When large, they can reduce the strength of a part to the extent that it can fracture under a single application of load [44]. This discontinuity, which may appear as a crack, or a seam with smooth, rounded edge, forms when solidification progresses too fast, or under conditions where there is excessive loss of superheat during mould filling process. This results in low liquid metal fluidity, which in turn can cause periodic blockages in the smooth flow of molten metal over the mould surface, and can also form a seam or entrained oxide film in the casting where two free surfaces meet during mould filling [13,44,45]. Unfortunately, the process conditions which increase the cooling rate and result in the development of a fine microstructure – such as using highly conductive mould materials, and low pour superheat – can lead to the formation of cold shuts.

Another source of surface defect is porosity that intersects the surface of the casting. This can be a gas porosity associated with outgassing of the mould, hydrogen porosity, or shrinkage-based porosity. In all cases, these pores may act as pre-existing cracks that greatly reduce the crack nucleation/initiation phase of fatigue cracking.

Residual stresses are also important in determining the fatigue life of the cast components. One well-known approach for extending the fatigue life of a component is to shot peen the part in order to create a compressive residual stress at the surface. This reduces the susceptibility of the component to surface flaws that otherwise would be fatigue life limiting [24,43,46].

As solidification length scales and porosity both strongly affect fatigue life and scale with cooling rate, a closer look at how the two are influenced by heat transport, is necessary.

2.3. The Solidification Sequence and Factors Affecting the Solidification Structure of A319 Alloy

A319 alloy is a hypo-eutectic, heat treatable Al-Si-Cu alloy [47,48]. The composition of A319 is given below in Table 2.1.

Table 2.1: A319 alloy chemistry for engine block precision sand casting process¹

Alloying Element	Si	Fe	Cu	Mn	Mg	Zn	Ti	Sr
Balance (Wt%)	8.10 -8.6	0.27 -0.59	2.60 -2.95	0.19 -0.44	0.31 -0.4	0.4 - 0.8	0.11 - 0.16	0.004 max

Solidification Sequence – The development of the cast structure of A319 alloy follows the following sequence under typical industrial sand casting cooling conditions [15,47-51]:

- i. Solidification begins with the nucleation of primary α -aluminium dendrites at approximately 610 °C;
- ii. At about 565 °C, corresponding to a fraction solid of approximately 0.55, the main aluminium-silicon eutectic forms.
- iii. At approximately 540 °C, corresponding to a fraction solid of 0.89, the precipitation of Mg_2Si and $Al_8Mg_3FeSi_6$ occurs.
- iv. At around 525 °C, corresponding to a fraction solid of 0.93, the formation of interdendritic, blocky $CuAl_2$ with needle shape $\beta-Al_5FeSi$ platelets occurs;
- v. At approximately 507 °C, corresponding to a fraction solid of 0.99, the formation of eutectic $CuAl_2$, accompanied by scattered $\alpha-Al$ and $Al_5Mg_8Cu_2Si_6$ (if the chemical composition contains Mg) occurs and;
- vi. At approximately 504 °C solidification is complete.

Solidification Morphology and Length Scales – The availability of nucleation sites and the cooling rate determine the grain morphology and size. One effective treatment to reduce the grain size and ensure an equiaxed structure is to increase the number of heterogeneous nucleation sites by adding a grain refiner to the melt. Common grain refiners used in the aluminium industry are Al-Ti and Al-Ti-B master alloys [26,41,52-54]. For a given alloy chemistry, including those that

¹ Chemical composition was provided by Nematik of Canada Ltd.

have been grain refined, increasing the cooling rate results in larger undercoolings, which in turn activates a greater number of heterogeneous nucleation sites within a given population.

As to the primary Dendrite Arm Spacing (DAS) and Secondary Dendrite Arm Spacing (SDAS), which are often used to quantify the “microstructural fineness”, they are both reduced with increasing the cooling rate as the growth morphology adapts to create more surface area for mass and heat transport [52,55]. The treatments, which lead to fine dendrite size, also will modify the eutectic silicon morphology – e.g. reduce the lamella spacing, colony size and aspect ratio [51,52,55].

The following empirical mathematical relationship between solidification rate and SDAS has been developed and suggested in the literature:

$$SDAS = at_f^n = b(\dot{T})^{-n} \quad \text{Equation 2.1}$$

where the exponent “ n ” is in the range of 0.3 to 0.5 for the SDAS and generally very close to 0.5 for the DAS. In Equation 2.1, t_f is the solidification time, a and b are fitting parameters, and \dot{T} is the cooling rate evaluated over the solidification interval ($^{\circ}\text{C/s}$) [55].

Cast Porosity – Aluminium alloys are susceptible to pore development because of the large volumetric shrinkage associated with solidification, which has been reported to be up to 7%, and because of the large difference between the hydrogen solubility in the liquid and in the solid. Consequently, there are two types of porosity that can form in aluminium casting parts: 1) Macro-Porosity and 2) Micro-Porosity [15,39,56-58].

Macro-Porosity results from solidification shrinkage and is associated with liquid encapsulation. Usually, macro-shrinkage porosity is limited to the last section to solidify in the casting, but can spread out to the casting surface and is normally greater than 1 mm in equivalent radius [37,57,58]. In the absence of directional solidification, a substantial amount of liquid can become surrounded by solid material. Mechanically, the surrounding solid serves as a ‘pressure vessel’ and the volumetric shrinkage associated with solidification decreases the pressure within the encapsulated region to well below the levels experienced inter-dendritically associated with late stage feeding. If the pressure drops below the hydrogen gas pressure in equilibrium with hydrogen in solution and/or the vapour pressure of aluminium, the result is the formation of an

expanded hydrogen bubble and/or aluminium vapour bubble, which then becomes a large void or a cluster of large voids. A basic solution to avoid macro-shrinkage formation is a good design of the mould system to improve feeding and avoid liquid encapsulation. This may be achieved by controlling heat transport, which includes strategic placement of in-gates, riser(s), chill(s), and/or insulating materials [9,31,40,59]. The origin of porosity in precision sand cast engine blocks made of A319 alloy is reported to be from very slow solidification rates. The lowest amount of porosity that was achieved in the above-mentioned castings to date, was due to employing a non-turbulent filling process followed by rapid solidification imposed by a chill. Rapid solidification conversely promotes shorter liquid feeding ranges [9,17,31,48,56,60].

Micro-Porosity, in contrast, is a series of discrete, isolated cavities which are less than 1 mm in equivalent radius [15,39,58]. The micro-scale porosity in aluminium alloy castings is generally more complicated to eliminate since it occurs due to the isolation of small inter-dendritic pockets of liquid within the mushy zone at high solid fractions [39,61]. The pressure drop in these regions is generally low, and pores form due to a change in hydrogen solubility associated with the liquid-to-solid transformation in aluminium castings.

At atmospheric pressure, the hydrogen solubility in aluminium is approximately $0.7(\text{mL})/100(\text{cm}^3)$ at the liquidus and $0.05(\text{mL})/100(\text{cm}^3)$ at the solidus [58]. During solidification, the solidifying metal rejects hydrogen into the liquid and causes the hydrogen concentration in the liquid to rise. As solidification proceeds, if the hydrogen activity in the liquid exceeds the solubility limit together with an overpressure associated with nucleation, a pore will nucleate and grow in the interdendritic liquid [26,35,39,58].

Normally, mass feeding through interconnected liquid channels takes place during solidification until channel connectivity is lost, which normally occurs at mass fractions in the range of 0.9 to 0.95 and above. At this stage, small inter-dendritic pockets of liquid become isolated. As the isolated pockets of inter-dendritic liquid solidify, the pressure within them will drop below the solubility limit of hydrogen, resulting in small distributed microporosity formation [15,20,39,58,59].

2.4. Chill Technology

As discussed in the previous section, fatigue properties of a cast part are strongly influenced by its microstructure and the degree of soundness of the part. The microstructure itself is determined by the type of the alloy being cast and the casting process. Focusing on the casting process, the application of local cooling can improve heat extraction and reduce the length scales of the microstructural features that affect fatigue properties, thereby, improve the fatigue performance of the cast product. The use of metallic chills in the precision sand-cast engine blocks and cylinder heads has been playing an important role in improving the mechanical properties of these cast products. The complicated geometries of engine blocks and cylinder heads include thick and thin sections, at different distances from the gating system. Generally, the thick sections will undergo slower cooling rates during solidification, have coarser microstructures, and will exhibit relatively poorer fatigue properties than the thinner, more rapidly solidified sections. If these sections also correspond with highly stressed areas such as the engine block main bearing bulkheads, they can limit the fatigue life of the component. The application of a metallic chill, which is directly in contact with the solidifying metal, can locally increase the heat flow from the thick sections and result in a finer microstructure and better fatigue performance [4,6,9,13,15,21,22,38,49,50,62].

In 2001, Heusler *et. al.* [9] suggested that both the microstructure and the alloy type should be improved in order to produce engine blocks with superior mechanical properties. For this purpose, they presented a newly developed alloy of the type AlSi₇MgCuNiFe for the production of engine blocks. In their research, three block types were cast. For the production of the first sample, the filling and feeding process took place via the crankshaft bearings and the oil flange. Also, for local cooling, a steel chill was placed at the joint face. For the second block, the casting was filled and fed via the joint face, and the chill was placed on the surface of the crankshaft bearing bulkheads. The third block was filled and fed in the same way as the second block, but no metallic chills were used in the process. The resultant microstructure of the second sand casting within the crankshaft bearing area was significantly improved due to the use of steel chill. After making comparisons between the mechanical test results of the three castings, they recommended the second casting method for the production of diesel engines that undergo large in-service stresses in the main bearing bulkheads.

In 2009, MacKay *et. al.* [4,6,17,20] proposed using cast iron and copper chills in the Cosworth process for the production of engine blocks. This method allows for a combination of controlled filling and improved mechanical properties of the cast component by reducing the length scales of the microstructural features in the microstructure of the engine block in proximity to the chills.

Several researchers [22,38,50,59,63-65] have used copper, cast iron, and steel chills in the production of cast parts made of Al-Si alloys and reported the effect of using a chill on the size, morphology, and distribution of the microstructural features (such as SDAS, porosity, intermetallics, eutectic phase, etc.), hence, on fatigue properties:

“The microstructure of the solidified casting becomes progressively coarser with increased distance from the chill.” [38].

The results of all the above-mentioned studies confirm that making use of the chill technology improves the heat transport from the casting, which results in a reduction in the length scales of the microstructural discontinuities. The chill size (thermal mass) and geometry have been mentioned as two important factors which determine the capacity to enhance heat transport. Some studies [66-68] have also investigated the role of the air gap that develops between the casting and the chill, in reducing the capacity of the chills to remove heat from the castings.

2.5. Casting-Mould Interfacial Heat Transfer

Based on a review of previous studies [51,69-71], either an interfacial heat flux (q) or an interfacial heat transfer coefficient (h) can be used to characterize the heat transfer that occurs across the casting-mould and/or casting-chill interfaces.

The interface between the casting surface and the mould surface represents a resistance to heat flow due to the presence of asperities on the casting and the chill surfaces, which cause loss of contact. Therefore, heat transport across this interface is generally better described using a heat transfer coefficient via Equation 2.2:

$$q = h_{Interface}(T_{Casting} - T_{Chill}) \quad \text{Equation 2.2}$$

where, as previously described, q ($W \cdot m^{-2}$) is the heat flux, $h_{Interface}$ ($W \cdot m^{-2} \cdot K^{-1}$) is the interfacial heat transfer coefficient between the casting and the mould, $T_{Casting}$ (K) is the temperature at the point on the casting side of the interface, and T_{Chill} (K) is the temperature on the chill side of the interface [72].

There are a number of factors that can influence h . These include: the thermal histories of the metal and the mould including superheat and preheat, the thermal expansion/contraction characteristics of the casting material and the mould material, the mould surface roughness, the geometry of the metal and the mould, and the relative displacements of the two arising during cooling/heating [51,73-79]. These factors generally contribute to a variation in the degree to which the surfaces are in contact –i.e. the presence of a gap(s) or the presence of pressure (closing the interface) [79-81].

In general, the heat transfer coefficient is the highest at the time the molten metal is introduced to the mould, due to the good contact between the mould and the molten metal. As the cooling of the metal proceeds, a large number of nuclei will form at the interface with the mould and grow due to the large undercooling at the interface [81,82]. A gradual decrease in the heat flow between the casting and the mould will then take place with the evolution of solidification. This resistance to heat flow occurs due to the formation of small periodic gaps on the surface of the cast part, resulting from solidification at the mould surfaces. As cooling continues and mass feeding ends, the casting part goes through a thermal contraction. Propagation of the solidification front into the bulk of the casting will result in the accumulation of appreciable contraction in the casting. The result of this can be the “pulling away” of the casting from the mould or the thermal contraction of the casting on the mould. The former resulting in the creation of a continuous physical gap, and a substantial decrease in h , and the latter resulting in the development of closing pressure, and a potential for little change in h relative to when liquid is present. In the case where the mould package is equipped with a chill, the interaction of the chill with the casting and the mould package can further complicate the behaviour of the interface.

The resistance to heat transport is believed to be proportional to the size of the gap. During the formation of the gap, the heat transfer process will be a combination of a conductive heat transport within the fluid in the gap, and a heat transport via radiation. The dominant heat transfer mechanism across the “air-gas” mixture depends on temperature. The involvement of radiation

heat transfer to the total heat transfer is reported to be negligible in the case of the alloys that have low melting points, such as aluminium alloys [51,73-76,81,83-85].

2.6. Quantification of Casting-Mould Interfacial Heat Transfer Coefficient

The estimation of the metal-mould (or chill) interfacial heat transfer coefficient is complicated as it needs to consider the thermal history and the geometry of the interface, likewise the thermo-physical properties of the casting, the mould, and the chill [79,80,86,87].

There is evidence in the literature that shows researchers have been successful in measuring/estimating the interfacial heat transfer coefficient using the following methods:

- 1) By measuring the gap size formed between the casting and the mould during the casting process, and correlating the gap size to interfacial heat transfer coefficient,
- 2) By using the thermal data obtained from various thermocouple locations at the interface in the casting and in the chill, to solve the Inverse Heat Conduction Problem (IHCP) and calculate the interfacial heat transfer coefficient, and
- 3) By using the thermal histories at specific thermocouple locations in the casting and in the chill, and developing a mathematical model of heat conduction to derive the interfacial heat transfer coefficient based on trial-and-error method [74,79,81,84,88,89].

Several researchers [74-76,78,81,88-90] made attempts to measure the interface gap size and reported that both the casting and the chill move during the casting process. The resistance to heat flow at the casting-chill interface is usually defined as a time dependent function since both the deformation of the solidifying metal and the oxide growth on the casting surface are dependent on time [78].

Ho *et. al.* [80,83] used two methods for the estimation of the interfacial heat transfer coefficient. In the first method, the thermocouple measurements at both the casting and the chill were used in a numerical solution of the inverse heat conduction problem. In the second method, two Linear Variable Displacement Transducers (LVDT) were installed in the casting and the chill, in order to keep a continuous record of the movements of the casting and the chill surfaces. The interfacial gap size was then calculated using the difference in the movement of the two faces and the transient heat transfer coefficient was derived from thermal conduction and radiation equations.

Nishida *et. al.* [85] also used the same two methods to calculate the interfacial heat transfer coefficient. In their experiments, some displacement meters were used in order to measure the displacements of the casting surface and the mould surface. Kulkarni *et. al.* [75] made use of the same two methods, too. For the gap measurement experiment, two sensitive displacement gauges were installed in the casting and the chill surfaces, to record the movement of both the surfaces. The gap size was defined by taking the difference of the two movement measurements.

Majumdar *et. al.* [91] proposed to determine the gap formation time and record the variation of the gap size during solidification time with measurement of electrical capacitance across the gap. The set-up consisted of a copper electrode which was installed as a sensing element, a capacitance meter for measuring the gap, and a voltage recorder to keep track of variation of capacitance.

Kim *et. al.* [79] designed a mould for a tube-shaped casting to investigate the behaviour of the interfacial thermal resistance for different aluminium alloys. A sequential function specification procedure was used in order to estimate the interfacial heat transfer coefficient at both inside and outside of the tube. The function specification method is a way to solve the inverse heat conduction problem, which assumes the heat transfer coefficient to be a function of time. Stolz [92] made use of numerical methods to inversely solve the heat conduction problem for simple casting geometries. Abdel Wahed *et. al.* [93] conducted a similar experiment and used an explicit finite difference method to solve a two-dimensional heat flow equation.

In 1991, El-Mahallawy *et. al.* [71] developed a computer program, based on an explicit finite difference model, to solve a one-dimensional heat conduction equation for a cylindrical shaped casting, and evaluate the interfacial heat transfer coefficient as a function of time. They found the Interfacial Heat Transfer Coefficient (IHTC) to be strongly influenced by the air-gas temperature and the metal superheat.

Heichal, Loulou, and Wang [76,77,81] suggested that releasing a droplet of molten metal on a solid surface, can be an appropriate method for the estimation of thermal contact resistance. For this purpose, the temperature of the droplet is measured, and then the results from numerical or analytical heat transfer model will be validated with the thermocouple readings.

Kumar *et. al.* [70] proposed a model to evaluate the transient heat flux across the casting-chill interface as a function of thermo-physical properties of the chill material and its thickness for two aluminium alloys. The model uses the thermal histories at different locations in the chill to inversely solve the one-dimensional Fourier heat conduction equation, and predict the interfacial heat transfer coefficient. In a similar experimental design, Gafur *et. al.* [69], evaluated the casting-chill interfacial heat transfer coefficient during solidification of square bars made of commercially pure aluminium with different superheats. The non-linear, one-dimensional Fourier heat conduction equation was inversely solved to estimate the interfacial heat transfer coefficient.

Griffiths [73,74] developed a model to predict the interfacial heat transfer coefficient for a water-cooled copper chill casting for the case of unidirectional solidification of an Al-Si alloy. The solidification directions examined were vertically upward, vertically downward, and horizontal. An explicit finite difference method in combination with the inverse heat conduction solution was used to derive the heat transfer coefficient. It was concluded that the vertically upward casting procedure was associated with the highest heat transfer coefficients.

Kang *et. al.* [94] derived the IHTC between a heating plate and a roller in a steel direct rolling process, by the use of a trial-and-error method. The FE (Finite Element) method was used to solve a two-dimensional transient heat conduction problem. Pokorny *et. al.* [95] also used a trial-and-error method to calculate the casting-mould interfacial heat transfer coefficient in an AZ91D magnesium alloy casting. The estimated IHTC was then used to develop a visco-plastic deformation model, which was applied to predict hot tear evolution in the alloy.

Fardi *et. al.* [96] investigated the effect of external loads on the interfacial heat transfer coefficient at the interface between an A356 alloy and a carbon steel mould. The results of their experiments show that applying an external pressure, leads to a better contact between the casting and the mould at the interface, hence, increases the interfacial heat transfer coefficient. They also derived a mathematical correlation between the interfacial heat transfer coefficient and the applied pressure:

$$h = 0.0011P^3 - 0.112P^2 + 6.605P + 2924.57 \quad \text{Equation 2.3}$$

where h ($W \cdot m^{-2} \cdot K^{-1}$) is the interfacial heat transfer coefficient, and P (MPa) is the applied pressure.

Fackeldey *et. al.* [97] reported that the IHTC can be expressed in two ways:

1) As a function of the air gap size:

$$h_{eff} = h_{radiation} + h_{cond,air} = \sigma(T_{Casting}^2 - T_{Mould}^2)(T_{Casting} - T_{Mould}) \frac{1}{\frac{1}{\epsilon_{Casting}} + \frac{1}{\epsilon_{Mould}} - 1} + \frac{k_{air}}{\delta_{airgap}} \quad \text{Equation 2.4}$$

where k_{air} ($W \cdot m^{-1} \cdot K^{-1}$) is the heat conduction of the air, ϵ is the emission coefficient, and σ is the Stephen-Boltzmann constant, 5.67×10^{-8} ($W \cdot m^{-2} \cdot K^{-4}$).

2) As a function of contact pressure between the casting and the mould:

$$h_{eff} = h_{cond,contact} = \gamma_1 \left[\frac{P_{int}}{H_e} \right]^{\gamma_2} \quad \text{Equation 2.5}$$

with γ_1 , γ_2 as material parameters, H_e as Vickers Hardness, and P_{int} (Pa) as contact pressure at the interface.

Trovant *et. al.* [86,87] conducted research to develop a model which predicts the evolution of the air gap and the IHTC during solidification of several metals and alloys (pure aluminium, A356 alloy, A206 alloy, Al-4% Cu alloy, and pure tin) in moulds made from different materials (a graphite mould, a sand mould, and a copper mould). In the first stage, they calculated the heat transfer coefficient by solving the energy balance equation for small Δr (the gap size), using the thermal data from their experiments:

$$q_{conv,int} = q_{cond,int} \quad \text{Equation 2.6}$$

$$h_{int}(T_{Casting,int} - T_{Mould,int}) = k_{Mould} \left(\frac{T_{Mould,int} - T_{Mould,int-\Delta r}}{\Delta r} \right) \quad \text{Equation 2.7}$$

$$h_{int} = \frac{k_{Mould}}{\Delta r} \left(\frac{T_{Mould,int} - T_{Mould,int-\Delta r}}{T_{Casting,int} - T_{Mould,int}} \right) \quad \text{Equation 2.8}$$

where k_{mould} ($W \cdot m^{-1} \cdot K^{-1}$) is the conductivity of the mould and r (m) is the gap size.

The results from this calculation were compared to the results from the analytical relationship to define h , assuming a perfectly flat interface:

Immediately after liquid metal is poured into the mould:

$$h = \frac{1}{R} \quad \text{Equation 2.9}$$

When the gap initiates and grows:

$$h = h_{cond,gas} + h_{radiation} = \frac{k_{air}}{A} + \frac{\sigma(T_{Casting,int}^2 + T_{Mould,int}^2)(T_{Casting,int} + T_{Mould,int})}{\frac{1}{\epsilon_{Casting}} + \frac{1}{\epsilon_{Mould}} - 1} \quad \text{Equation 2.10}$$

where R ($W^{-2} \cdot m^2 \cdot K$) is the thermal resistance, A (m) is the air gap width, σ is the Stefan-Boltzmann constant, and ϵ is the emissivity.

This approach was successful in characterizing the factors that influence the heat transfer coefficient, and in the establishment of a general mathematical relationship for HTC:

$$HTC = f(\text{air gap size, roughness of mould surface, conductivity of gas in the gap, thermo-physical properties of the metal and the mould})$$

In the last step, they proposed a semi-empirical equation to calculate the HTC at the casting-mould interface:

$$HTC = \frac{1}{k \cdot A + r} + C \quad \text{Equation 2.11}$$

where k ($W^{-1} \cdot m^2 \cdot K \cdot mm^{-1}$) is the conductivity related parameter, A (mm) is the air gap size, r ($W^{-1} \cdot m^2 \cdot K$) and C is a variable with units of ($W \cdot m^{-2} \cdot K^{-1}$). This equation is a function of air gap size, which is reported to be the most dominant variable affecting the IHTC. Other variables in this equation – i.e. k , r , and C – allow the user to implement the effect of mould surface roughness, radiation, coating, etc. on the IHTC. The air gap size in their experiments was measured with the use of two LVDTs.

Based on the review of the literature, it is clear that the thermal mass of the chill and the Interfacial Heat Transfer Coefficient (IHTC) play an important role in the ability of the chill to influence cooling rate in the casting.

3. Scope and Objective

The objective of this research is to explore using water-cooled chill technology as a means of refining the SDAS in the main bearing bulkhead in small, four-cylinder, turbocharged engine blocks made from A319 alloy. Thereby, potentially improving the fatigue life of the newer generation of lightweight engine blocks. Toward this goal, 12 casting experiments were conducted on two mould packages, based on a section of a 4-cylinder engine block. These mould packages were provided by “General Motors Co.” and “Highland Foundry Ltd.” (*GM was unable to provide all the necessary mould packages required for the program due to problems encountered at their research foundry, located in Warren, Michigan. Thus, two different mould packages were used*). Two different chill configurations were used in the above-mentioned castings: 1) a solid chill that is currently being used in industry; and 2) a water-cooled chill, which was designed at UBC as a part of this thesis work. In all of the experiments, the mould packages were instrumented with thermocouples to record thermal data in the casting, the chill and the mould. Linear Variable Displacement Transducers (LVDT) were also placed in the casting and the chill to measure the evolution in the gap development at the casting-chill interface. The initial work was conducted using the moulds provided by GM. This work was undertaken to develop and refine the methodology for conducting interface displacement measurements using the LVDTs – one fixed to the casting at the casting-chill interface and one fixed to the chill at the chill-casting interface. All of the remaining instrumented castings were conducted using the mould package provided by Highland Foundry. Additionally, metallography samples were taken from different parts of the bulkhead area in the casting in order to evaluate the SDAS size (degree of microstructural refinement). Details on the experimental procedure are presented in Chapter 4 of this thesis.

The results from the experimental program were complemented by completing a detailed thermal-stress analysis of the castings. The objective of the numerical-based analysis was to quantify the behaviour of the interface in terms of the relationship between heat transfer and gap development. The approach hinges on the development of a fully coupled thermal-stress model of the engine block section and the chill and is validated using the empirical thermocouple and LVDT data derived from the casting experiments. The numerical model has been developed using the general commercial finite element package “ABAQUS” version 2016, which is reported to have advanced capabilities for solving problems involving contact interface. Details related to the

mathematical model development and application to the engine block sand casting are presented in Chapter 5.

4. Experimental Methodology

The sand moulds that were used in the experiments for this research were simplified $\frac{1}{4}$ sections of a 2.0-litre turbocharged 4-cylinder engine block mould package made from bonded silica sand, designed and fabricated at “General Motors Co.” and “Highland Foundry Ltd.”. The two mould packages that were provided by GM were used for two initial test castings, one with the solid chill and one with the water-cooled chill. However, due to a hazardous material issue detected at GM’s research foundry, the foundry was shut down and the company was not able to provide the additional mould packages needed to complete the proposed program. Highland Foundry Ltd., located in Surrey, BC, kindly supported this research work with providing an additional 10 mould packages.

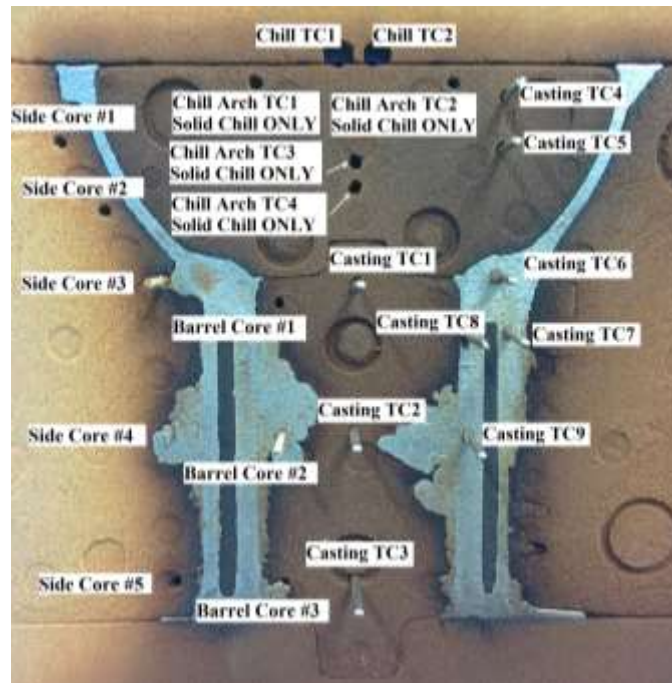
4.1. GM Mould Package Thermocouple Setup

Figure 4.1 (a) shows a side view of the assembled GM mould package (note: the oil drain back core and the cast iron liner were not included in the mould packages to simplify the casting, as it was reasoned that these would not alter significantly the heat transfer in proximity to the chill). The image shows the mould with the refractory board removed from the face that is oriented toward the camera (the white refractory board can be seen fixed to the back of the other side). The solid version of the H13 chill can be seen sitting on the top of the mould cavity, directly above the main bearing bulkhead. Figure 4.1 (b) shows the final cast part including the gating system and the feeding system after extraction of the sand mould. Figure 4.1 (c) shows the post-cast location of the thermocouples that were used in the experiments with the GM mould packages. Two thermocouples were inserted in the bulkhead area, 10 and 30 mm away from the chill, underneath the flat section of the chill. In addition, three thermocouples were inserted in the barrel area at 10, 60, and 110 mm from the bulkhead at the centre of the mould cavity, and four thermocouples were inserted in the cylinder water jacket area (Casting TC6 - TC9). Finally, three thermocouples were placed in the chill. Two thermocouples were inserted in the arch to the middle of the chill and one thermocouple was inserted in the chill arch vertically (2 mm above the chill-casting interface). For the solid chill, 4 thermocouples were inserted in the arch extension as can be seen in Figure 4.1 (c).



(a)

(b)



(c)

Figure 4.1: a) GM simplified mould package for a section of a 2.0-litre turbocharged 4-cylinder engine block, b) cast engine block section, c) thermocouple locations

All the thermocouples that were used to measure the temperature in the castings were Type-K, 0.5 mm diameter wire, sheathed in a nickel-chrome based alloy (Super OMEGACLAD XL, measurement accuracy: $\pm 0.4\%$). The thermocouple wires in all the experiments (including the experiments with Highland mould packages) were exposed at the tip and twisted and spot-welded

to form the thermocouple junction. All the thermocouples that were used to measure the temperature in the chill and the two interface thermocouples were Type-K, 0.2 mm diameter wire, sheathed in alumina tubes (measurement accuracy: $\pm 0.4\%$). The sources of error with respect to temperature readings are the $\pm 0.4\%$ intrinsic thermocouple error reported by the company, and any loss of contact that might have happened between the thermocouple tip and the casting or the chill during the experiment.

4.2. Highland Mould Package Thermocouple Setup

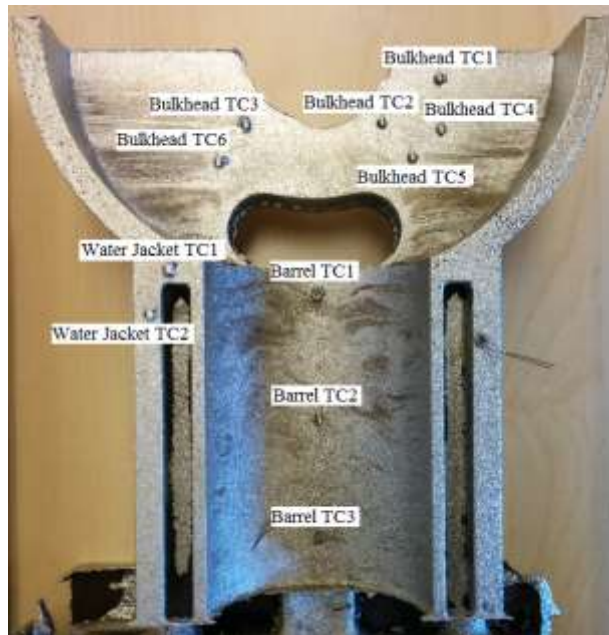
Figure 4.2 (a) shows a side view of the Highland mould package including all the cores and the thermocouple locations. The Highland mould packages were configured differently from the GM packages in that they did not use insulating fibre plates on either side of the bonded sand mould packages to provide metal containment, rather they used two bonded sand sections that were clamped together to form the mould. The chill was placed in the same location as it was placed in the GM mould packages – i.e. at the top of the mould package and in contact with the bulkhead. Figure 4.2 (b) shows the final cast part including the gating and the feeding systems. Figure 4.2 (c) shows the locations of the thermocouples in the casting.

Based on the results from the first set of experiments, it was decided to add a total of 4 additional thermocouples to the bulkhead section and remove TC8 and TC9 from the water-jacket area, since the main focus of the experiments was making an improvement in the cooling rate at the bulkhead area. The numbers and positions of the in-chill and in-mould thermocouples for experiments with Highland mould packages were the same as the GM mould packages.



(a)

(b)



(c)

Figure 4.2: a) Highland simplified mould package drag for a section of a 2.0-litre turbocharged 4-cylinder engine block, b) cast engine block section, c) thermocouple locations

Figure 4.3 shows the geometry and dimensions of the Highland simplified engine block section. The dimensions were the same as the GM engine block section.

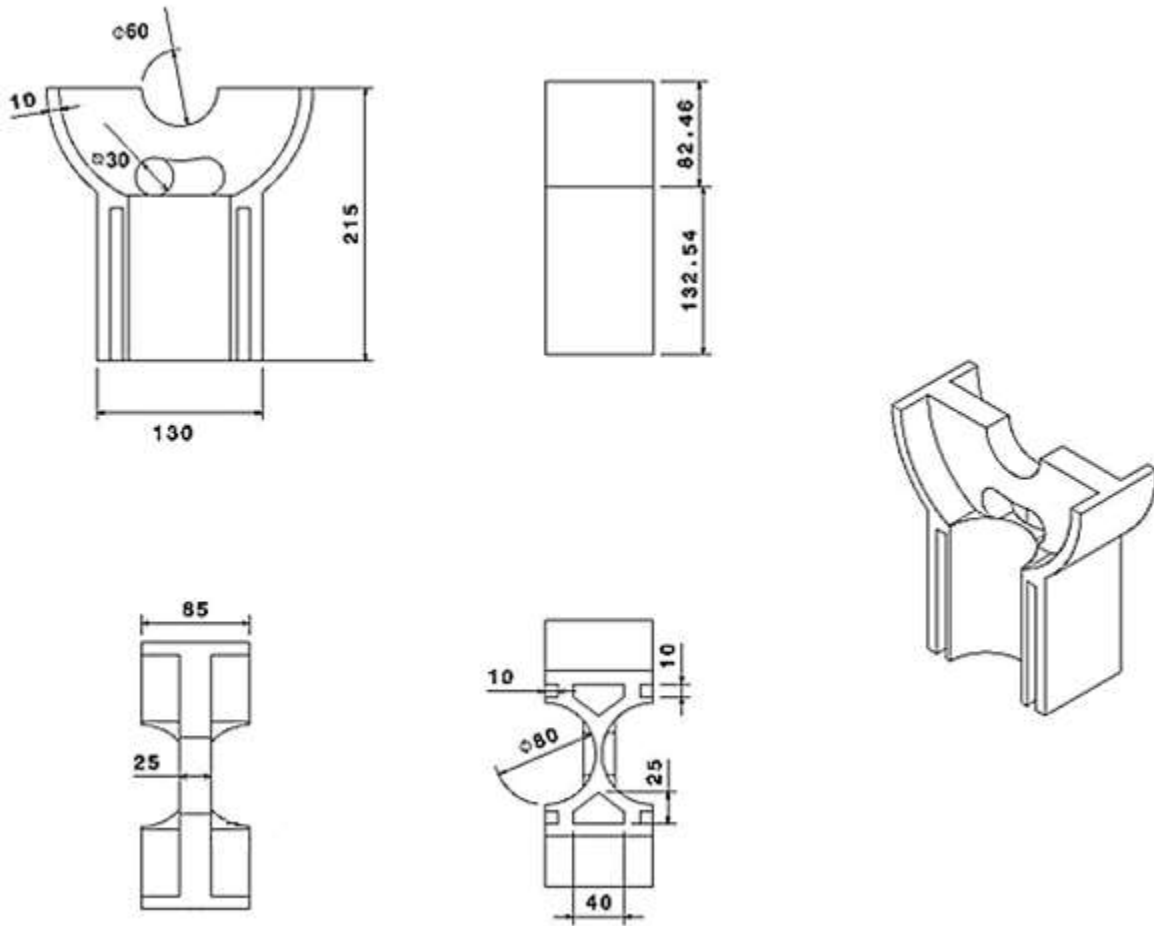


Figure 4.3: Geometry of the simplified engine block section fabricated at Highland Ltd. (dimensions in mm)

4.3. The Geometries of The Solid Chill and The Water-Cooled Chill

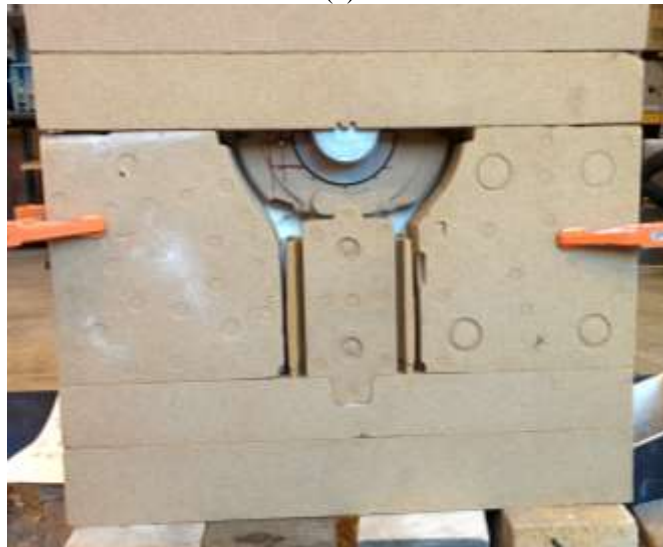
Figure 4.4 shows photographs of the solid chill (a - c) and a dimensioned drawing of the solid chill (d) that is currently being used at GM for their test castings. Note that the original GM solid chill came with two additional, optional, arch extensions (Figure 4.4 (b)). These arch extensions were set up in one of the two GM mould packages which was used for the solid chill casting. The arch extensions were not used in the Highland Foundry moulds to simplify the system.



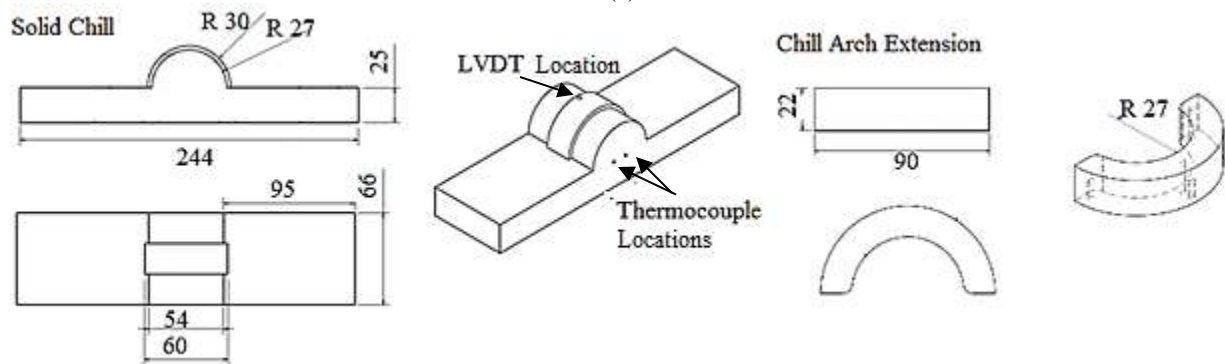
(a)



(b)



(c)



(d)

Figure 4.4: a) H13 solid chill, b) side arch, c) the assembly of the solid chill and one of the two arches in the mould package, and d) dimensioned drawing of the solid chill and the solid chill arch extension for GM solid chill casting (dimensions in mm)

Photographs of the water-cooled chill are shown in Figure 4.5 (a) and (b), and a dimensioned drawing of the chill is presented in Figure 4.5 (c). The water-cooled chill was designed based on preliminary experimental and modelling results as a part of this research at UBC. Both the chills were made of H13 tool steel, which is the material currently used in industry. The same chills were used in all the experiments in this research.

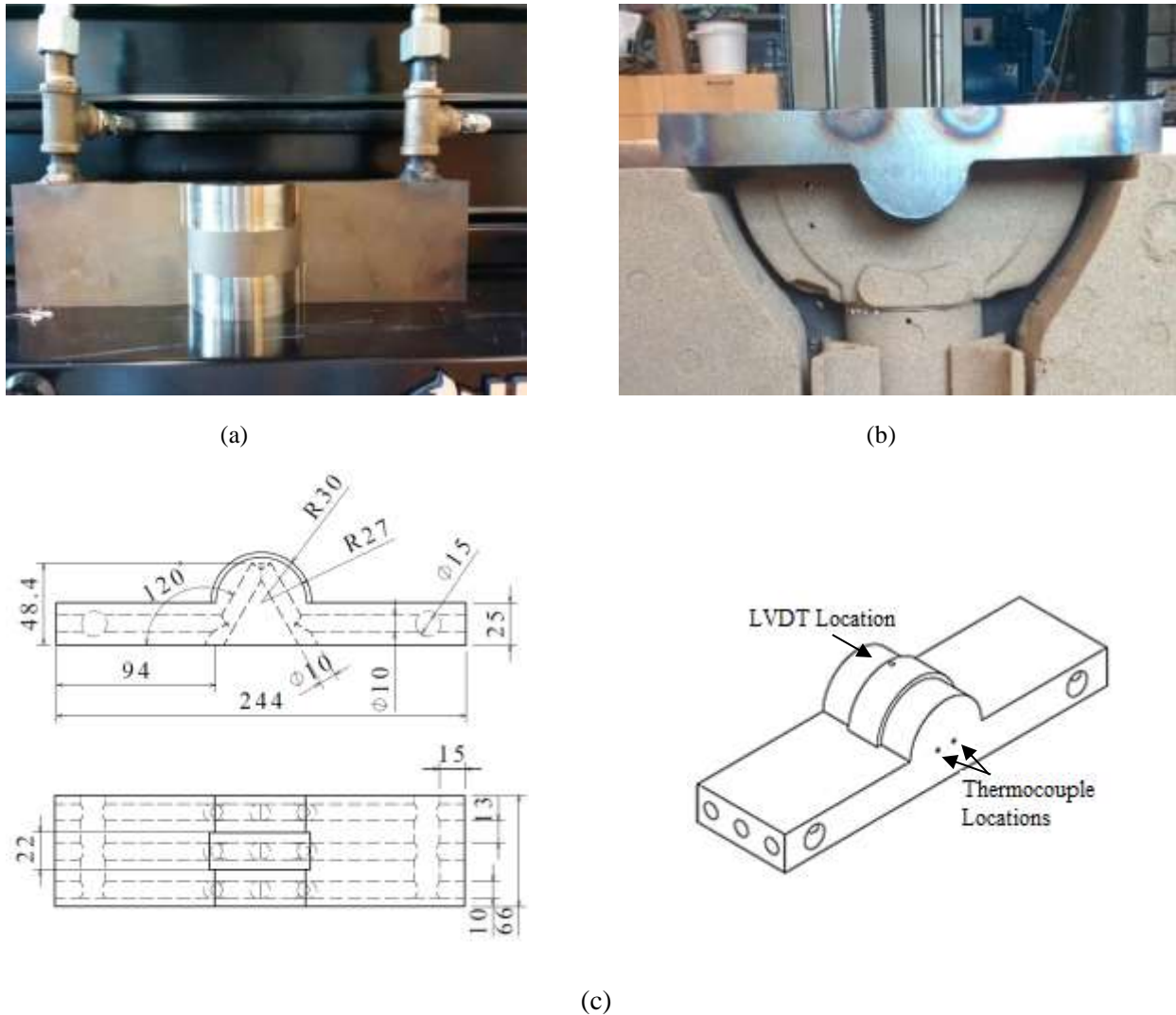


Figure 4.5: a) H13 water-cooled chill, b) the place of the water-cooled chill in the mould system, c) dimensioned drawing of the water-cooled chill (dimensions in mm)

4.4. LVDT Installation

The evolution in the displacements of the casting and the chill at the casting-chill interface were measured by using two LVDTs (Schaevitz – HR 050, resolution: $\sim 0.76 \mu\text{m}$). Quartz tubes (quartz

has a very low coefficient of linear thermal expansion: $\sim 0.5 \times 10^{-6} \text{ } ^\circ\text{C}^{-1}$) were cemented to the transducer cores that extended through the mould package: one was inserted into a hole drilled in the chill and terminating approximately 2 mm from the hot face at the bottom of the chill arch; and the other, passed through a second hole drilled in the chill, protruding about 2 mm into the mould cavity underneath the chill arch – see Figure 4.6. The LVDT intrinsic sources of error are:

- 1) The $\pm 0.25\%$ full stroke (LVDT coil length) linearity error (the largest intrinsic error); and
- 2) The noise produced by the AC line-powered analogue signal conditioner, ATA 2001, which can reach to a maximum value of $\sim 0.76 \text{ } \mu\text{m}$.

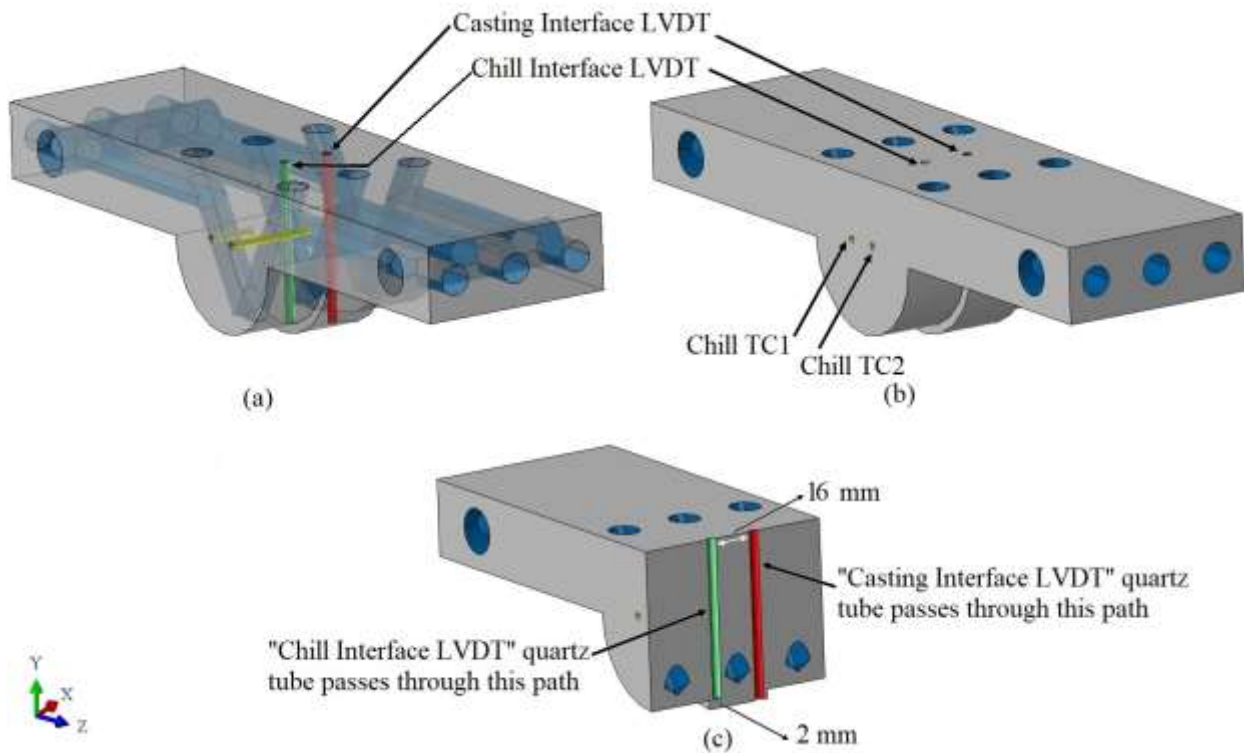


Figure 4.6: a) Transparent view of the water-cooled chill with the locations of casting and chill interface LVDTs and the chill thermocouples, b) solid view of the water-cooled chill with the locations of casting and chill interface LVDTs and the chill thermocouples, c) solid view of the water-cooled chill cut in half on the XY plane with the locations of casting and chill interface LVDTs (the same LVDT and thermocouple locations were drilled in the solid chill).

To track the temperature change in close proximity to the interface, two type K thermocouples, sheathed in alumina, were inserted vertically through the transducer core-quartz tube assemblies.

The installation of the LVDTs was one of the most challenging parts of the experimental procedure, owing to the sensitivity of the LDVTs to any movement and vibration affecting the casting setup, which is one potential source of error in LVDT readings. The LVDTs consist of a ferromagnetic core, placed in a coil, which transforms displacement from a reference position to a proportional voltage. Since friction can significantly affect the displacement results, special care was needed to make sure that the core and the coil were installed parallel to each other and there was no point of contact between them to reduce any possible errors in the measurements (the diameter of the core is ~3 mm less than the inner diameter of the coil).

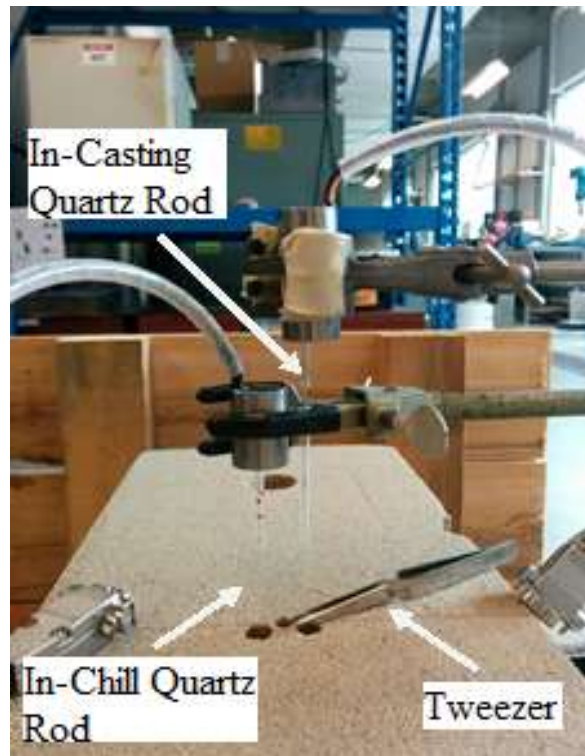
Another challenge with the LVDTs was how to fix them spatially. For the first of the two GM moulds, the chill interface LVDT was held in-place free of the mould package, using a tool stand, and the casting interface LVDT was mounted to the top of the mould package (this was done principally to allow alignment of the two LVDT-quartz rod assemblies, as there was insufficient room on top of the mould package to place both and align the quartz probes with the holes in the chill). The results of this testing clearly identified a problem with this set-up, as the LVDT fixed to the mould package was displaced vertically upward as the sand mould package heated up and expanded, whereas, the transducer mounted on the tool stand was not. Thus, casting interface LVDT was measuring a combination of movement of the casting and expansion of the mould package. To address this issue, it was clear that both transducers needed to be mounted free from the mould package, and held in place by tool stands, so that only the quartz probe tip displacements were being measured – see Figure 4.7. Finally, in the case of the casting interface probe, a tweezer was used to hold the quartz rod-core assembly in place initially to stop the core and quartz rod from falling into the mould cavity prior to pouring – see Figure 4.7 (c). The tweezers were released as soon as the casting interface thermocouple reached the dendrite coherency point (when the cast metal in proximity to the interface developed some mechanical rigidity).



(a)



(b)

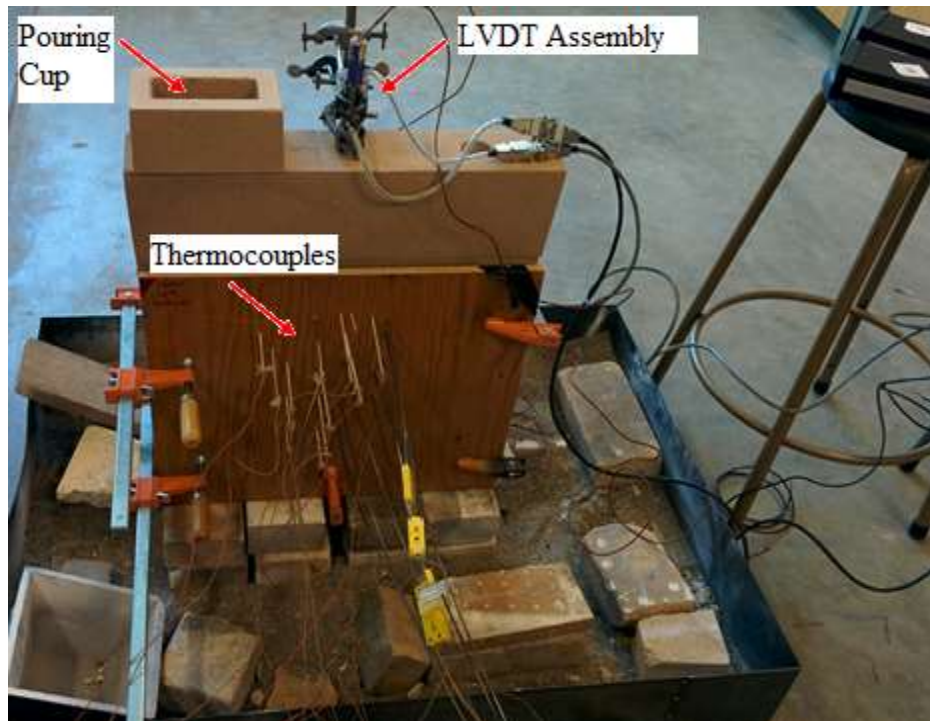


(c)

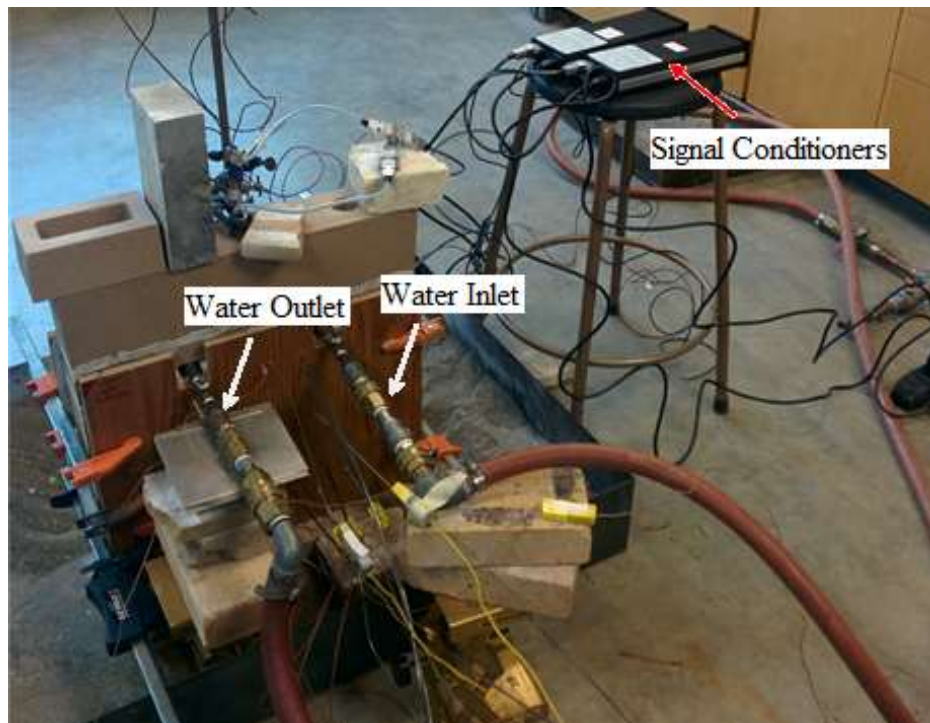
Figure 4.7: LVDT installation process, a) the chill LVDT side view, b) the chill LVDT top view, c) complete LVDT assembly

The temperature-time data for all the thermocouples and the displacement data from the two LVDTs were recorded at a frequency of 4 Hz, with the use of “Lab View¹” software. Figure 4.8 and Figure 4.9 show the full setup of the solid chill and the water-cooled chill castings for the GM mould package and for the Highland mould package, respectively.

¹ Labview is a trademark of National Instruments Corporation.

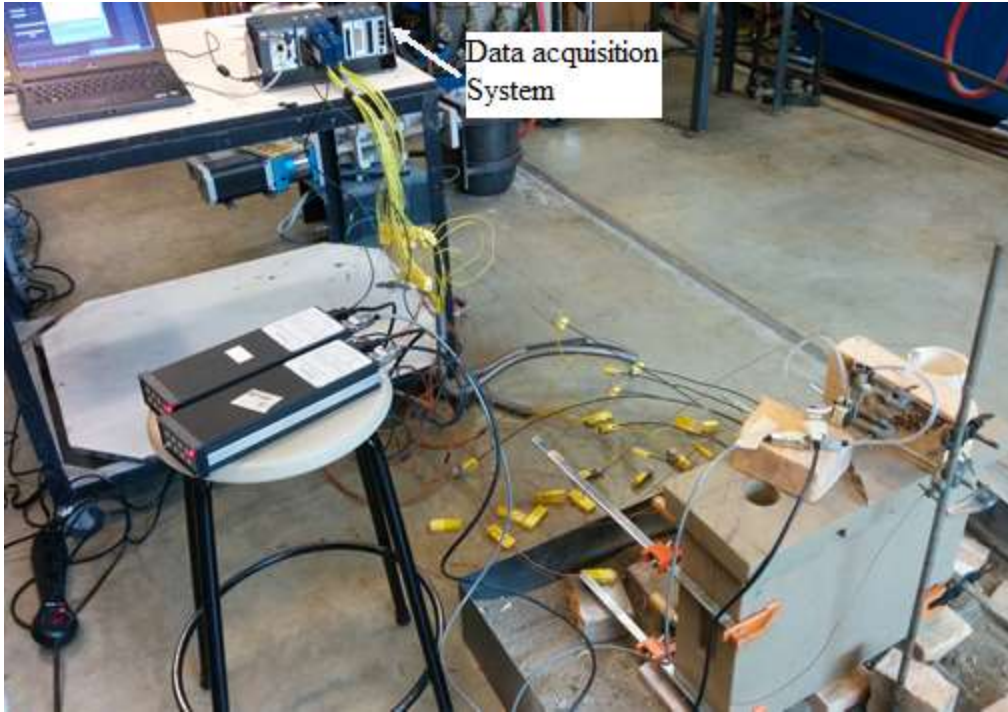


(a)



(b)

Figure 4.8: Full GM mould casting setup a) solid chill, b) water-cooled chill



(a)



(b)

Figure 4.9: Full Highland mould casting setup a) solid chill, b) water-cooled chill

4.5. Liquid Metal Pouring Process

In this research, A319 aluminium alloy was used, which is widely used for the commercial production of engine blocks and cylinder heads in North America. The alloy composition was presented earlier in Table 2.1.

In order to fill each mould, batches of 6.5 kg of the A319 alloy were melted in a silicon carbide crucible in an electrical top-loading ESTRIN furnace model Q3C.

Once the metal reached approximately 780 °C, the crucible was carefully removed from the furnace and fixed in place in the pouring jig. The metal was then skimmed of dross and left to cool and the pouring procedure for all the castings started once the molten metal reached a temperature of 750±5 °C. The pour temperature was measured using a type K thermocouple probe inserted into the molten metal. It took approximately 10 seconds to pour the melt into the mould cavity.

Three different casting conditions were examined: 1) solid chill; 2) water-cooled chill; 3) delayed water-cooled. In the water-cooled experiments, the water was switched on simultaneously with the start of the pouring process, and in the delayed water-cooled experiments, the water was switched on 10 seconds after the completion of the pouring process (the delay time was chosen based on previous work [10]). The water flow rate in the chill water inlet was set to 35 L·min⁻¹ (measured with an inline water flow meter). The temperature of the main water supply was fairly constant at ~7 °C.

To be fully consistent with the Cosworth process, the mould package would have had to have been rolled over once filled. The mould rollover was not utilized in these experiments due to: 1) the use of the LVDT sensors; and 2) safety concerns and the lack of suitable equipment for rotating the mould.

4.6. Metallography Test

To investigate the effect of variation in cooling rate on the SDAS in the bulkhead area, twelve 10×10×5 mm metallographic specimens were taken from 5, 10, 15, and 20 mm from the chill at three angular locations on the arch: 1) along a line at 45° from the top surface of the chill; 2) along a line at 90°; and 3) along a line 135° – see Figure 4.10.

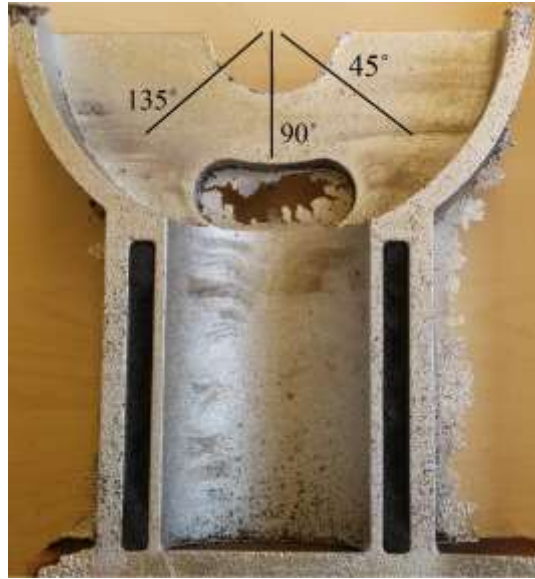


Figure 4.10: Locations for metallography test samples

The metallography samples were polished down to $0.5\ \mu\text{m}$ and etched using 0.5% HF solution. Metallographic images were taken with a “Nikon Epiphot 300” optical microscope, equipped with a “QImaging” digital camera. The secondary dendrite arm spacing was measured in each sample (150 measurements per sample) using “ImageJ” software and the “line intercept” method. These measurements were taken as representative measurements of the microstructural length scale.

5. Model Development

The ABAQUS-based thermal-stress model developed in this research for analysis of the role of gap development on heat transfer at the casting-chill interface is presented in this Chapter. The model formulation consists of three main sections: 5.1) governing equations; 5.2) preliminary 2-D model development; 5.3) three-dimensional model development. The 2-D and 3-D model development sections contain: 1) model domain(s); 2) initial conditions; 3) boundary conditions; 4) material properties, 5) the solution technique and mesh. The last section of the 2-D model development includes the 2-D model results, and the last section of the 3-D model development presents the 3-D model fitting parameters.

5.1. Governing Equations

Coupled thermal-stress models of the casting, the chills, and the mould were developed in the commercial finite element package “ABAQUS” version 2016, for the experiments done with the two chill configurations – the solid chill and the water-cooled chill. The decision to work with ABAQUS was made because of its superior ability to handle contact interface boundary conditions and its ability to also undertake a coupled thermal-stress analysis. The latter capability is essential to be able to predict the evolution of the gap and/or pressure at the casting-chill interface. Mould filling and fluid flow have been ignored in the current analysis.

Due to the fact that casting processes are time dependent processes, the analysis had to be a transient analysis in order to be able to report the temperature change with time in the whole domain.

5.1.1. Thermal Analysis Formulation

Equation 5.1 is the governing partial differential equation of heat transfer for a three-dimensional case:

$$\rho(T)C_p(T)\frac{dT}{dt} = \frac{\partial}{\partial x}(k(T)\frac{\partial T}{\partial x}) + \frac{\partial}{\partial y}(k(T)\frac{\partial T}{\partial y}) + \frac{\partial}{\partial z}(k(T)\frac{\partial T}{\partial z}) + \dot{Q} \quad \text{Equation 5.1}$$

where $\rho(T)$ ($kg\cdot m^{-3}$) is the temperature dependent density, $C_p(T)$ ($J\cdot K^{-1}\cdot kg^{-1}$) is the temperature dependent specific heat capacity, T (K) is temperature, $k(T)$ ($W\cdot m^{-1}\cdot K^{-1}$) is the temperature

dependent thermal conductivity, \dot{Q} ($J \cdot m^{-3} \cdot s^{-1}$) is the heat generation rate per unit volume which accounts for the release of latent heat as an internal heat source, t (s) is the time, and x , y , and z (m) are the coordinates. Note: all the material properties are independent of direction since the material has been defined as an isotropic material.

5.1.2. Stress Analysis Formulation

The general three-dimensional force equilibrium partial differential equations for a solid in a state of stress are:

$$\frac{\partial \sigma_x}{\partial x} + \frac{\partial \tau_{xy}}{\partial y} + \frac{\partial \tau_{xz}}{\partial z} = F_x \quad \text{Equation 5.2}$$

$$\frac{\partial \sigma_y}{\partial y} + \frac{\partial \tau_{xy}}{\partial x} + \frac{\partial \tau_{yz}}{\partial z} = F_y \quad \text{Equation 5.3}$$

$$\frac{\partial \sigma_z}{\partial z} + \frac{\partial \tau_{xz}}{\partial x} + \frac{\partial \tau_{yz}}{\partial y} = F_z \quad \text{Equation 5.4}$$

where σ_x , σ_y , and σ_z (Pa) are the normal stresses in x , y , and z (m) directions, respectively, the τ_{ij} (Pa) are shear stresses acting in j direction, on a plane with normal in i direction, and F_i ($N \cdot m^{-3}$) are internal body forces per unit volume acting in i direction.

In order to solve Equation 5.2 to Equation 5.4, for a body subject to boundary conditions (3 equations with 6 unknowns), the so-called ‘‘compatibility conditions’’ must be satisfied in three dimensions. The compatibility equations that confirm gaps and/or overlaps do not form when a continuum body is deformed under the applied loads, are:

$$\frac{\partial^2 \varepsilon_{xx}}{\partial y^2} + \frac{\partial^2 \varepsilon_{yy}}{\partial x^2} = 2 \frac{\partial^2 \varepsilon_{xy}}{\partial x \partial y}, \quad \frac{\partial^2 \varepsilon_{zz}}{\partial x \partial y} = \frac{\partial}{\partial z} \left[\frac{\partial \varepsilon_{yz}}{\partial x} + \frac{\partial \varepsilon_{zx}}{\partial y} - \frac{\partial \varepsilon_{xy}}{\partial z} \right] \quad \text{Equation 5.5}$$

$$\frac{\partial^2 \varepsilon_{yy}}{\partial z^2} + \frac{\partial^2 \varepsilon_{zz}}{\partial y^2} = 2 \frac{\partial^2 \varepsilon_{yz}}{\partial y \partial z}, \quad \frac{\partial^2 \varepsilon_{xx}}{\partial y \partial z} = \frac{\partial}{\partial x} \left[-\frac{\partial \varepsilon_{yz}}{\partial x} + \frac{\partial \varepsilon_{zx}}{\partial y} + \frac{\partial \varepsilon_{xy}}{\partial z} \right] \quad \text{Equation 5.6}$$

$$\frac{\partial^2 \varepsilon_{zz}}{\partial x^2} + \frac{\partial^2 \varepsilon_{xx}}{\partial z^2} = 2 \frac{\partial^2 \varepsilon_{xz}}{\partial x \partial z}, \frac{\partial^2 \varepsilon_{yy}}{\partial x \partial z} = \frac{\partial}{\partial y} \left[\frac{\partial \varepsilon_{yz}}{\partial x} - \frac{\partial \varepsilon_{zx}}{\partial y} + \frac{\partial \varepsilon_{xy}}{\partial z} \right] \quad \text{Equation 5.7}$$

Equation 5.5 to Equation 5.7 are the relationships between the strains, which ensure that the body remains compatible and continuous after deformation.

In the stress analysis, ABAQUS first calculates the displacements at the nodes (the field variable). The system of equations that is solved to yield the displacement field is based on the integral form of Equation 5.2 to Equation 5.4 formulated to describe the potential (strain energy). The solution sought is one that minimizes the potential energy of the system. The integral equations require the variation in the displacement field within the domain of an element to be assumed (the so-called interpolation or shape functions).

Once the displacement field is known, the terms comprising the three-dimensional strain tensor may be calculated at a point within a given element (and therefore the domain), using the following equations (knowing the nodal displacements and the shape functions):

$$\varepsilon_x = \frac{\partial u}{\partial x}, \varepsilon_y = \frac{\partial v}{\partial y}, \varepsilon_z = \frac{\partial w}{\partial z} \quad \text{Equation 5.8}$$

$$\varepsilon_{xy} = \frac{1}{2} \left(\frac{\partial v}{\partial x} + \frac{\partial u}{\partial y} \right), \varepsilon_{xz} = \frac{1}{2} \left(\frac{\partial w}{\partial x} + \frac{\partial u}{\partial z} \right), \varepsilon_{zy} = \frac{1}{2} \left(\frac{\partial v}{\partial z} + \frac{\partial w}{\partial y} \right) \quad \text{Equation 5.9}$$

where ε_x , ε_y , and ε_z are normal strains, the ε_{ij} are shear strains, and v , u , and w (m) are displacements in x , y , and z directions, respectively. The strains are “elemental” quantities and may be evaluated at nodes by a process of extrapolating the in-element strains to the nodes and then averaging the values associated with the adjacent elements.

Prior to calculation of the stress, any inelastic strains must first be removed – e.g. due to plastic or creep deformation – as follows:

$$\{\Delta \varepsilon_{el}\} = \{\Delta \varepsilon\} - \{\Delta \varepsilon_{pl}\} \quad \text{Equation 5.10}$$

where $\{\Delta\varepsilon_{el}\}$ is the elastic strain increment vector, and $\{\Delta\varepsilon_{pl}\}$ is the plastic strain increment vector. For rate in-dependent plasticity, ABAQUS uses “associated flow” in which the direction of accumulation of plastic strain is the same as the outward normal to yield surface. The resulting elastic strain can then be used to calculate the normal and shear stresses using Hooke’s law – see Equation 5.13. As the stresses are also elemental based quantities, the same process can be used for their evaluation at the nodes, as was applied for nodal strain evaluation.

In problems involving a change in temperature such as the current problem, the changes in the temperature will generally result in either expansion or contraction of the body. For homogeneous and isotropic materials, a temperature change of ΔT will result in a linear uniform strain in all the dimensions:

$$\varepsilon_x = \varepsilon_y = \varepsilon_z = \alpha \cdot \Delta T \quad \text{Equation 5.11}$$

where α ($^{\circ}C^{-1}$) is the coefficient of linear thermal expansion of the material. The thermal strain is first converted to a body load and added to any other loads (surface traction, gravity, etc.) present in the system prior to solving for the displacement field. The thermal strain is then removed along with any inelastic loads prior to solving for the elastic strain and stress as follows:

$$\{\Delta\varepsilon_{el}\} = \{\Delta\varepsilon\} - \{\Delta\varepsilon_{pl}\} + \{\Delta\varepsilon_{th}\} \quad \text{Equation 5.12}$$

where $\{\Delta\varepsilon_{th}\}$ is the thermal strain increment vector.

The relationship between the elastic strain increment vector and the stress obeys Hooke’s law:

$$\{\Delta\sigma\} = [D]\{\Delta\varepsilon_{el}\} \quad \text{Equation 5.13}$$

where $[D]$ is the stiffness tensor containing temperature dependent elastic modulus, E (MPa), and Poisson’s ratio, ν .

The constitutive behaviour of A319 alloy was defined as a temperature dependent elastic-perfectly plastic behaviour in the current analysis. The data describing the stress-strain response of A319 as a function of temperature is presented later in Section 5.2.4.

5.1.3. Coupled Thermal-Stress Analysis Formulation

The general form of the fully coupled temperature-displacement system of equations that ABAQUS solves for is of the following form:

$$\begin{bmatrix} K_{uu} & K_{u\theta} \\ K_{\theta u} & K_{\theta\theta} \end{bmatrix} \begin{Bmatrix} \Delta u \\ \Delta \theta \end{Bmatrix} = \begin{Bmatrix} R_u \\ R_\theta \end{Bmatrix} \quad \text{Equation 5.14}$$

where Δu and $\Delta \theta$ are the respective corrections to the incremental displacement and temperature, K_{ij} are the submatrices of the fully coupled Jacobian matrix, and R_u and R_θ are the mechanical and thermal residual vectors, respectively.

The current coupled thermal-stress model is highly non-linear. Sources of non-linear behaviour include the transient heat flow equation, the implementation of temperature dependent thermo-physical and mechanical properties, and temperature and/or displacement dependent boundary conditions. To solve the nonlinear coupled temperature-displacement system of equations (Equation 5.14) simultaneously, ABAQUS uses Newton's method. Furthermore, ABAQUS adopts an implicit backward-difference scheme for time integration of temperatures and displacements.

5.2. Preliminary Two-Dimensional Model Development

To develop the model of the actual experimental casting configuration, a step-by-step approach was taken in which model complexity, in terms of geometry, boundary conditions (thermal and mechanical), and material properties (mechanical behaviour) were added incrementally based on a simplified two-dimensional model. The goal was to develop a foundation, or framework, using a relatively quick to run 2-D model, that could then be applied to the development of the 3-D model. Key issues centred on the mechanical boundary conditions (constraints) and the mechanical properties (constitutive behaviour) of A319 and the bonded sand mould. This approach also allowed some aspects of a traditional sensitivity analysis to be completed.

5.2.1. Two-Dimensional Model Domain

Figure 5.1 shows the model domain for the two-dimensional analysis. The domain represents a 2-D, YZ plane, bisecting the main bearing bulkhead with the cylinder projected onto the plane. To reduce the computational size of the problem, the following four additional assumptions were made:

1. The model domain is based on the geometry of the mould package that was fabricated at Highland foundry, which is a simpler geometry.
2. The geometries of the gating system and the riser are not included in the analysis domain.
3. Symmetry is assumed about XY plane bisecting the casting.
4. The two-dimensional model is based on the solid chill experiment.

The geometries of the engine block section, the chill, and the mould were created in ABAQUS CAE.

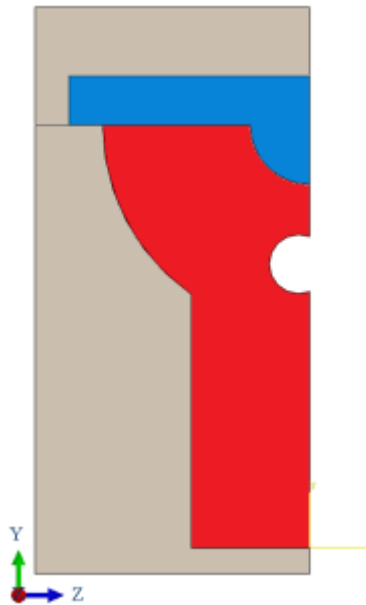


Figure 5.1: The two-dimensional model domain with the sand, solid chill and casting geometries

5.2.2. Initial Conditions

As was mentioned earlier in this Chapter, the model is a fully coupled thermal-stress model that does not include the pouring process and fluid flow. Therefore, the thermal-stress simulation in the casting process begins when the mould cavity is full of molten metal. The initial temperatures

of the various components including the casting, the chill, and the sand were taken from the thermocouple data that were recorded during the experiments and were assumed to be uniform in the three domains. These initial temperatures are reported in Table 5.1.

Table 5.1: Initial conditions applied to the casting, the chill and the sand mould

The Domain	Casting	Solid Chill	Sand Mould
Temperature (°C)	610	20	35

For the stress model, the material was assumed to be in an initial state of zero strain and zero stress.

5.2.3. Basic Symmetry Boundary Conditions Applied to the 2-D Model

In a thermal-stress analysis, there are two types of boundary conditions that must be developed/formulated: the first, pertaining to the calculation of the heat balance and the evolution of the temperature field; and the second, pertaining to the calculation of force equilibrium and the evolution of the displacement field. The thermal and stress boundary conditions include definitions for the symmetry boundaries and interface boundaries (component-to-component, and component-to-environment). Of these, the symmetry boundaries are the most straightforward. Figure 5.2 shows the symmetry boundaries for the thermal and the stress analysis in which $U_z (m)$ is displacement in Z direction, UR_i are rotational displacements about i axis. The descriptions of the various interface boundaries examined during the development of the 2-D model are presented in Section 5.2.6 in a series of case studies.

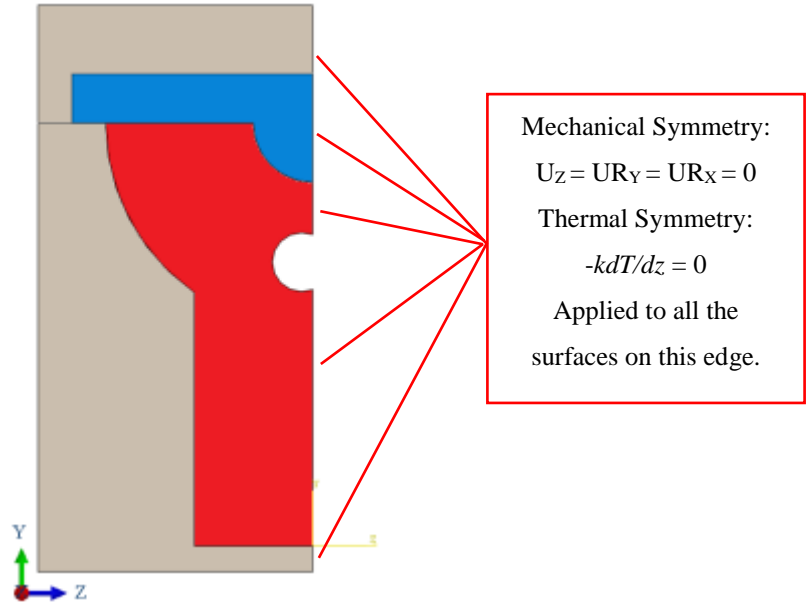


Figure 5.2: 2-D model domain with basic symmetry boundary conditions

5.2.4. Material Properties

The thermo-physical and mechanical properties of A319, H13 tool steel, and bonded silica sand needed to be implemented into the model were taken from the values reported in the literature, and are summarized in Table 5.2 and Table 5.3, respectively. All these materials have been defined as being homogeneous and isotropic. The Poisson's ratio was assumed to be 0.33 for each of the three materials. The latent heat was assumed to be released linearly within a series of temperature ranges between the liquidus (610 °C) and solidus (504 °C) temperatures, in proportion to the evolution of fraction solid [98,99].

Table 5.2: Thermo-physical properties of A319 alloy, bonded silica sand, and copper [31,98,100,101]

Material	T (°C)	α (°C ⁻¹)	ρ (kg·m ⁻³)	k (W·m ⁻¹ ·K ⁻¹)	C _p (J·kg ⁻¹ ·K ⁻¹)	T (°C)	L (kJ·kg ⁻¹)
A319	25	2.8×10 ⁻⁵	2750	137	830	610-565	220
	100	2.8×10 ⁻⁵	2737	155	900	565-540	136
	200	2.8×10 ⁻⁵	2717	163	950	540-525	16
	300	2.8×10 ⁻⁵	2693	164	980	525-504	28
	400	2.8×10 ⁻⁵	2668	179	1120		
	500	2.8×10 ⁻⁵	2646	175	1200		
	504	2.8×10 ⁻⁵	2640	150	1090		
	610	0	2492	70	1130		
	611	0	2492	70	1170		
H13	10	1.24×10 ⁻⁵	7800	25	459		
	400	1.24×10 ⁻⁵	7700	29	588		
	600	1.24×10 ⁻⁵	7600	29	726		
Bonded Silica Sand	25	5×10 ⁻⁶	1602	1.04	760		
	95	5×10 ⁻⁶	1602	1.04	810		
	96	5×10 ⁻⁶	1602	1.04	11230		
	104	5×10 ⁻⁶	1602	1.04	11230		
	105	5×10 ⁻⁶	1602	1.04	820		
	550	5×10 ⁻⁶	1602	0.73	1070		

For the various case studies associated with the development of the 2-D model, temperature dependent thermo-physical properties have been adopted. In the case of the mechanical properties of A319 and bonded silica sand, an incremental approach was adopted starting first with temperature independent elastic behaviour before moving on to temperature dependent elastic behaviour for A319 and bonded silica sand, and finally, temperature dependent elastic-perfectly plastic behaviour for A319.

In Table 5.3, the literature based values for the elastic modulus and yield stress are shown as a function of temperature up to 400 °C. At temperatures above 400 °C, the elastic modulus and yield stress were assumed to decrease with increasing temperature as shown in the Table 5.3. The approach used to decrease the elastic modulus and yield stress follows reference [102]. Beyond 504 °C (the solidus temperature of the A319 alloy) these quantities are temperature invariant. (Note: ABAQUS requires a finite value for the elastic modulus and yield stress, hence, values of 3.53 GPa and 0.02 GPa are applied for the elastic modulus and yield stress, respectively, in the liquid at temperatures above 504 °C [102]).

Table 5.3: Mechanical properties of A319 alloy, bonded silica sand, and copper [100,103-105]

Material	T (°C)	E (GPa)	T (°C)	σ_y (GPa)
A319	25	76	25	0.16
	100	74	150	0.16
	200	68.8	180	0.149
	300	60.6	240	0.143
	400	49.4	270	0.097
	500	35.3	320	0.063
	504	3.53	370	0.03
			400	0.025
		504	0.02	
H13	10	210		
	400	180		
	600	157		
Bonded Silica Sand	25	3.4		
	125	0.6		
	250	0.6		
	280	1.2		

Several studies [104,106] have reported that the predicted stresses and displacements in thermal-stress models of sand castings are highly sensitive to temperature dependent elastic modulus of the bonded sand. Therefore, part of the 2-D model development focused on exploring the effect of elastic modulus of the bonded silica sand on the interface gap behaviour. According to these studies, the variation of the elastic modulus of bonded sand is very complicated and depends on many factors, such as the type of the binder, the binder setting process, the shape and

size of the sand, the rate of heating of the sand, etc. However, the common behaviour observed in all the different bonded sand moulds is that with an increase in the temperature, the elastic modulus of the bonded sand decreases. Between around 125 °C to 250 °C the elastic modulus remains relatively constant, and at temperatures above 250 °C, the elastic modulus slightly increases. These behaviours are due to the chemical reactions in the binder at elevated temperatures.

5.2.5. Solution Technique and Mesh

ABAQUS version 2016 was used to solve the problem subject to initial and boundary conditions, which are defined in the previous sections of this Chapter. ABAQUS uses the finite element method to solve the governing equations discussed in section 5.1, and hence, the domain is discretized into a mesh containing elements and nodes. The domain was meshed in ABAQUS CAE and the example mesh topographies in the domains are shown in Figure 5.3 for the 2-D model.



Figure 5.3: The mesh topographies in the 2-D model domains

The mesh statistics are summarized in Table 5.4. The element type is consistent with a coupled thermal-plane stress analysis (triangular CPS3T), in which the thermal and displacement fields are assumed to vary linearly over the domain of the element. Note: strains and stresses are consequently constant within an element. Plane stress conditions are assumed to prevail because the through thickness dimension in the 2-D analysis domain (X direction) is much smaller than the

in-plane dimensions (in Y and Z directions). Thus, conditions are approaching plane-stress conditions in which $\sigma_x = 0$ MPa.

Table 5.4: Mesh statistics, 2-D model

Domain	Element Type	Element Shape	Number of Nodes	Number of Elements
Casting	CPS3T ¹	Triangular	1686	3172
Solid Chill			1069	1965
Sand Mould			1166	2153
Sand Cap			1498	2795

The time step was set to be automatically chosen by ABAQUS, given fixed user-defined initial, minimum, and maximum values for the time step. This type of time step control allows ABAQUS to select time increments based on a user-defined maximum allowable temperature change per increment.

5.2.6. Two-Dimensional Model Results

The 2-D model results are presented in a series of Cases, in which each Case presents an exploration of the addition of a step to the complexity of the analysis. Case 1 explores the issues around mechanical constraints and rigid body motion. Case 2 explores issues around the constitutive behaviour of A319 and bonded silica sand, and Case 3 explores issues around heat transfer to the mould package. In Case 3, the residuals of the temperature and the displacement fields were relaxed to explore their effect on the model execution time and accuracy. The results are presented in terms of the behaviour of the casting-chill interface, the central focus of this investigation, and in terms of the behaviour of the displacements and/or stress fields.

Case 1 - The Effect of Mechanical Constraints and the Presence of the Mould

As alluded to previously, one of the main challenges in thermal-stress models is to impose appropriate mechanical constraints to certain locations on the geometry, which prevent rigid body

¹ 3-node plane stress thermally coupled triangle, linear displacement and temperature

motion, while not over constraining the parts in the assembly and allowing them to expand and contract as they do in the actual casting. Two domains were examined in Case 1:

- 1) The bonded sand mould was removed from the assembly – see Figure 5.4 (a); and
- 2) The bonded sand mould was included in the assembly – see Figure 5.4 (b).

For the domain without the mould, in addition to the symmetry constraints, vertical displacement, U_y , has been suppressed on the nodes located on the upper and lower bounds of the circular cut-out (where it intersects the symmetry boundary). This constraint was applied to simulate the effect of the sand core that was fixed to the mould system and was removed from the analysis domain to decrease the computational size of the problem. Displacements in the Y and Z directions have been suppressed in the lower left corner of the chill to approximate the effect of the mould cap. Note that failure to suppress vertical motion in the corner of the chill resulted in rigid body motion. Furthermore, the right bottom corner of the casting was constrained in the Y direction to consider the constraining effect of the mould and the gating system in the experimental setup.

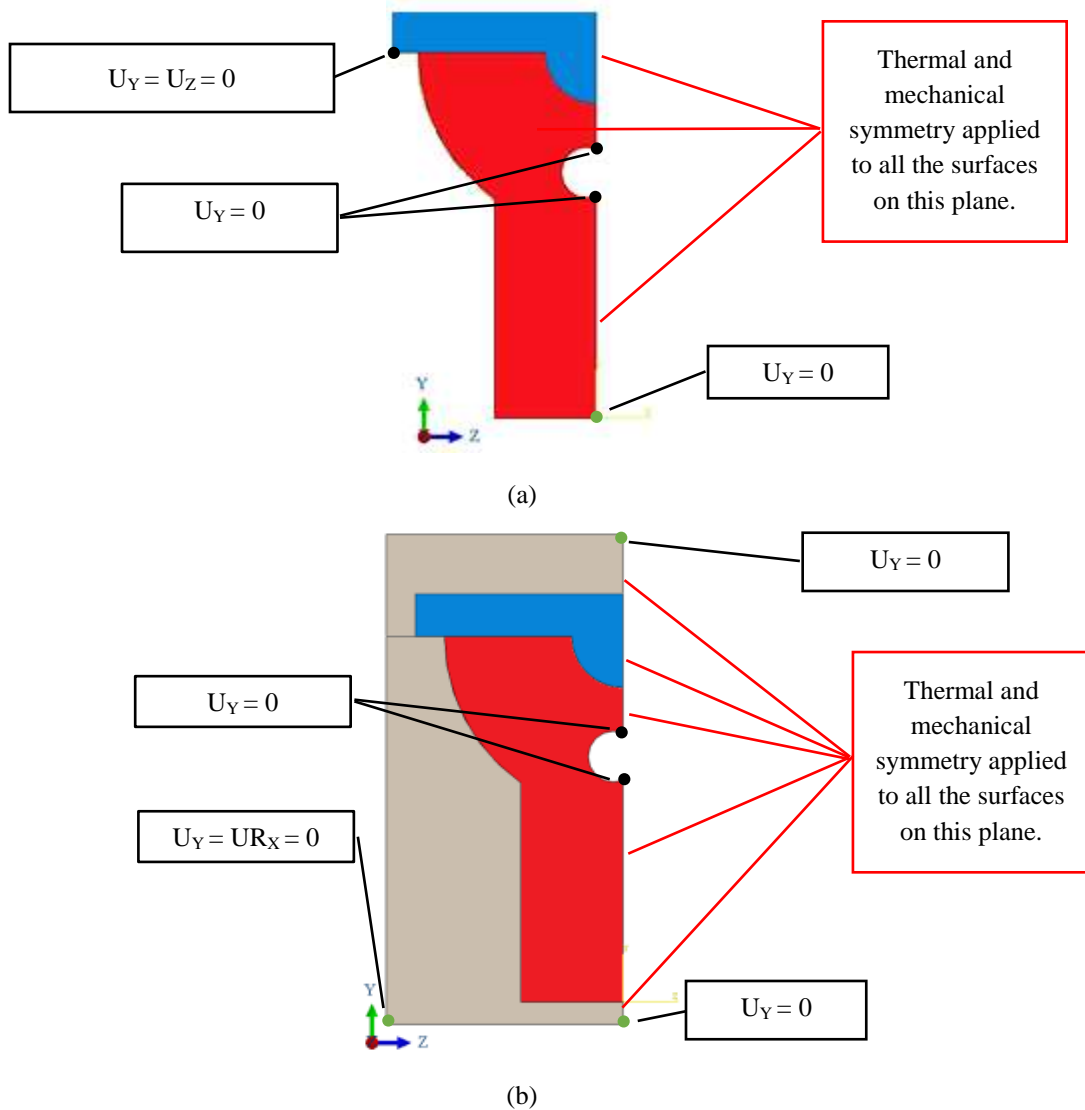


Figure 5.4: Model domain and mechanical constraints applied to Case 1 a) without the mould geometry and b) including the mould geometry

For the domain including the mould, Figure 5.4 (b), vertical displacement, U_y , has been suppressed on the nodes located on the upper and lower bounds of the circular cut-out as in the previous case. Additionally, the top right corner of the mould cap was constrained to suppress motion in the Y direction. The chill displacement has been constrained by defining hard contacts (in ABAQUS hard contact is defined as a contact interface in which no penetration is permitted between the two surfaces) at the boundaries between the sides of the chill and the mould cap. Vertical displacement on the lower right and left corners of the mould have been suppressed to simulate the effect of the gating system. Rotation around X-axis on the lower left corner of the

mould was also constrained to stop twisting. In both models in Case 1, constant elastic moduli (equivalent to the value at room temperature) were defined for A319, the chill, and the bonded sand mould.

The boundaries that represent a contact interface between two hard surfaces (e.g. casting-mould, casting-chill, and chill-mould) in the domain that are exchanging heat are all of the form:

$$-k \frac{\partial T}{\partial n} = h_{Interface}(T_{Surface1} - T_{Surface2}) \quad \text{Equation 5.15}$$

where n , is the direction normal to the surface, $h_{Interface}$ ($W \cdot m^{-2} \cdot K^{-1}$) is the interfacial heat transfer coefficient, $T_{Surface1}$ (K), is the temperature at the point on the surface for which the heat flux is being applied (i.e. the master surface), and $T_{Surface2}$ (K) is the temperature on the opposite side of the interface, adjacent to the point being processed (i.e. the slave surface). The IHTC may be a function of temperature, time, pressure, or the interface gap. In Case 1, the IHTC at the casting-chill boundary, $h_{Interface}$, is formulated as being gap dependent, and to reduce as the gap develops as shown in Figure 5.5. The relationship between gap size and IHTC was obtained by using a trial-and-error method.

The analysis has been limited to only 200 s to yield a reasonable execution time (within an hour). This length of time was found to be sufficient to examine deformation behaviour of the mould package in terms of the magnitude of the gap that formed at the chill-casting interface and whether it made physical sense.

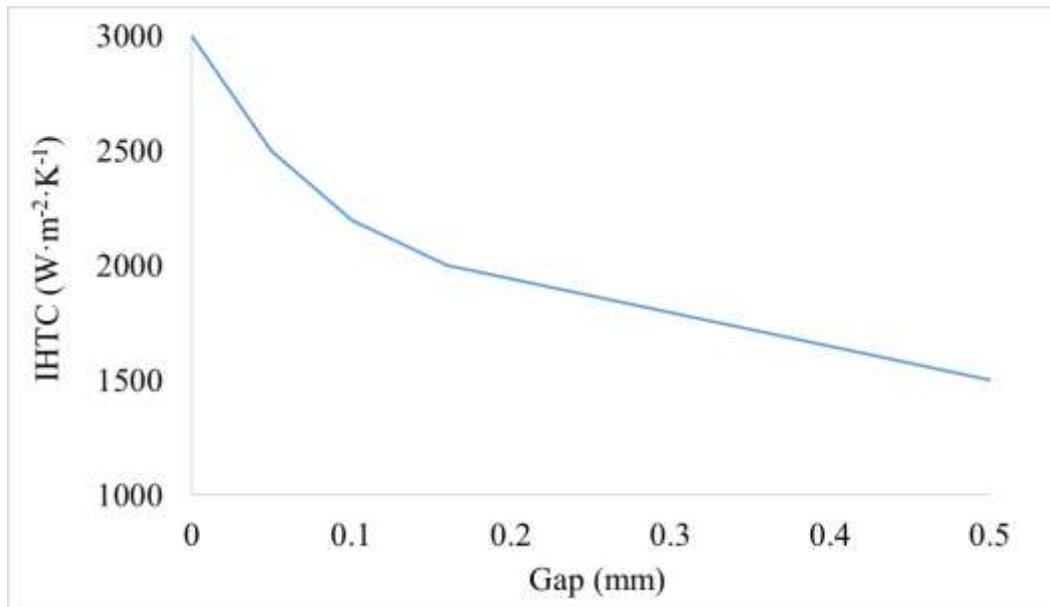


Figure 5.5: Variation of the casting-chill IHTC with interface gap that was implemented to the 2-D model

Figure 5.6 shows the Von-Mises stress contours for Cases 1(a) and 1(b) at 200 s, superimposed on the deformed mesh. Note: the deformation has been magnified by a factor of 10. A larger interface gap between the casting and the chill is predicted in Case 1(a) because the chill is not constrained above the arch and has more freedom to deform and move upward, particularly adjacent to the symmetry boundary. The deformation of the chill develops as a result of the expansion of the face adjacent to the casting. Note: the bending of the chill is exacerbated by pinning the lower left corner of the chill in the Y and Z directions. In contrast, in Case 1(b), the bending of the chill is reduced by the presence of the bonded sand cap allowing some horizontal expansion while suppressing some vertical movement of the chill upward above the arch. Note: in Case 1(b), the chill appears to penetrate into the mould domain. This is an artefact of magnifying the deformation 10 times.

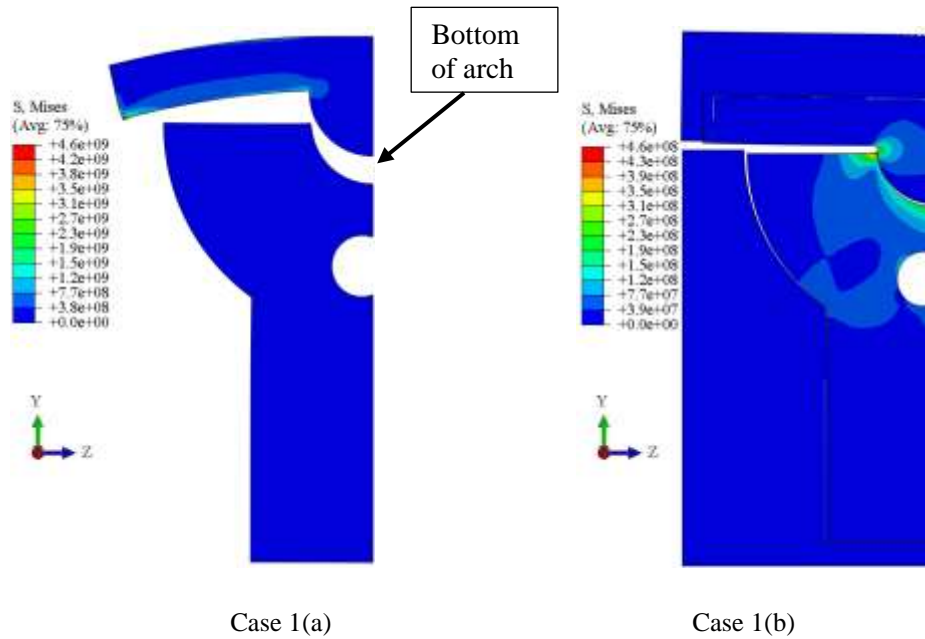


Figure 5.6: Comparison between the Von-Mises stress results at 200 s obtained from Case 1(a) and 1(b) (deformation magnified by 10 times, and the pressure unit is in Pa)

Figure 5.7 presents the results for the evolution of the gap at the casting-chill interface at the bottom of the arch (see Figure 5.6) with time predicted for the two models examined in Case 1. For reference, the gap measured during the experiment using LVDTs has been added to the plot. Note: the details surrounding the LVDT based measurements of the gap size evolution are presented in Chapter 6, Section 6.1. The gap data was added to Figure 5.7 to serve as a reference for conducting a preliminary assessment of the accuracy of the model predictions in the context of the sensitivity analysis.

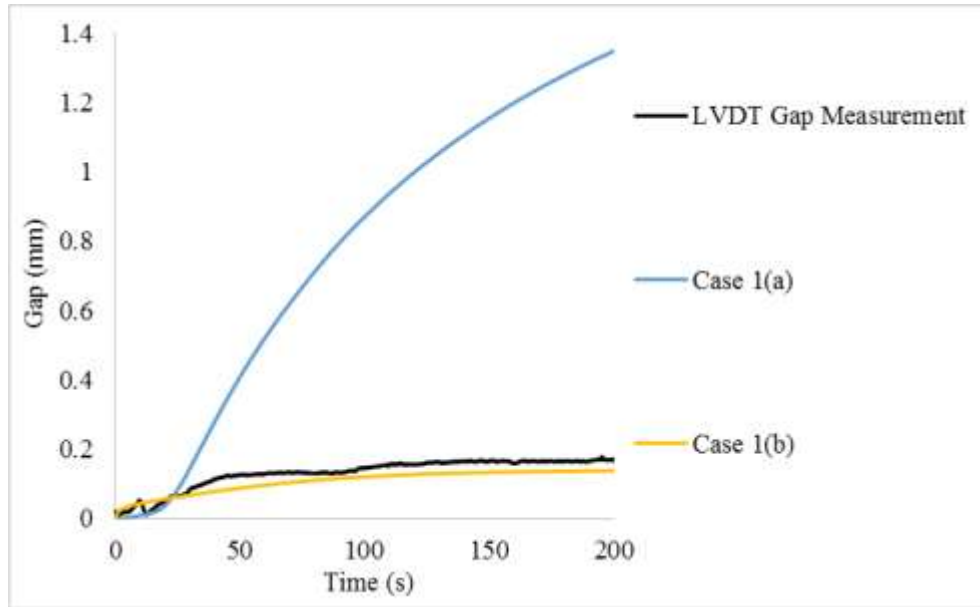


Figure 5.7: Comparison between interface gap behaviours obtained from experiment and models in Cases 1

Comparing the results obtained from the two models and the experimental results indicates that a much larger gap forms at the casting-chill interface in the model without the sand mould than the model with it present. Furthermore, the gap magnitude is in the range obtained from the measurements with the constraining influence of the sand cap included. The results of this analysis clearly indicate the following:

- 1) The interplay between the deformation of the casting and chill is complicated and is strongly influenced by the constraining effect of the bonded sand cap;
- 2) The constraints that have been applied to the 2-D domain seem reasonable at this stage as the model appears to be able to reproduce the behaviour of the experimentally determined gap.

To explore Case 1 (b) further, contours of the stress (Von-Mises) have been overlaid on the deformed mesh and are presented in Figure 5.8 at 4 different times during the analysis. Note: the deformation has been magnified by a factor of 10. During the initial stages of the casting process, there is good contact between the casting and the chill, which results in a high heat transfer between the two parts. As a result, the chill starts to thermally expand and the casting starts to contract due to variation in the density of the cast material as a result of solidification. From the results presented in Figure 5.8, it appears that the casting contracts onto the chill at the side of the

arch near the top creating a pinch point. As can be seen, contact pressures develop at this point, and because of the direction of the curvature in the geometry at the interface, the normal component of the pressure at the pinch point pushes the chill up creating a gap at the bottom of the arch. This upward motion of the chill is constrained/moderated by the presence of the bonded sand cap. The pinch point stress continues to increase with time consistent with the gap at the bottom of the arch increasing with time.

In addition to the pinch point stress, the chill is bent upward by the development of thermal stresses as a result of heat being transferred to the chill from the casting. This bending contributes to the development of the gap between the casting and the chill along the horizontal portion of the interface. Note: this moderates with increasing time due to the moderation of the temperature gradient in the chill. Thus, there are two contributing factors to the gap behaviour at the casting-chill interface:

- 1) The development of a pinch point;
- 2) The development of thermal stress induced deformation of the chill.

At this point, the former appears to be responsible for the formation of the gap at the bottom of the arch.

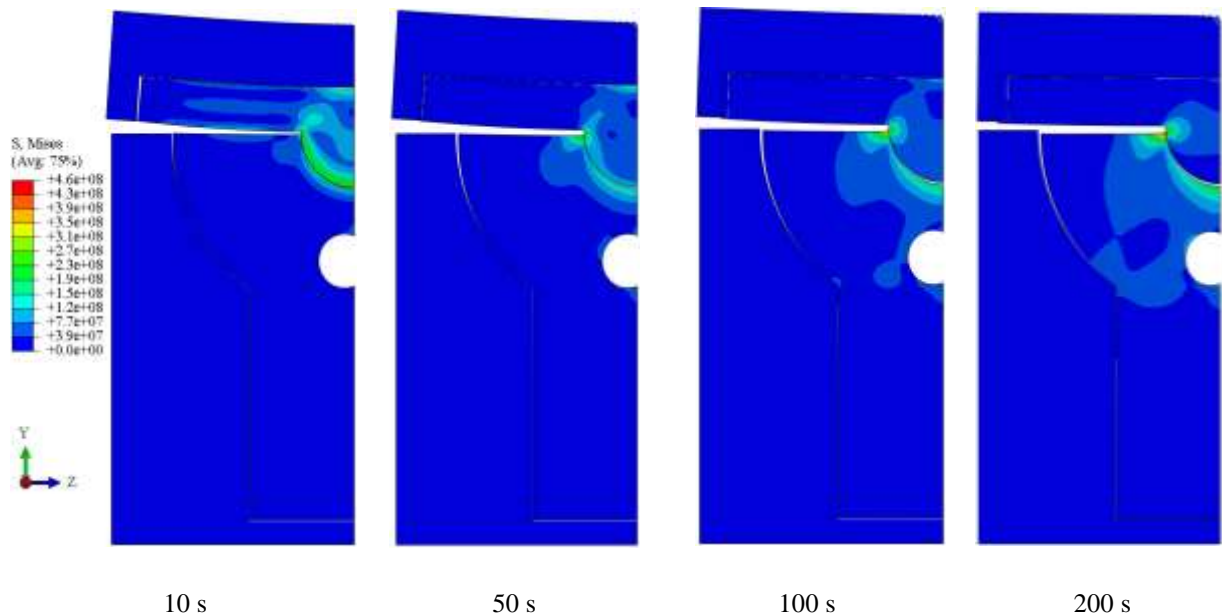


Figure 5.8: Comparison between the Von-Mises stress results obtained from Case 1(b) at different times (deformation magnified by 10 times, and the pressure unit is in Pa)

Case 2 - The Effect of Material's Constitutive Behaviour

To examine the effect of the constitutive behaviour of the materials involved in the analysis on the development of the casting-chill interface gap, five models were formulated. In these models, the effect of temperature on the constitutive behaviours of the materials was gradually introduced. The model domain and the mechanical constraints for this analysis were those of Case 1(b). The following steps in constitutive behaviour complexity were introduced and examined in a series of case studies:

Case 2(a) – Temperature dependent elastic modulus defined up to solidus temperature for A319; constant room temperature elastic modulus for the bonded sand.

Case 2(b) – Temperature dependent elastic and plastic behaviour defined up to solidus temperature for A319; constant room temperature elastic modulus for the bonded sand.

Case 2(c) – Temperature dependent elastic and plastic behaviour defined up to 400 °C for A319; constant room temperature elastic modulus for the bonded sand.

Case 2(d) – Temperature dependent elastic and plastic behaviour defined up to solidus temperature for A319; reduced elastic modulus of silica sand to consider the effect of mould softening when the mould heats up.

Case 2(e) – Temperature dependent elastic and plastic behaviour defined up to 400 °C for A319; reduced elastic modulus of silica sand to consider the effect of mould softening when the mould heats up.

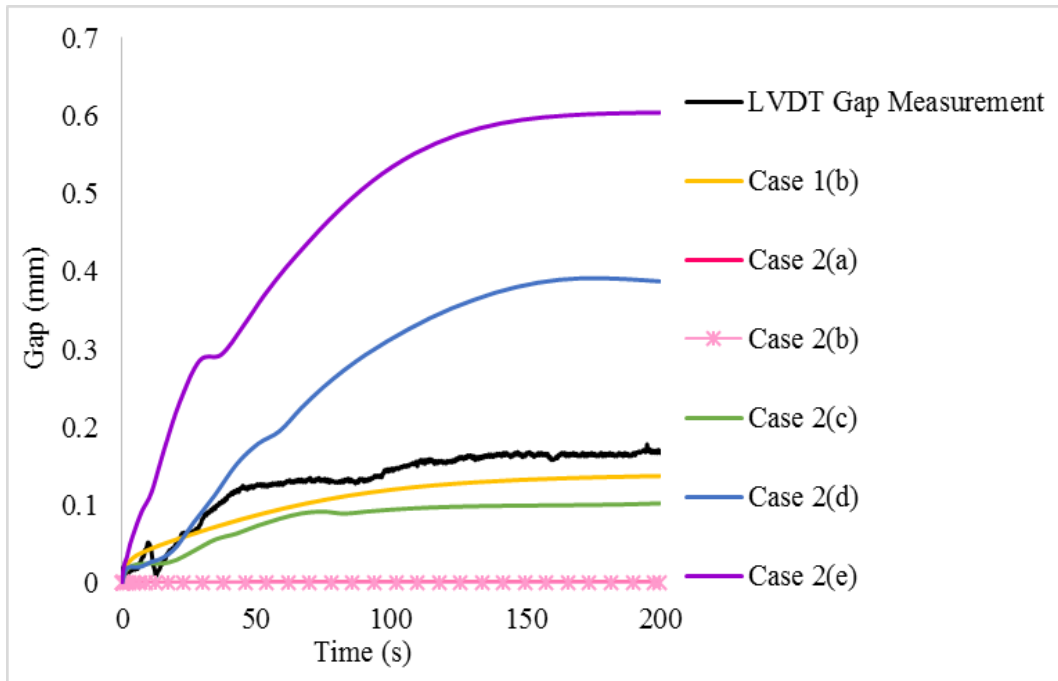


Figure 5.9: Comparison between interface gap behaviours obtained from experiment, Case 1(b), and Cases 2

Figure 5.9 presents the results for the evolution of the gap at the casting-chill interface (bottom of the arch) with time predicted for the five models examined in Case 2. For reference, both the gap evolution for Case 1(b) and gap evolution measured during the experiment using LVDTs have been added to the plot. As can be seen in Figure 5.9, the model results are highly sensitive to how the constitutive behaviour of A319 and the bonded silica sand are defined. Case 2(a) and 2(b) predict no gap formation at the interface. This is because the casting is too deformable at elevated temperatures and is unable to exert enough force at the pinch point to push the chill upward. In Case 2(c), the mechanical properties of A319 are held constant for temperatures above 400 °C – i.e. no further reduction in the elastic modulus or yield point is defined above 400 °C. With the increased resistance to deformation at elevated temperatures, the casting is strong enough to exert sufficient force at the pinch point to displace the chill upward, forming the gap. In Cases 2(d) and 2(e), the elastic modulus of bonded sand is reduced by an order of magnitude relative to (b) and (c) to add the effect of softening of the bonded sand. As can be seen, this results in a larger gap as the chill is less constrained and is forced upward to a greater extent. These results indicate that the gap is highly sensitive to the competing forces that develop at the pinch point (forcing the chill upward) and the contact interface between the top of the chill and the bonded sand cap (forcing the chill downward).

To further explore these competing forces, the evolution of pressure with time has been output from the model at two locations: 1) at the casting-chill interface at the pinch point (Figure 5.10); and 2) at the interface between the mould cap and the chill at the line of symmetry (Figure 5.11). Both plots show the evolution in contact pressure (Pa) that is exerted by the chill with time (s) for Cases 2(a) through (e) and for Case 1(b) for reference.

The results for Case 1(b) (elastic moduli for A319 and sand held constant at the room temperature values) presented in Figure 5.10, show an initial rapid increase in the contact pressure at the casting chill interface, which then moderates with increasing time, reaching a peak value of ~350 MPa at around 200 s. For Case 2(a), in which a temperature dependent elastic modulus for A319 has been implemented, the contact pressure that develops at the pinch point is significantly lower, reaching a peak value of ~125 MPa at 200 s. The difference observed is consistent with the A319 being less stiff at elevated temperatures in Case 2(a). Cases 2(b) through 2(e) show the results for the temperature dependent, elastic-perfectly plastic constitutive behaviour for A319. As can be seen from the plots, the pressure at the pinch point increases and then saturates quickly at ~15-20 MPa and does not increase further with time, consistent with yielding. Note: the lowest yield stress input to the model is 20 MPa.

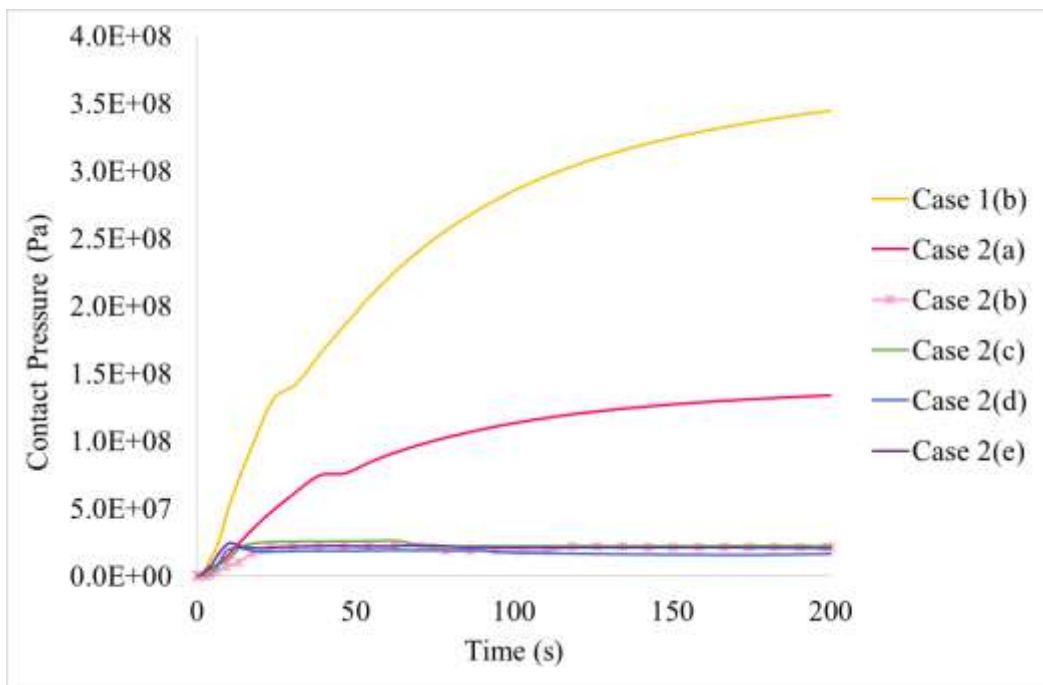


Figure 5.10: The evolution of contact pressure at the pinch point in the casting-chill interface

The results presented in Figure 5.11 show a steep initial rise in the chill-mould cap interface pressure for the first 10 seconds in Cases 1(b), and 2(a) through 2(c), in which the elastic modulus of the bonded sand was constant at 3.4 GPa. The pressure then continues to increase at a slower rate to the end of the analysis. This pressure acts as a resisting pressure to the pressure exerted on the chill by the casting at the pinch point. This resisting pressure restricts the motion of the chill in Y-direction and helps to maintain contact between the casting and the chill. The trend in these results shows the development of higher contact pressures at the mould cap-chill interface consistent with A319 having a higher stiffness. In Cases 2(d) and 2(e), in which the elastic modulus of the bonded sand was decreased to 0.34 GPa, a significant reduction in the chill-mould cap contact pressure was observed. Although the sand mould can still limit the upward movement of the chill, referring to Figure 5.9, the resistance is not high enough to predict a gap that is consistent with what was measured during the experiments.

According to the results presented in this section, it can be concluded that the mechanical behaviour of A319 and the bonded sand have a significant effect on the behaviour of the interface predicted by the preliminary model. Therefore, defining appropriate constitutive behaviour for these two materials in the final model is critical.

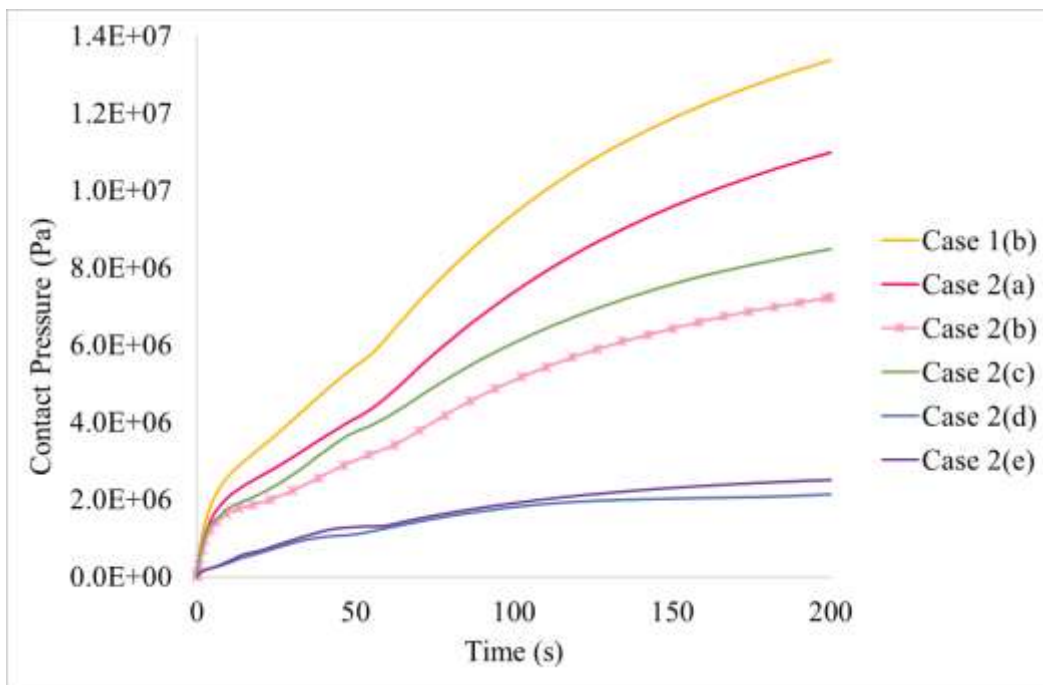


Figure 5.11: The evolution of contact pressure at the mould cap-chill interface

Case3 - The Effect of Heat Transfer at the Mould Boundaries

In Case 3, the effect of heat transfer to the sand mould boundaries was investigated. The heat transfer coefficients at all the sand mould boundaries were defined as gap dependent functions. The same surface-to-surface hard contact boundary with the displacement dependent heat transfer coefficient that is presented in Figure 5.5 was defined at the casting-chill interface.

The boundaries that represent an external surface exposed to air have the form:

$$-k \frac{\partial T}{\partial n} = h(T_{Surface} - T_{Ambient}) \quad \text{Equation 5.16}$$

where $T_{Surface}$ (K) is the temperature of the mould external surface, $T_{Ambient}$ (K) is the ambient temperature and h ($W \cdot m^{-2} \cdot K^{-1}$) is the heat transfer coefficient. This boundary condition was assigned to the exterior of the sand to describe natural convection with a constant heat transfer coefficient of 20 ($W \cdot m^{-2} \cdot K^{-1}$) and constant ambient temperature of 20 °C.

One consequence of adding the mould geometry to the analysis domain was that the execution times were increased by a factor of 16 in comparison to the models run in Cases 1 and 2. In order to reduce the computational time of the Case 3 models, the effect of relaxing the temperature and displacement residuals on the execution time, temperature results, and displacement results were assessed (these residual are used to assess convergence within a time step in ABAQUS). Both the temperature and displacement residuals were relaxed by 3 orders of magnitude. The results indicated no impact on the thermal and displacement results, however, the execution time was reduced by a factor of 8.

As can be seen in Figure 5.12, the deformation results for Cases 1(b) and Case 2(c) – (e) are affected when heat transfer to the mould is switched on. This is believed to be due to the thermal stresses that develop on the vertical wall of the casting bounding the sand mould. Contraction of the A319 along this wall results in the pinch point being partially unloaded, causing a reduction in the gap evolution with time.

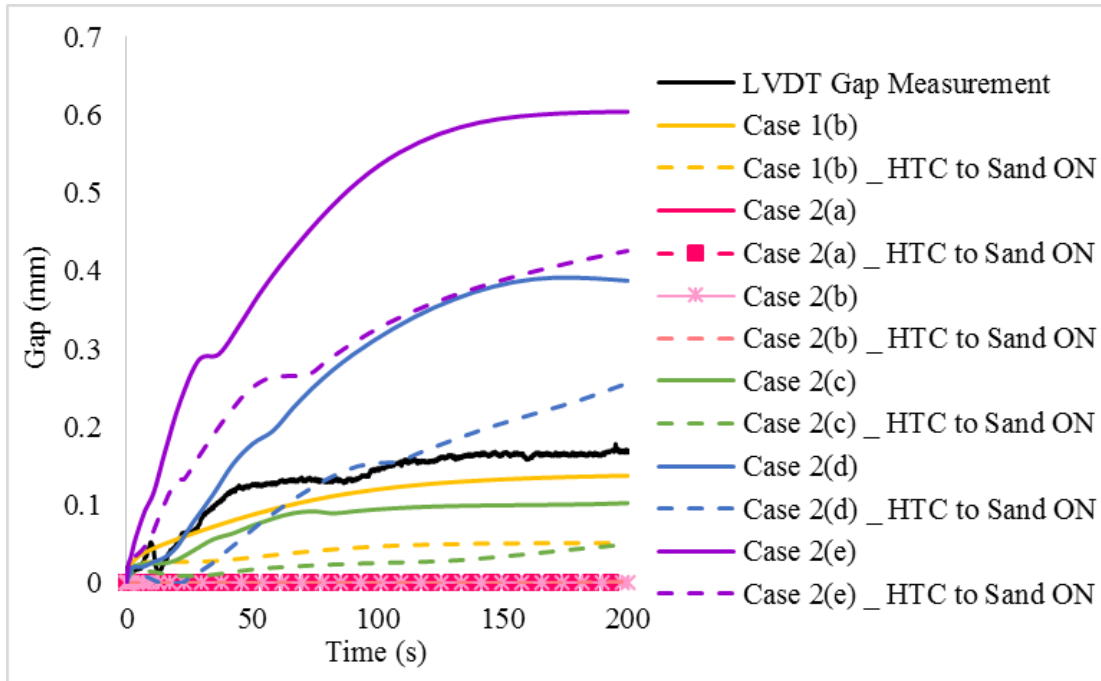


Figure 5.12: Comparison between interface gap behaviours obtained from experiment, and the sensitivity models

5.3. Three-Dimensional Model Development

To attempt to take some features of the geometrical complexity of the experimental casting into account a three-dimensional model was developed. The analysis has been limited to 150 s at which time the farthest thermocouple from the chill in the bulkhead area solidifies. The following sections describe the steps taken to formulate the 3-D model:

5.3.1. Three-Dimensional Model Domain

The geometries of the engine block section, the chill, and the mould were created in CATIA¹ and imported to ABAQUS CAE. Figure 5.13 shows the model domain for the three-dimensional analysis. To reduce the computational size of the problem, the following three major assumptions were made:

1. The model domain was based on the geometry of the mould package that was fabricated in Highland foundry, which is a simpler geometry than the GM mould package.

¹ CATIA is the trademark for Dassault Systèmes.

2. The geometries of the gating system, the riser, and the sand mould around the casting were not included in the analysis domain.
3. The three-dimensional analysis domain was assumed to be symmetric about the two vertical planes (XY and YZ) bisecting the casting, and hence, only one fourth of the geometry was included in the analysis.

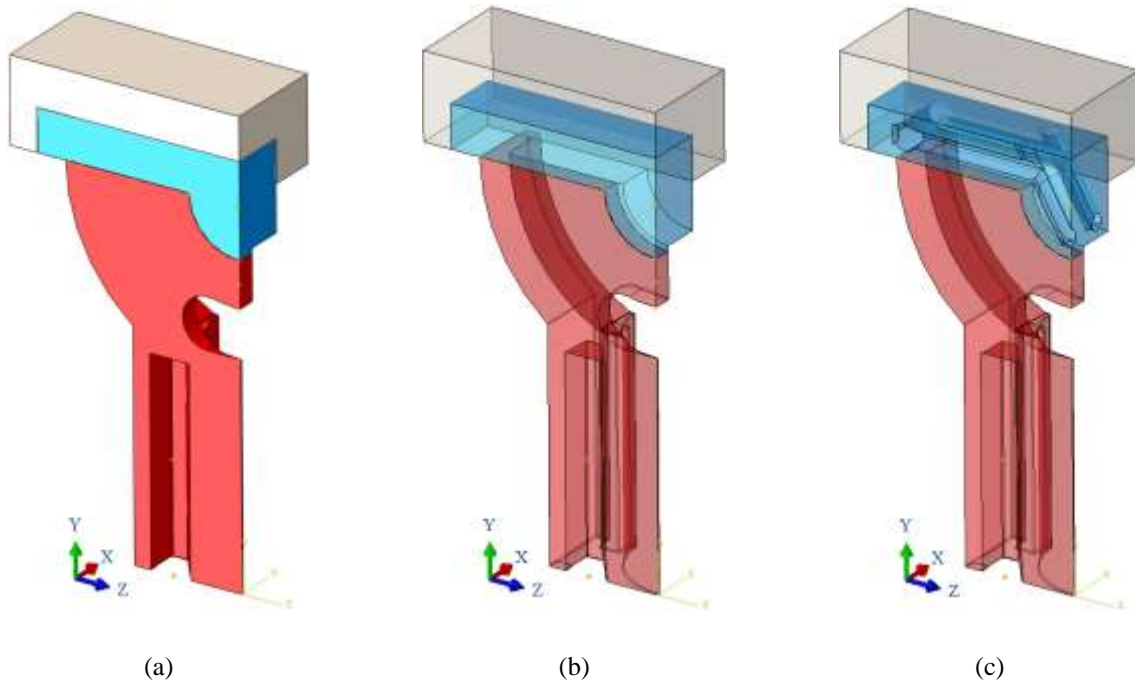


Figure 5.13: The three-dimensional model domain with a) solid view of the solid chill model assembly, b) transparent view of the solid chill model assembly, and c) transparent view of the water-cooled chill model assembly

5.3.2. Initial Conditions

As was mentioned earlier in this Chapter, the model is a fully coupled thermal-stress model that does not include the pouring process and fluid flow. Therefore, the thermal-stress simulation in the casting process begins when the mould cavity is full of molten metal, and an initial condition of the form shown in Equation 5.17 is applied to the casting domain:

$$T = T_0(x, y, z) \text{ in the domain, } t = 0s \quad \text{Equation 5.17}$$

The data collected from the thermocouples located in the mould cavity in each experiment indicated a non-uniform temperature distribution in the liquid metal at the end of the pouring processes, which was not unexpected as the metal enters the mould cavity through the bottom and

loses heat as it rises within the mould (see Figure 6.3, 6.10, and 6.18 in Chapter 6). The initial temperature distribution in each casting was assumed to be non-uniform (hence depends on x, y, and z) and was estimated from the thermocouple data recorded at various locations in the mould cavity for each experiment.

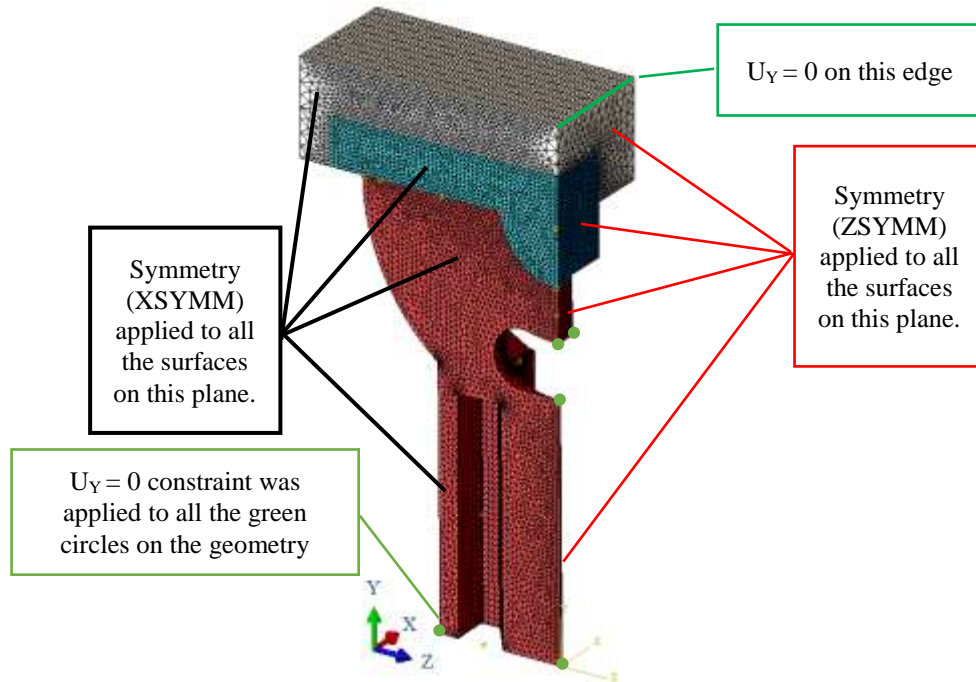
The initial temperatures in the two chills and the sand were taken from the thermocouple readings that were recorded during the experiments and were assumed to be uniform in the three domains. These initial temperatures are reported in Table 5.5.

Table 5.5: Initial conditions applied to the chills and the sand mould cap

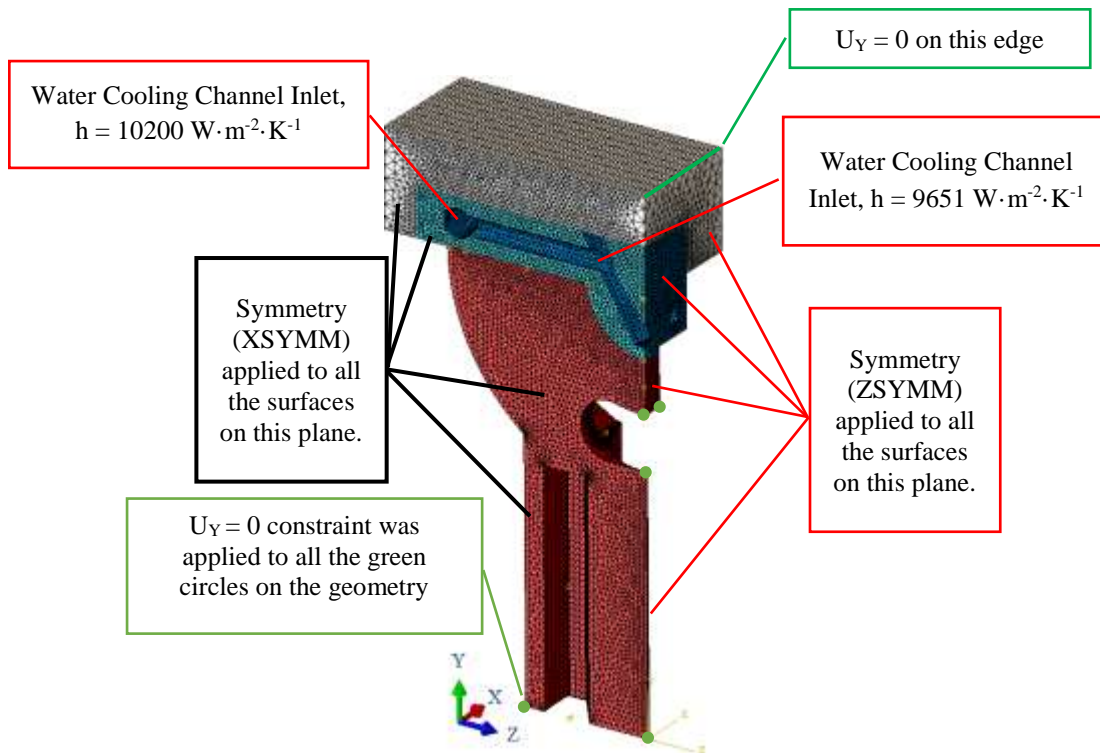
The Domain	Water-cooled Chill	Solid Chill	Sand Mould Cap
Temperature (°C)	20	25	20

5.3.3. Boundary Conditions

The meshed domain comprising the casting, the chill, and the mould together with the boundary conditions that were applied to the various boundaries are shown in Figure 5.14. Figure 5.14 (a) shows the solid chill casting model domain and Figure 5.14 (b) shows the water-cooled chill casting domain. The casting and the chill, extracted from the sand mould are shown in Figure 5.15, together with the boundaries identified by the boundary type – e.g. heat transfer coefficient (HTC) or adiabatic (symmetry). The expression used to describe the exchange of heat between the two boundaries in contact was introduced earlier in Equation 5.15.



(a)



(b)

Figure 5.14: The meshed model domain with mechanical and water cooling boundary conditions: (a) solid chill and (b) water-cooled chill

During the first stage of the development of the 3-D model, the same thermal boundary conditions and mechanical constraints that were implemented into the 2-D model in Case 1(b) were used. The heat transfer coefficients at the casting-chill and casting-mould boundaries were originally formulated as gap dependent functions and the chill-mould boundaries as temperature dependent functions. As was discussed earlier in section 5.2.6, the presence of the sand mould around the casting increased the execution time of the 2-D model by 16 times. A significant increase in execution time was also observed in the 3-D model, such that the model took 24 hours of execution time to complete 0.01 s of simulation. Numerous attempts were made to reduce the computational time, such as relaxing the heat flux and displacement residuals. However, none of these attempts proved to be successful, so it was decided to remove the mould geometry in order to make the problem computationally tractable. To address heat loss from the casting to the mould boundary, a time dependent heat transfer coefficient (film coefficient) was defined for the casting-mould boundaries, and the sand mould thermocouple data was used to specify an effective time dependent “ambient temperature” around the casting. Details of the approach used are described below.

This simplification is justified by the fact that solidification in the main bearing bulkhead (the area of focus) is dominated by heat transport to the chill. This is because the sand mould has a low thermal conductivity and acts to a certain degree as an insulating material, whereas the H13 is a relatively good heat conductor.

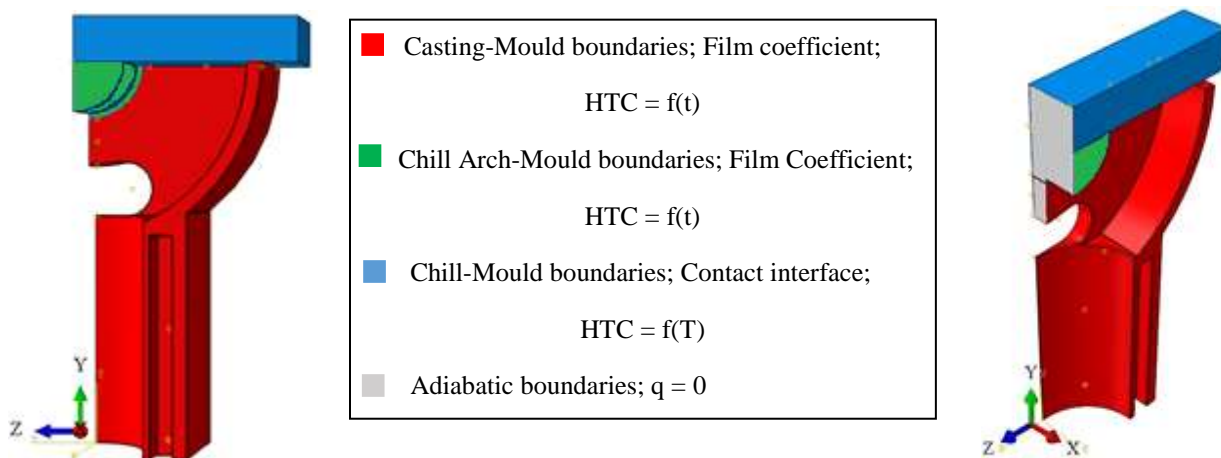


Figure 5.15: Boundary conditions at the casting-mould and the chill-mould interfaces (the same for the two chill)

Casting-Chill Interfacial Heat Transfer Coefficient

The casting-chill boundary can be subdivided into two areas: 1) the arch; and 2) the flat area, as shown in Figure 5.16. To consider the effect of temperature, gap, and pressure at the interface on the IHTC, a series of GAPCON subroutines with temperature, pressure, and gap dependent IHTC were developed and implemented in the model. Despite considerable effort, attempts to develop a comprehensive approach that considers all three dependencies were not successful and the model failed to converge since the heat flux residuals in the arch section of the interface were not achieved within the specified tolerance. This is believed to be due to the evolution of different gap and pressure regions on the same surface, which causes severe discontinuities in the IHTC, as the software transitions from one correlation to another – i.e. from a displacement based correlation to a pressure based correlation. Hence, the casting-chill interfacial heat transfer coefficient was defined only as a function of interfacial gap. Defining the casting-chill interfacial heat transfer coefficient as a function of gap, pressure, and temperature is an area for future work, beyond the scope of this thesis.

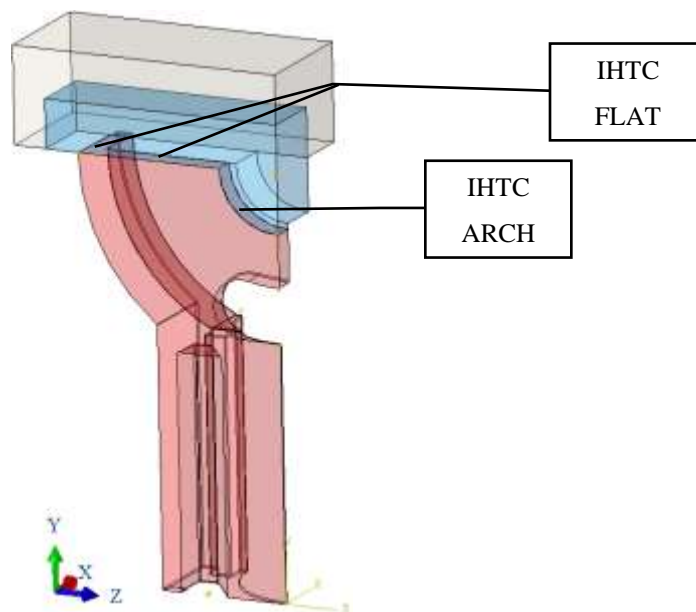


Figure 5.16: The schematic of the casting-chill interfaces with the applied boundary conditions (the same for the two chill configurations)

Figure 5.17 shows the gap dependent IHTC applied to the two casting-chill interfaces in the solid chill, the water-cooled chill, and the delayed water-cooled chill models. This was obtained by a trial-and-error fitting of the model results to a combination of the thermocouple and the LVDT

data obtained during the experiments (experimental results are presented in Chapter 6). The results show an approximately linear variation in IHTC with change in gap size over the range shown in Figure 5.17. The results are inconsistent with a resistance based on conduction through air, which suggests the presence of other gasses (e.g. binder vapour and/or water vapour) in the gap in addition to air.

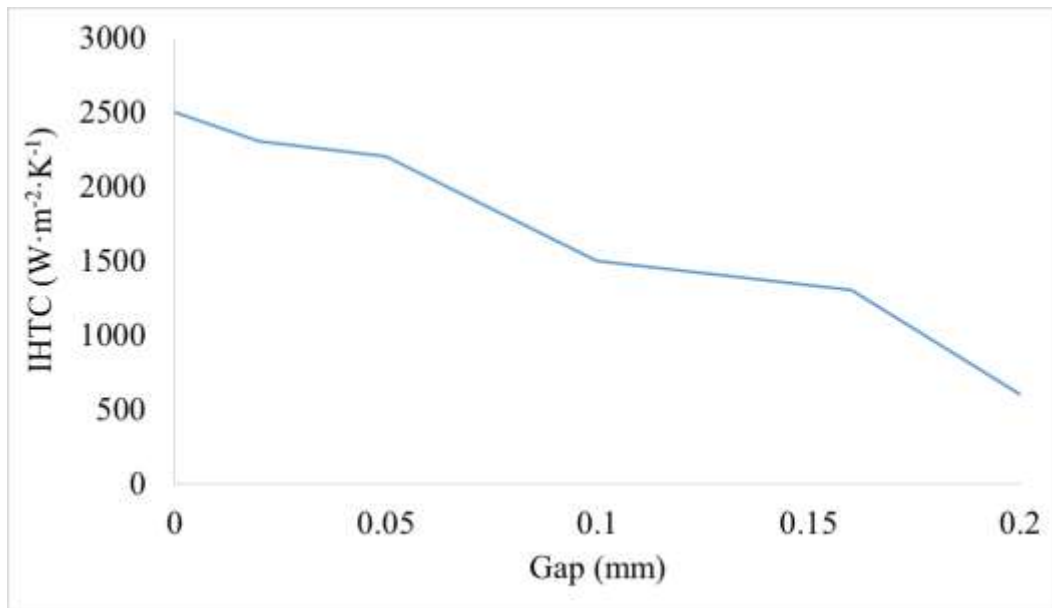


Figure 5.17: Variation of the casting-chill IHTC with gap size implemented to the models

The behaviour shown in Figure 5.17 may be rationalized as follows:

- When the liquid metal is first poured into the mould cavity, good physical contact between the casting and the chill is established. The molten metal fills at least a portion of the small asperities present on the chill surface due to its high fluidity, and hence; the IHTC is initially high ($2500 \text{ W}\cdot\text{m}^{-2}\cdot\text{K}^{-1}$).
- As the casting begins to solidify, two scenarios may happen:
 - 1) A gap forms as the cast metal undergoes solidification shrinkage and thermal contraction. This results in a drop in IHTC as a function of gap size.
 - 2) No gap forms and the IHTC remains at the initial high value of $2500 \text{ W}\cdot\text{m}^{-2}\cdot\text{K}^{-1}$.

Note that the gap in ABAQUS is predicted as a result of solution of the global (macro-scale) equilibrium equations, and therefore, phenomena occurring in the early stages of solidification

with respect to the degradation of interface contact are not captured in this displacement dependent function.

Casting-Mould Heat Transfer Boundary Conditions

As was discussed earlier in this Section, the mould geometry was removed from the three analyses in order to reduce the computational time, and instead, a film condition interaction (convection boundary condition) was defined at the casting-mould boundaries – see Equation 5.16.

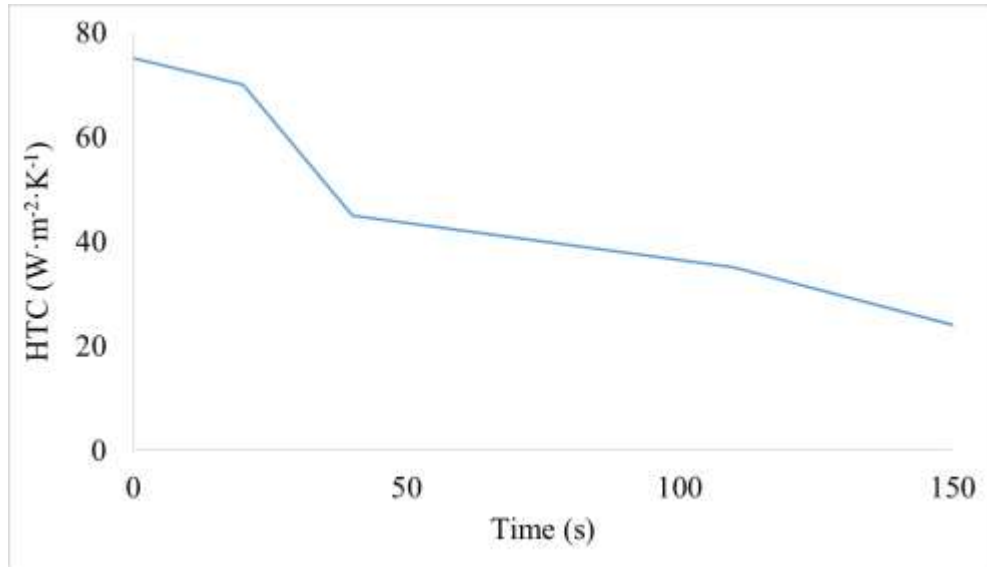


Figure 5.18: Casting-mould heat transfer coefficient implemented to the models

The film condition interaction was implemented with a combination of a time dependent heat transfer coefficient, shown in Figure 5.18, and a time dependent effective far-field, or ambient temperature, as shown in Figure 5.19. The average of the sand core thermocouple data was used to define the time dependent effective ambient temperature evolution. Note: the same ambient temperature behaviour for the barrel core and the side core were applied to the three models since the temperature differences between the three cases were negligible – see Figure 5.19.

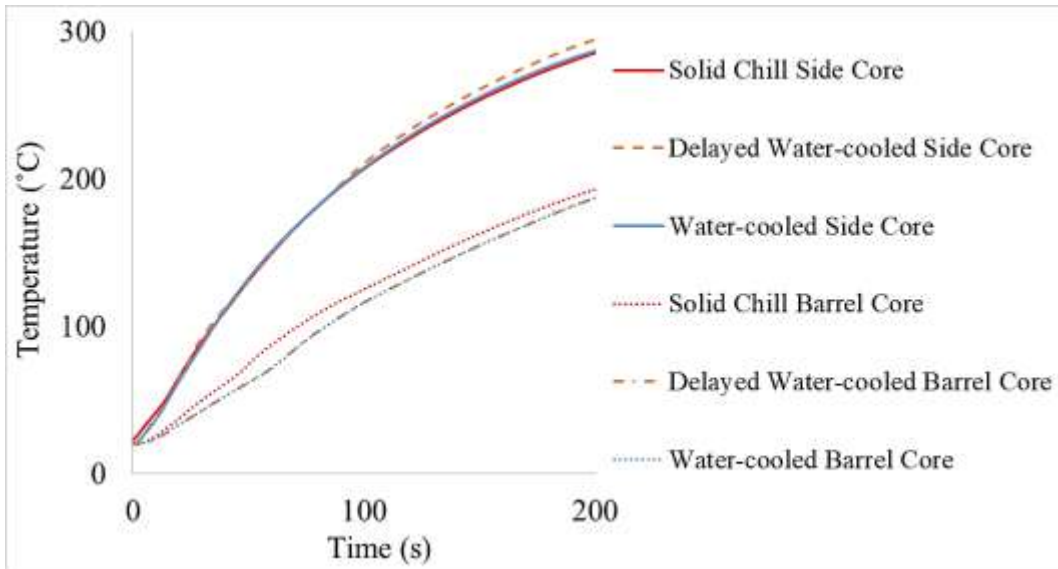


Figure 5.19: Thermocouple readings obtained from the side and barrel cores in the three castings

Chill-Mould Heat Transfer Boundary Conditions

The chill-mould interfaces including the chill-mould cap interfaces and the chill arch-mould interfaces are shown in Figure 5.20.

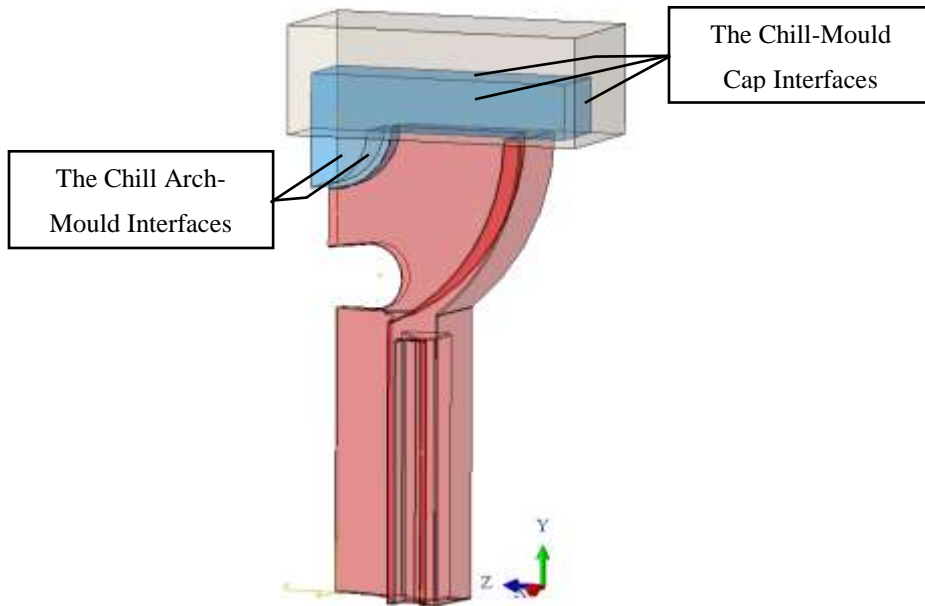


Figure 5.20: The schematic of the chill-mould interfaces (the same for the two chill configurations)

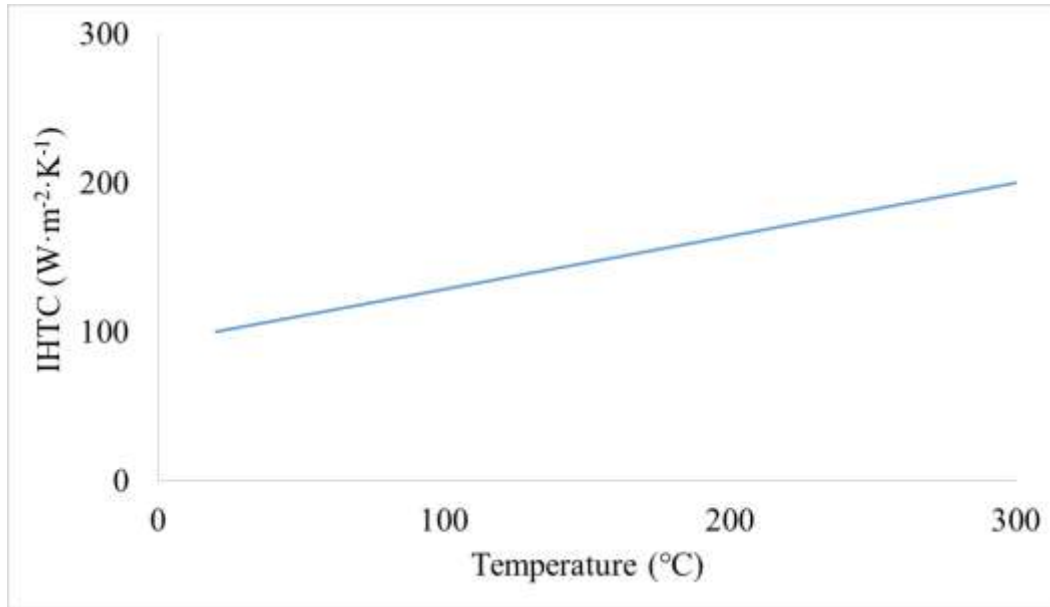


Figure 5.21: Temperature dependent heat transfer coefficient at the chill-mould cap boundaries

Two different interface behaviours were implemented for the chill-mould interfaces: one for the chill-mould cap interface; and the other for the chill arch-mould interface:

Chill-mould cap interface - Owing to the presence of the sand cap in the analysis, which is critical from the standpoint of constraining the upward motion of the chill, the chill-mould cap interface was defined as a surface-to-surface contact boundary condition in ABAQUS. This allows for a range of dependencies to be defined including temperature, gap and contact pressure. To avoid adding additional challenges with respect to convergence, a temperature dependent IHTC formulation was adopted at this interface. The IHTC used in the analysis is shown in Figure 5.21 and was assumed to be linearly dependent on the chill temperature. This behaviour was intended to capture better contact (increased heat transfer) between the chill and the sand mould cap as the chill heats up and expands.

Chill arch-mould interface – In the case of the arch-mould interface, the sand mould has been removed in order to reduce the model execution time, as previously discussed. Thus, a film condition interaction was defined for this boundary. In ABAQUS, this type of boundary only allows for a time-dependent (or constant) heat transfer coefficient to be defined – see Equation 5.16 (the option to define a temperature dependent film coefficient in a user-defined subroutine was not explored at this time). Two time-dependent relationships were defined – one for the solid

chill, and the other for the water-cooled chill – see Figure 5.22. In the case of the solid chill, the temperature of the chill increases at a different rate and to a higher temperature in comparison to the water-cooled chill. To capture the effect of this difference on interfacial heat transfer, the two different behaviours shown in Figure 5.22 were adopted. In terms of the ambient or far-field temperature needed to complete the definition of this boundary condition, the same time-dependent temperature that was used for the casting-mould interfaces were used for chill arch-mould interfaces – see Figure 5.19.

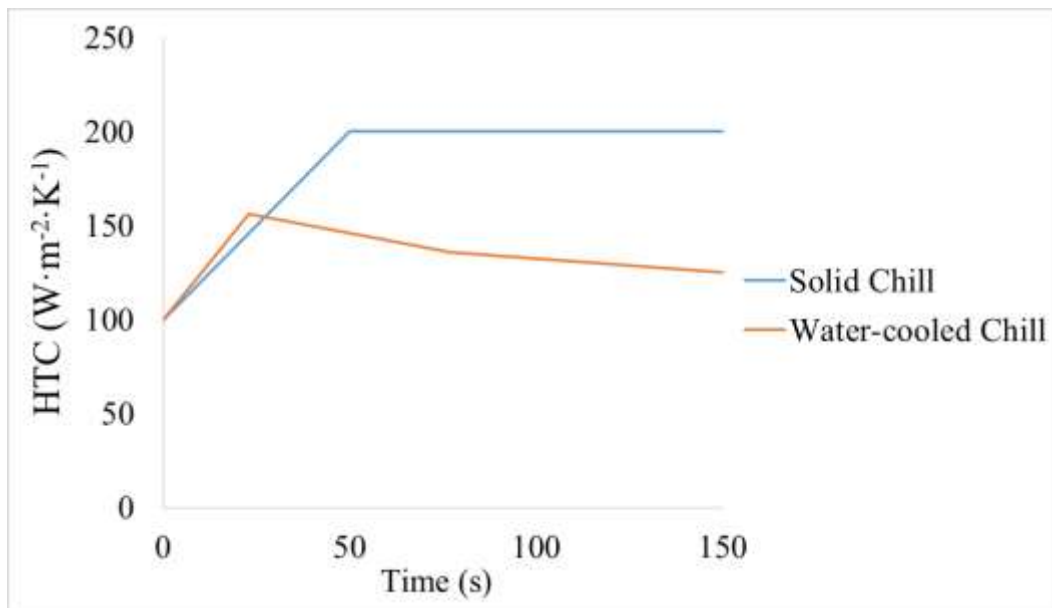


Figure 5.22: Time dependent heat transfer coefficient at the chill arch-mould interfaces

Note that in both cases, the range of the heat transfer coefficient is approximately the same for a given chill type.

Heat Transfer Boundary Conditions Applied to the Exterior of the Sand Mould Cap

The boundaries that represent an external surface of the cap exposed to the air have been previously introduced in Equation 5.16. Natural convection was assigned to the exterior of the sand mould, with a constant heat transfer coefficient of $20 \text{ (W}\cdot\text{m}^{-2}\cdot\text{K}^{-1}\text{)}$ and constant ambient temperature of 15°C .

Water Cooling Channel Boundary Conditions

The heat transfer in the water cooling channels may be expressed as:

$$-k \frac{\partial T}{\partial n} = h(T_{Surface} - T_{Water}) \quad \text{Equation 5.18}$$

where $T_{Surface}$ (K) is the temperature of the surface of the cooling channel, which is in contact with water, and T_{Water} (K) is the water temperature. As the diameters of the cross water cooling channels (inlet and outlet) are different from the diameters of the three cooling channels across the chill, the heat transfer coefficients applied to them need to be calculated separately. The heat transfer coefficient in the water inlet/outlet may be determined by taking the following steps:

Step 1 – Calculating the velocity of the coolant in the cooling channel:

$$V = \frac{Q}{A} = \frac{6 \times 10^{-4}}{2 \times 10^{-4}} = 3(m \cdot s^{-1}) \quad \text{Equation 5.19}$$

where V ($m \cdot s^{-1}$) is the velocity of water in the cooling channel, Q ($m^3 \cdot s^{-1}$) is the flow rate that was measured by the in-line flow meter, and A (m^2) is the area of the normal cross-section of the cooling channel.

Step 2 – Determine if the flow in the pipe is a laminar flow or a turbulent flow by calculating the Reynolds number:

$$Re = \frac{\rho V D}{\mu} = \frac{1000 \times 3 \times 0.015}{0.001} = 4.5 \times 10^3 \quad \text{Equation 5.20}$$

where Re is the Reynold's number, ρ ($kg \cdot m^{-3}$) is the density of water at 10 °C, D (m) is the diameter of the cooling channel, and μ ($Pa \cdot s$) is the viscosity of water at 10 °C. The laminar to turbulent transition in a pipe occurs when the Re exceeds 4000. Since the value obtained from Equation 5.20 exceeds this limit, the water flow in the pipe is considered to be turbulent flow.

Step 3 – Given that the criterion for a turbulent flow is exceeded, the Nusselt number can be calculated from the following correlation:

$$Nu = 0.023 \times Re^{0.8} \times Pr^n \approx 3 \times 10^2 \quad \text{Equation 5.21}$$

where Pr is the Prandtl number:

$$Pr = \frac{\nu}{\alpha} = \frac{\text{MomentumDiffusivity}(m^2 \cdot s)}{\text{ThermalDiffusivity}(m^2 \cdot s)} = 9.47 \text{ for water at } 10^\circ\text{C} \quad \text{Equation 5.22}$$

and n is 0.4 when the walls are hotter than the bulk fluid and 0.33 when the walls are colder. The heat transfer coefficient was obtained from:

$$h = \frac{k_{\text{water}}}{D} \times Nu = \frac{0.51}{0.015} \times 3 \times 10^2 \approx 10200 (W \cdot m^{-2} \cdot K^{-1}) \quad \text{Equation 5.23}$$

where k_{water} ($W \cdot m^{-1} \cdot K^{-1}$) is the thermal conductivity of water at 10°C .

The same series of calculations were done to determine the heat transfer coefficient in the three cooling channels with 10 mm diameter and a value of 9651 ($W \cdot m^{-2} \cdot K^{-1}$) was obtained and used in the model. This calculation assumed that the water flow rate in each of the channels was identical and $\frac{1}{3}$ of the flow rate in the inlet channel.

Symmetry Mechanical and Heat Transfer Boundary Conditions

The two symmetry boundary conditions applied to the model are of the forms:

$$XSYMM : U_x = UR_y = UR_z = 0 \quad \text{Equation 5.24}$$

$$ZSYMM : U_z = UR_x = UR_y = 0 \quad \text{Equation 5.25}$$

where U_x and U_z (m) are the displacements in x and z directions, respectively, and the UR_i are the rotational displacements around i axis. These symmetric surfaces are automatically defined as adiabatic surfaces in the heat transfer analysis:

$$q = 0 \quad \text{Equation 5.26}$$

where q ($W \cdot m^{-2}$) is the heat flux.

To avoid rigid body motion in the model, the following displacement boundary condition was applied to the lower corner of the casting at the intersection of the two symmetry planes (note this is to replace the constraint formerly applied to the sand mould at this location see Figure 5.14).

$$U_y = 0 \quad \text{Equation 5.27}$$

which suppresses the motion of the domain in the Y direction. Note: the motion and rotation of this point in and around X and Z directions are constrained by the symmetry boundary conditions that have been applied to the symmetric surfaces, otherwise defining an “Encastre” boundary condition ($U_Y = UR_X = UR_Y = UR_Z = 0$) for this point would have been necessary.

5.3.4. Material Properties

The thermo-physical and mechanical material properties of A319, H13 tool steel, and bonded silica sand were taken from the values reported in the literature, and are summarized in Table 5.2 and Table 5.3, respectively. All of these materials have been defined as being homogeneous and isotropic. The Poisson’s ratio is assumed to be 0.33 for all of the materials.

5.3.5. Solution Technique and Mesh

As with the 2-D problem, ABAQUS 2016 was used as a solver for the problem subject to initial and boundary conditions, which are defined in the previous sections of this Chapter. The 3-D model domain was meshed in ABAQUS CAE and the example mesh topographies in the domains are shown in Figure 5.14 for both the solid chill and the water cooled chill models. The mesh statistics are shown in Table 5.6.

Table 5.6: Mesh statistics

Domain	Element Type	Element Shape	Number of Nodes	Number of Elements
Casting	C3D4T ¹	Tetrahedral	25119	119201
Solid Chill			18164	94283
Water-cooled Chill			18804	93422
Mould Cap			18025	91091

The time step was set to be automatically chosen by ABAQUS, given fixed user-defined initial, minimum, and maximum values for the time step. This type of time step control allows ABAQUS to select time increments based on a user-defined maximum allowable temperature change per increment.

¹ Continuum 3-D, 4-node thermally coupled tetrahedron, linear displacement and temperature

6. Results and Discussion

6.1. Solid Chill Casting

Experimental Data - The casting thermocouple locations are shown in Figure 6.1, and the chill thermocouple locations are shown in Figure 6.2. Note: that the thermocouple locations for all the experiments with both the chill formats are the same, hence, are presented only once. In the graphs, the data from some of the thermocouples are not present. This is because some of the thermocouples failed during the experiments.

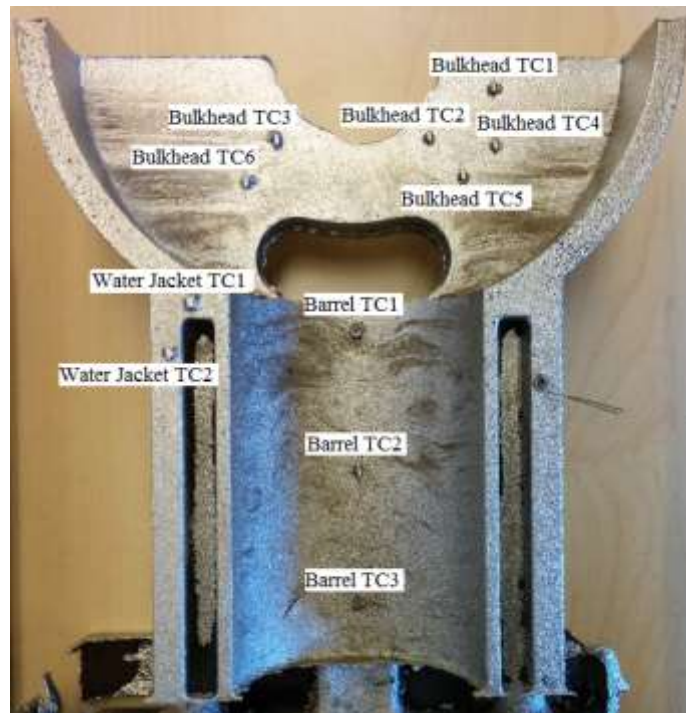


Figure 6.1: Thermocouple locations in the castings



Figure 6.2: Thermocouple locations in the chills

The thermal data obtained from the solid chill castings are presented in Figure 6.3 along with the solidus (T_s) and the liquidus (T_l) lines, which have been added to the plots to aid in identifying when solidification begins and when it is complete. The plot has been limited to the first 400 s, which encompasses the time taken for the casting to solidify. The interface TCs (the casting and the chill) are plotted as dashed lines (this scheme is used in the subsequent plots, too). The Bulkhead TCs 1 – 3, which are located 10 mm away from the chill, and the “Casting Interface TC” show an initial rapid drop in temperature for the first ~40 s. The rate of temperature drop then decreases until approximately 90 to 110 s at which point solidification at these locations finishes and a slight increase in the cooling rate appears. The “Bulkhead TC5”, which is located 30 mm away from the chill, also shows the same trend, as do the Barrel TCs and the Water Jacket TCs, which are farther away from the chill. The initial rapid drop is associated with the liquid metal contacting the cold mould and the reduction in the cooling rate within the solidification temperature range is associated with the release of latent heat. Finally, there is clearly a decrease in the cooling rate with increasing distance from the chill, as would be expected.

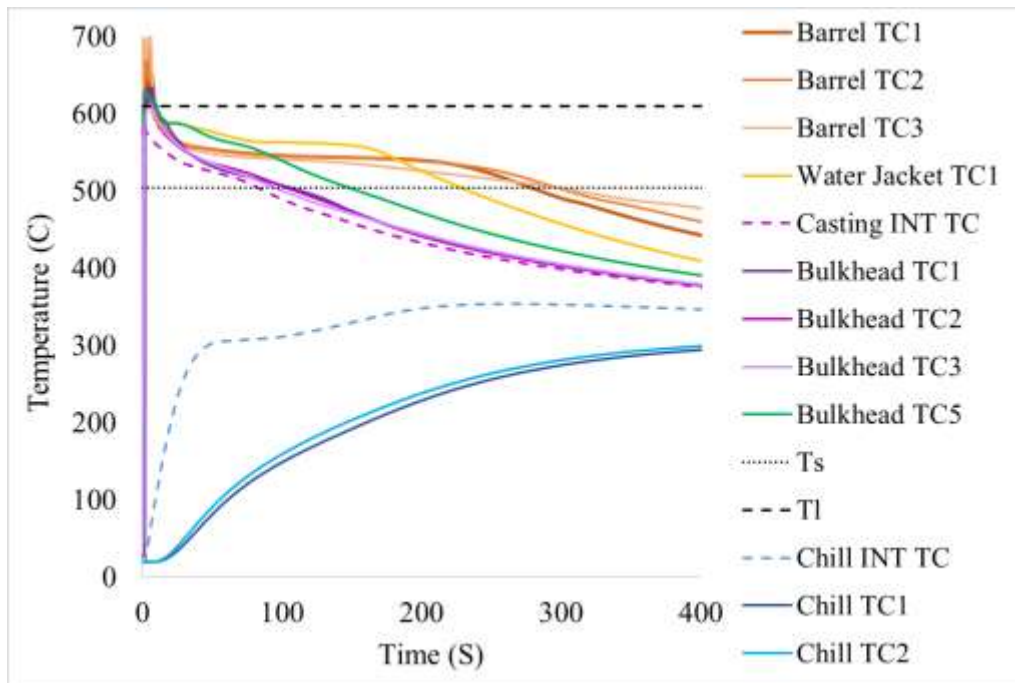


Figure 6.3: Temperature variation with time for various thermocouple locations within the casting and the solid chill

Turning to the chill thermocouples, there is an initial rapid increase in temperature at the chill interface, reflecting a high initial rate of heat transfer from the casting to the chill. The rate of temperature change in the chill at the interface then significantly decreases at approximately 50 s.

An inflection point in the chill temperature at the interface position can be observed at about ~100 s, which may reflect changes in the interface resistance associated with the gap dynamics. The “Chill TC1” and “TC2” show a more moderate temperature increase due to their position farther into the chill. The interface chill TC peaks at approximately 350 °C and then gradually decreases with time. The “Chill TC1” and “TC2” peak at close to 275 °C at a time slightly beyond the range shown in the figure.

Figure 6.4 shows the evolution of the casting-chill interfacial gap with time for the solid chill experiment, based on the relative displacements of the chill and the casting that were measured by the LVDTs. The gap size was determined by taking the following steps:

1. Both LVDT displacement measurements were set to the same reference point;
2. The noise produced by the signal conditioner was then removed from the raw data;
3. Finally, the gap size was calculated by taking the difference between the two displacements.

The gap, as measured at the bottom of the arch, starts to form and increase rapidly from the early stages of the casting process. It is observed to initially plateau at a value of 0.13 mm at approximately 50 s, before increasing again and reaching a peak of ~0.17 mm at around 150 s. The gap then remains roughly constant until 250 s at which point it begins to decrease. The development of the first plateau at around 50 s is consistent with the inflection point in the chill interface temperature behaviour and is consistent with an increase in the thermal resistance across the chill-casting interface as the gap grows.

At the first glance, the behaviour of the gap would appear to be driven by the contraction of the casting, as the expansion of the chill would have the opposite effect. The reason for the further increase in the gap following the first plateau and the reduction in the gap beyond 250 s is not obvious at this point.

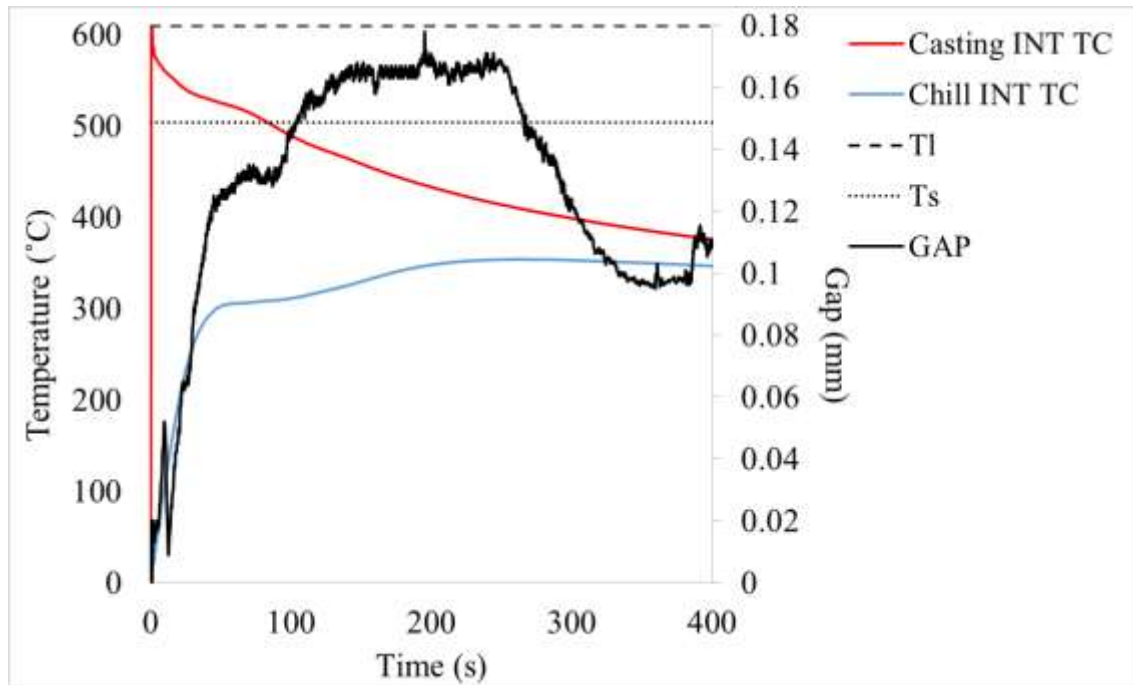


Figure 6.4: The evolution of the casting-chill interfacial gap with time in the solid chill experiment

Application of the 3-D Model to the Solid Chill Experiment – Based on the experimental data and the 2-D modelling results presented in Section 5.2.6, it is clear that the behaviour of the interface is complicated. Owing to the limitations of the 2-D model with respect to geometry, the 3-D model, described in Section 5.3, has been developed for the solid chill in an attempt to develop a complete picture of the interface behaviour. To begin with, the 3-D solid chill casting model is first verified with the thermal and displacement results from the solid chill experiment. The results of the 3-D model simulation are then combined with the experimental results to complete the analysis. Prior to comparing the model thermal predictions to the experimental data, the location of the thermocouple in the casting were confirmed with the actual final casting.

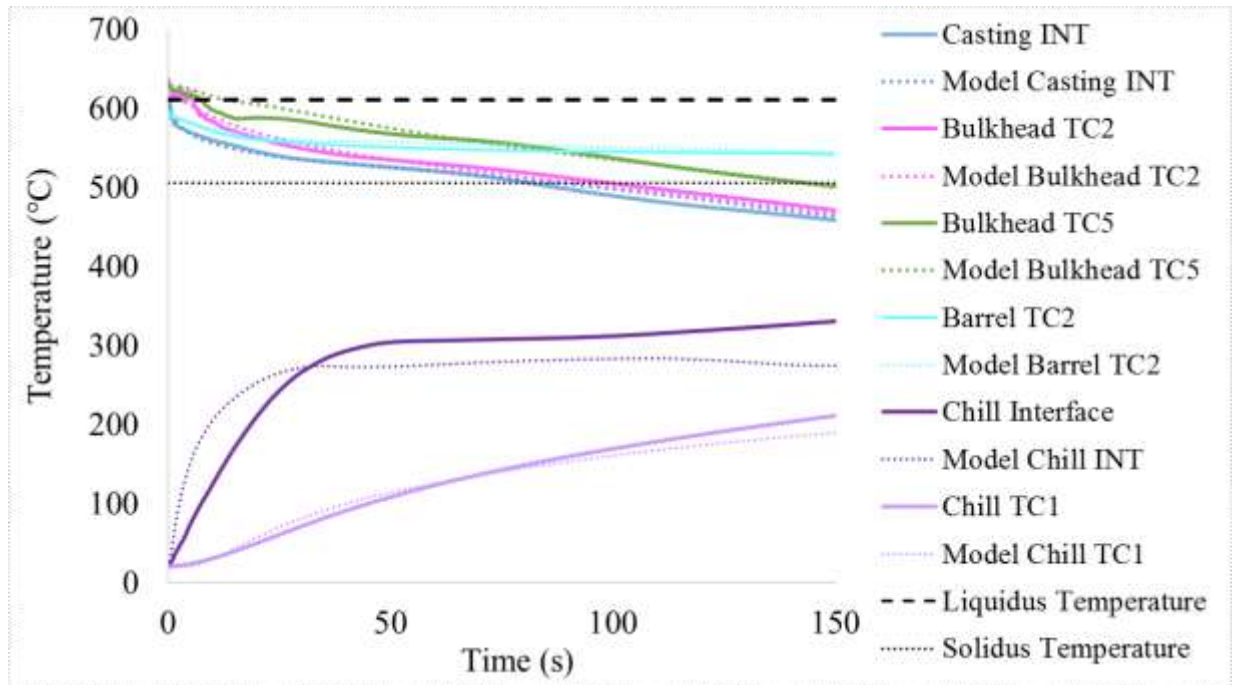


Figure 6.5: Comparison between the solid chill model temperature predictions and the TC data at different locations

Figure 6.5 shows a comparison between the model temperature predictions and the TC data at selected locations in the casting bulkhead, the casting barrel, and the chill. In the plot, the solid lines represent the experimental results, and the dotted lines show the model predictions. In addition, on each figure, the black horizontal lines have been added to delineate the liquidus and solidus temperatures for A319. Note: to reduce the overall computation time, the analysis was limited to 150 s and hence the plot compares the results up to 150 s (not 400 s used in plotting the TC data). This range in time is sufficient for the bulkhead thermocouples to reach to the solidus temperature.

Overall, as shown in Figure 6.5, the agreement between the model thermal results and the experimental thermocouple data is good given the complexity of the model. For the thermocouples located in the casting, the variation of temperature with distance from the chill and the evolution in cooling rate with time have been reproduced accurately. A similar agreement is also observed for the location of chill TC1. The largest error observed between the model predictions and the experimental temperature measurements is ~30% at the location of the chill interface thermocouple at 12 seconds, and ~4% at the location of the Bulkhead TC5 at 16 seconds. The reason for this

inconsistency at the chill interface is not clear, particularly in light of the good agreement at the location of chill TC1.

Figure 6.6 shows a comparison between the casting-chill interface gap predicted by the model and the LVDT measurements obtained during the experiments. Again, very good agreement between the model predictions and the LVDT gap measurements can be observed in the graph, with a maximum of ~ 0.04 mm difference between the model prediction and the experimental results at 150 s.

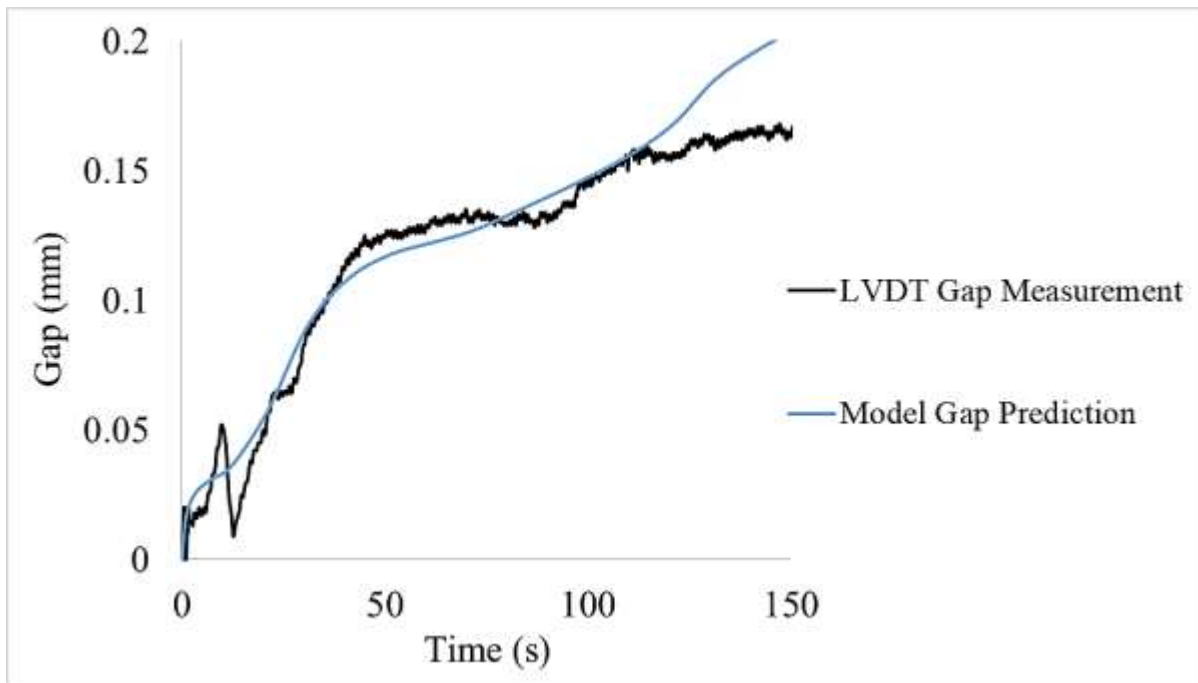


Figure 6.6: Comparison between the solid chill-casting interface gap size measurements with LVDTs and the model predictions

Taking a more macro-scale perspective, Figure 6.7 shows the evolution of the displacement of the casting, the chill, and the sand mould cap with time together with the temperature contours, predicted by the 3-D model, at 20, 50, 100 and 150 s. The displacements have been magnified by a factor of 10 to make the deformation more obvious to the eye. As can be seen in the series of images, the gap that forms at the bottom of the arch and the gap that forms along the horizontal section at the top of the bulkhead, both increase with increasing time up to the end of the simulation at 150 s. In contrast, there is no gap formed at the pinch point at the top of the arch. The contours of temperature show a gradual decrease in the casting temperature with time and a gradual increase

in the chill temperature with time as heat is transferred from the casting to the chill. As was discussed in Section 5.2.6, in addition to the pinch point stress, there is another contributor to the development of the gap at the casting-chill interface. As heat is transferred from the casting to the chill, the chill bends due to the development of thermal stresses resulting in augmentation of the gap along the horizontal portion of the interface.

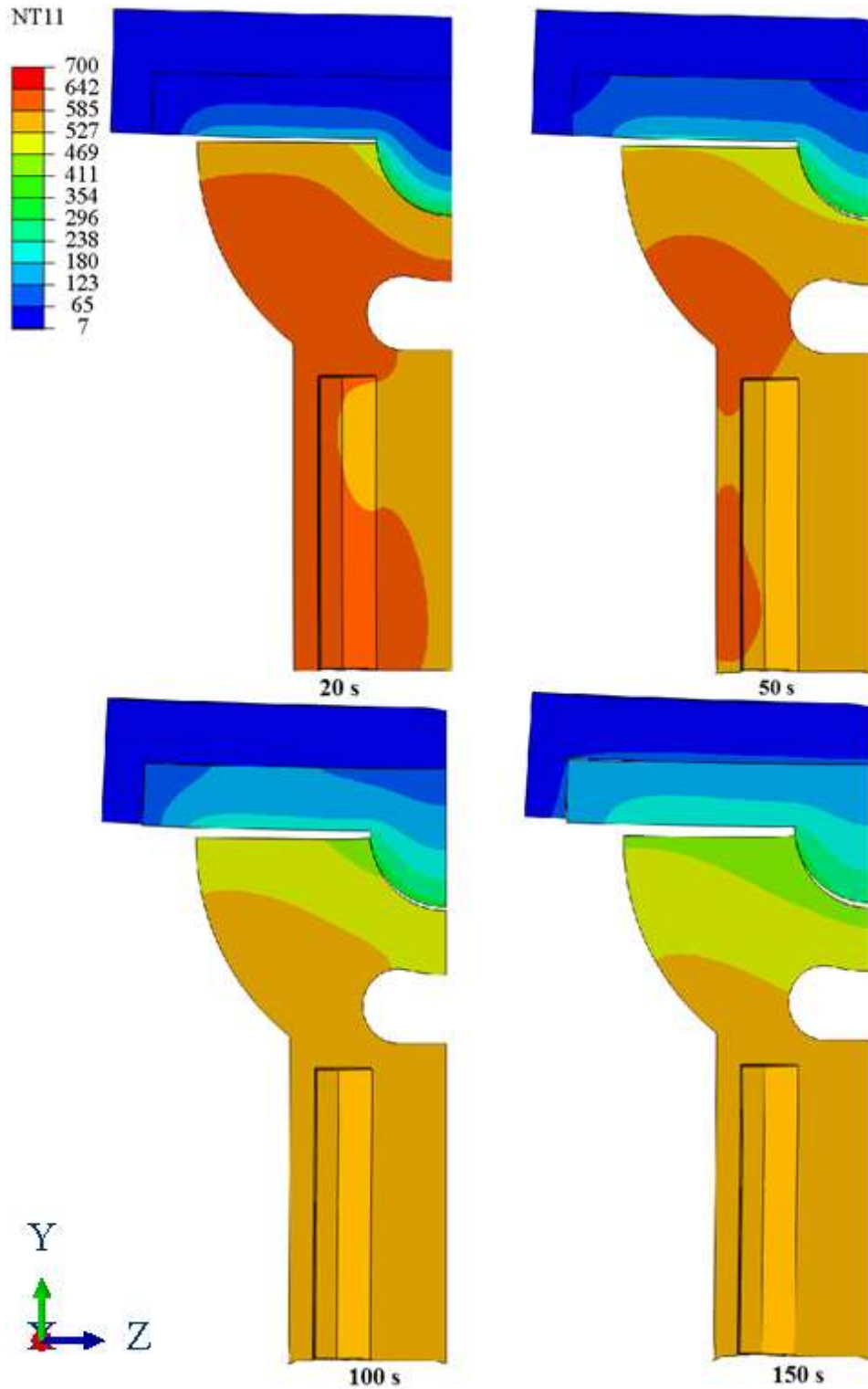


Figure 6.7: The evolution of the displacement in the casting, the chill, and the sand mould cap with time, and the temperature contours predicted by the solid chill model (The deformation is magnified by a factor of 10, and the temperature unit is in °C.)

Figure 6.8 shows a series of contour images illustrating the evolution of the contact pressure at the pinch point with time on the surface of the casting at 20, 50, 100 and 150 s. A pressure in the range of 20 to 45 MPa develops at the pinch point by 20 s. The contact area and peak pressure then gradually increase with time, reaching a maximum of approximately 60 MPa by 50 s at small locations within the contact area. To take a more quantitative look at the development of pressure at the pinch point/contact area, the evolution of contact pressure at the contact area with time has been plotted in Figure 6.9. The graph plots the average of the contact pressure over the contact area. The results show that the average contact pressure develops very fast at the pinch point/contact area within the first ~35 s and then continues to increase very slightly to a maximum of 27 MPa. This behaviour is consistent with the rate of gap growth shown earlier in Figure 6.6. Note that as both the contact area and pressures are increasing in Figure 6.8, the average results are different than the contour results.

Overall, the results in the two graphs show that the pressure developed at the pinch point location is responsible for the formation of the gap observed at the bottom of the arch and on the flat portion of the bulkhead (because of the curvature of the arch, the normal component of the pressure at the pinch point pushes the chill up creating a gap at the bottom of the arch and along the horizontal interface). This upward motion of the chill is constrained/moderated by the presence of the bonded sand cap. The thermal induced deformation of the chill appears to also contribute to the gap formation on the horizontal portion of the interface as the chill bends. This is consistent with what was observed experimentally; as previously described, when removing the chill from the casting after each experiment, a gap could be seen with the naked eye along the flat interfaces between the chill and the casting and at the bottom of the arch, in all the castings including the water-cooled experiments. In contrast, the chill was stuck to the casting on either side of the arch, requiring force to remove it.

Based on the evidence from the thermal data, the displacement data, and the 2-D and the 3-D model results, the casting-chill interface behaviour can be explained. During the first 35 seconds of the casting process, there is a sharp increase in the temperature of the chill and a high cooling rate in the areas in the casting that are close to the interface. This is due to the initial good physical contact between the casting and the chill, which results in a high heat transfer rate between the two parts. Within the first 35 s both the 2-D model and the 3-D model predicted that a pinch-

point develops at the sides of the arch that results in the chill being pushed up. This is believed to be responsible for the chill losing contact with the casting along the flat part of the bulkhead and in the middle of the arch at the bottom (the latter confirmed by the LVDT measurements). The formation of the physical gap results in an increase in the resistance to heat transfer across the interface and a moderation in the cooling rate of the casting in the bulkhead, and a moderation in the rate of temperature increase in the chill, which is observed in the thermocouple data. Thus, the behaviour of the interface heat transfer is complicated and largely dominated by the behaviour of the gap. The behaviour of the gap, in turn, is dependent on a number of factors including the solidification shrinkage and the thermal contraction and deformation of the casting, the thermal expansion and deformation of the chill, the geometry of the interface between the casting and the chill, and the constraining influence of the sand mould cap.

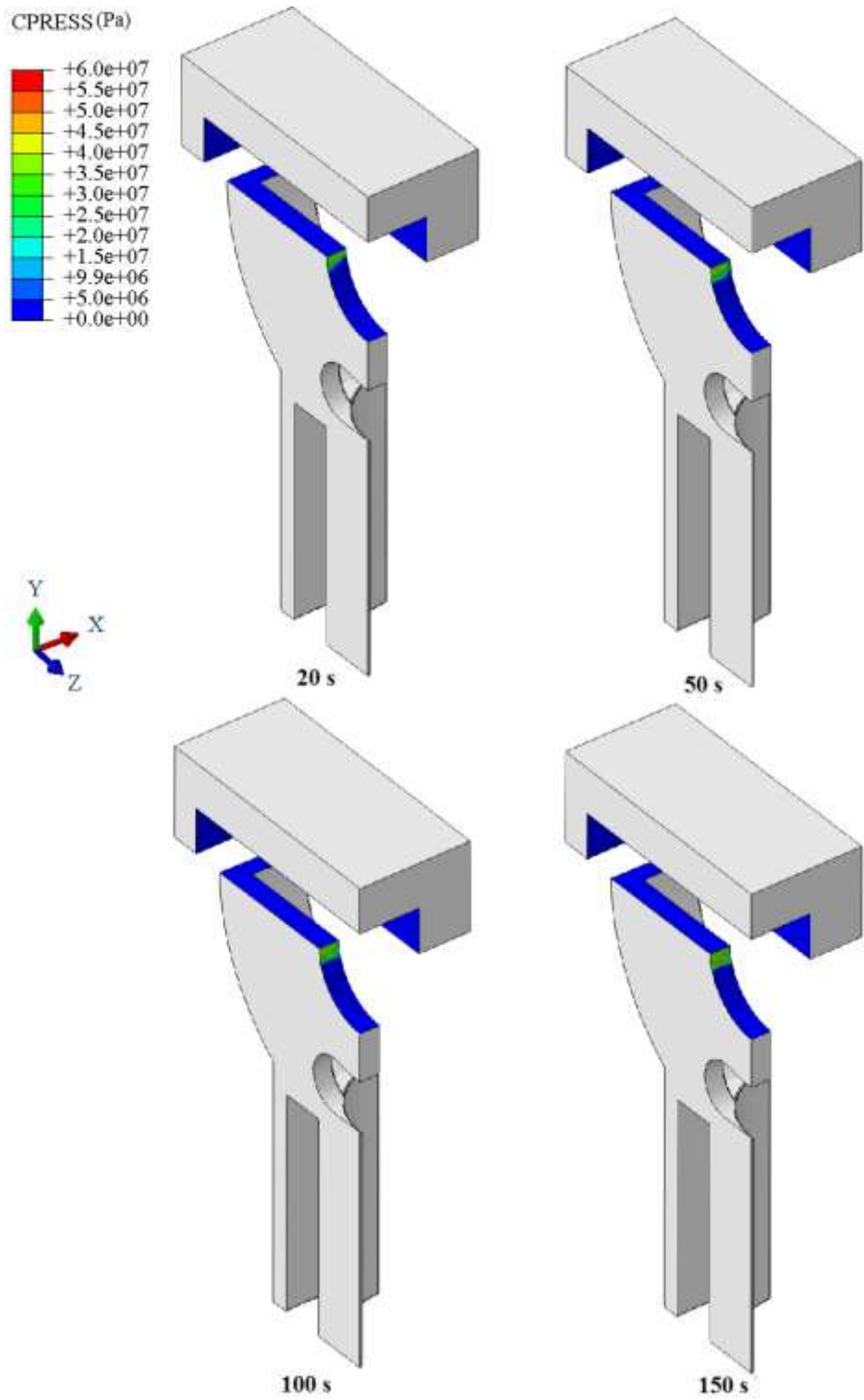


Figure 6.8: The evolution of the contact pressure at the pinch point predicted by the solid chill model (The pressure unit is in Pa.)

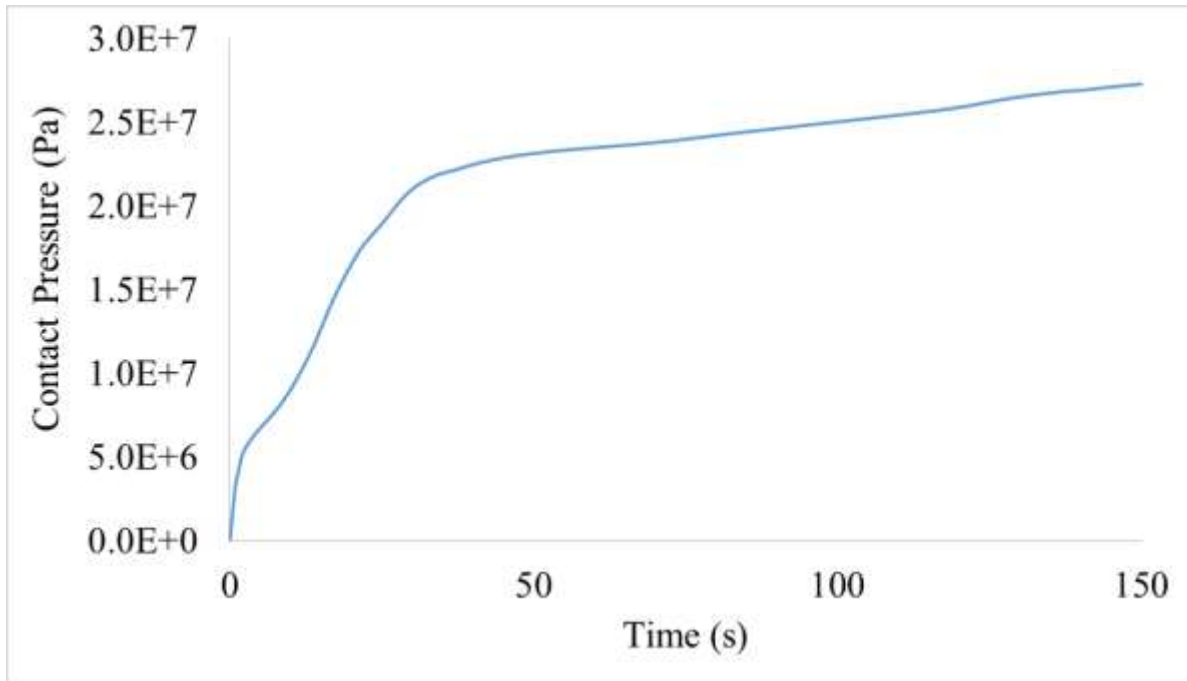


Figure 6.9: The evolution of the contact pressure at the pinch point/contact area (the value is the average of the contact pressure on the contact area) predicted by the solid chill casting model

6.2. Water-Cooled Chill Castings

Figure 6.10 shows the thermocouple results obtained from the water-cooled chill casting. The behaviour is qualitatively similar to what was observed in the solid chill casting. The Bulkhead TCs 1 – 3, which are located 10 mm away from the chill, show a steep temperature drop for the first ~30 s followed by a more moderate rate of cooling during solidification. Bulkhead TC4 and TC6 follow the same trend (an initial rapid drop in the temperature for the first ~20 s, followed by a marginal decrease in the cooling rate). The Barrel TCs and the Water Jacket TCs, also follow this behaviour, but with a further reduction in cooling rate. Looking at the variation in cooling rate with distance from the chill, again the same trend as observed for the solid chill can be observed – i.e. a gradual decrease with increasing distance from the chill.

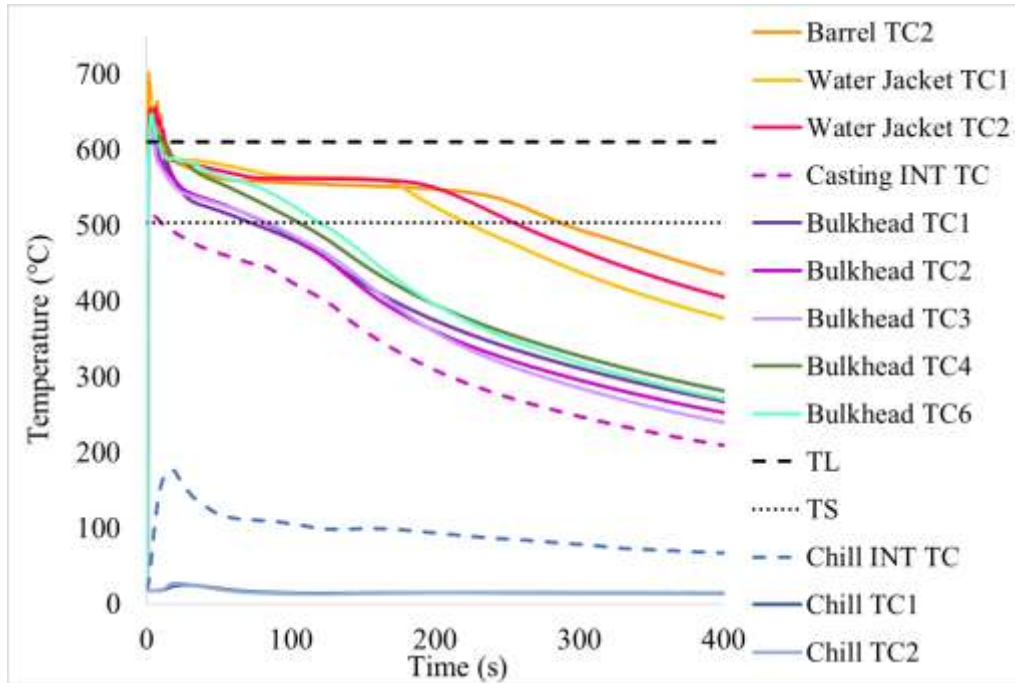


Figure 6.10: Temperature variation with time for various thermocouple locations within the casting and the water-cooled chill

Taking a more quantitative look, in comparison to the solid chill experiments, a higher cooling rate during solidification is achieved with the water-cooled chill – e.g. the interface TC indicates solidification in ~10 s compared with 90 s for the solid chill and the bulkhead TCs indicated solidification at TC1 and TC2 in 80 s compared with 110 s. There is also a significantly higher temperature difference maintained across the interface, which is the driving force for heat transfer. Moreover, the graphs show a stronger dependence of cooling rate with distance from the chill for the bulkhead area. This indicates that a larger heat extraction rate is achieved with the water-cooled chill for a sustained period of time, which is consistent with the increased difference in temperature across the interface.

Turning to the graphs for the chill, the chill interface TC shows a rapid initial increase in temperature to a maximum of 180 °C in the first ~25 s followed by a temperature drop to 100 °C and then a slow decline. Chill TC1 and TC2 show an approximately 10 °C increase in chill arch temperature in the first 25 s, and then the temperature drops to ~14 °C where it remains largely unchanged. This behaviour is very different than what was observed for the solid chill and reflects the high heat extraction capacity of the water cooling.

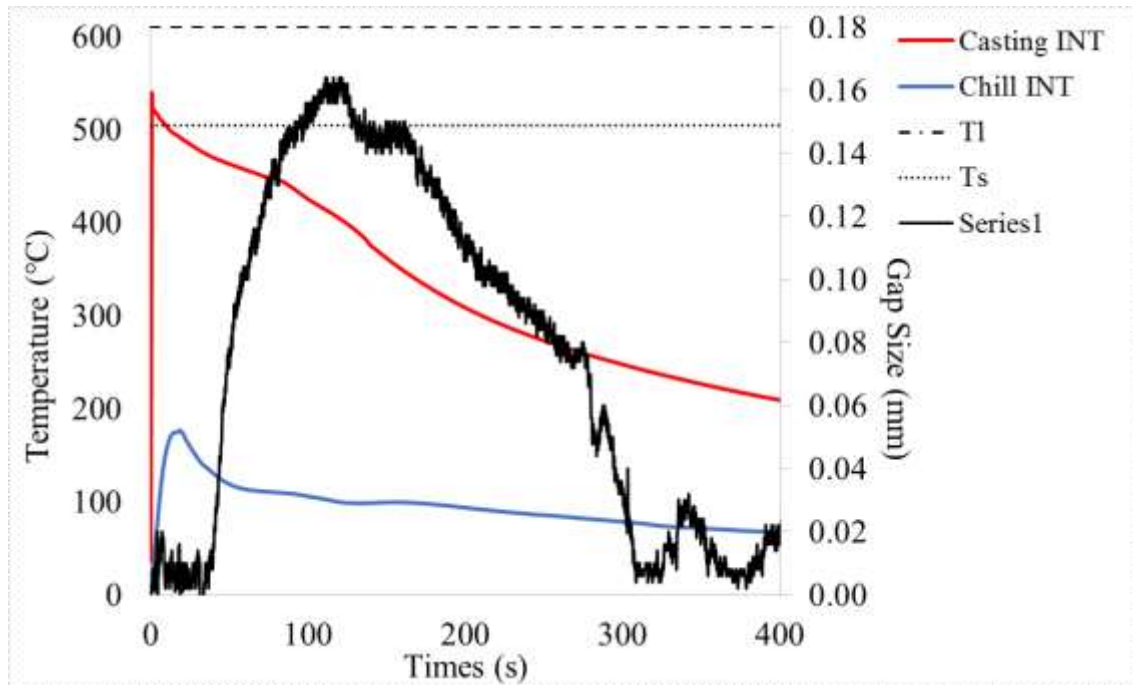


Figure 6.11: The evolution of the casting-chill interfacial gap with time in the water-cooled chill experiment

Figure 6.11 shows the evolution of the casting-chill interfacial gap with time for the water-cooled chill experiment together with the casting and chill interface temperature evolution. Comparing the casting and chill interface temperatures first, it is clear that a much larger driving force for heat transfer (temperature difference) is achieved and maintained for the first 400 s of the water-cooled casting in comparison to the solid chill casting.

In terms of the behaviour of the gap, there are noticeable differences between the gap behaviour for the water-cooled chill and the solid chill: 1) initially, an approximately 0.005 mm gap forms and the gap size remains fairly constant for ~38 s; 2) then the gap starts to grow and peaks at a value of 0.16 mm in ~110 s (which is shorter in duration compared to ~200 s in the solid chill casting experiment); and 3) following the peak, the gap drops to ~0.006 mm, whereas the gap drops to ~0.1 mm in the solid chill. As with the solid chill, the behaviour of the gap is complicated and difficult to interpret, therefore the development of the 3-D model is necessary.

Application of 3-D Model to the Water-cooled Chill Experiment – To try to understand the differences in the behaviour of the two chills with respect to both the temperature and the gap behaviour, the 3-D model has been applied to the casting with water-cooled chill conditions. Figure 6.12 shows a comparison between the model temperature predictions and the TC data at selected

locations in the casting bulkhead, casting barrel, and the water-cooled chill. As a reminder, the solid lines and dashed lines in the graph represent the experimental results, and the dotted lines show the model predictions. In addition, the dashed black line shows the liquidus temperature and the black dotted line shows the solidus temperature. As can be seen, good agreement is achieved between the model thermal results and the experimental thermocouple data in both the casting and in the chill. The model was also able to accurately predict the initial increase in chill temperature at the interface over the first 20 s followed by the gradually decrease beyond 40 s. The maximum disagreement between the model thermal predictions and the experimental thermal results is 5% in the casting interface thermocouple at 50 seconds and 5% in the Bulkhead TC2 at 150 seconds. Moreover, the maximum difference between the model thermal predictions and the experimental thermal results obtained from the chill thermocouples is ~30% at 5 seconds.

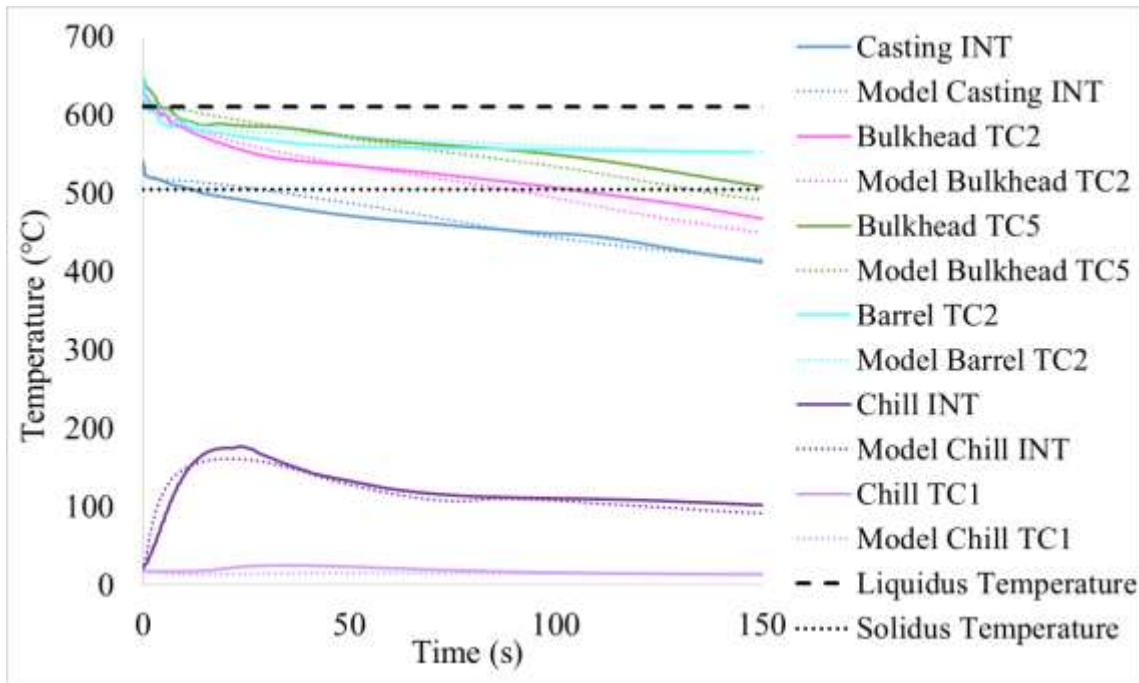


Figure 6.12: Comparison between the water-cooled chill model temperature predictions and the TC data at different locations in the bulkhead area

Figure 6.13 shows the evolution of the casting-chill interface gap with time obtained from the model and from the experimental data. The model predicts the correct trend in the evolution of the gap and the correct gap size (the latter to within approximately 20%). Notable differences include:

- 1) The rate at which the gap grows initially at approximately 40 s; and,
- 2) The peak in gap size (0.15 mm predicted by the model compared with 0.17 mm according to the LVDT measurements).

Importantly, both the model and the measurements agree on the early behaviour of the gap, in that it forms quickly but remains fairly constant and small at ~ 0.005 mm for ~ 40 s. This behaviour is consistent with the higher heat transfer rates achieved with the water-cooled chill in the initial stages of the casting process in comparison to the solid chill.

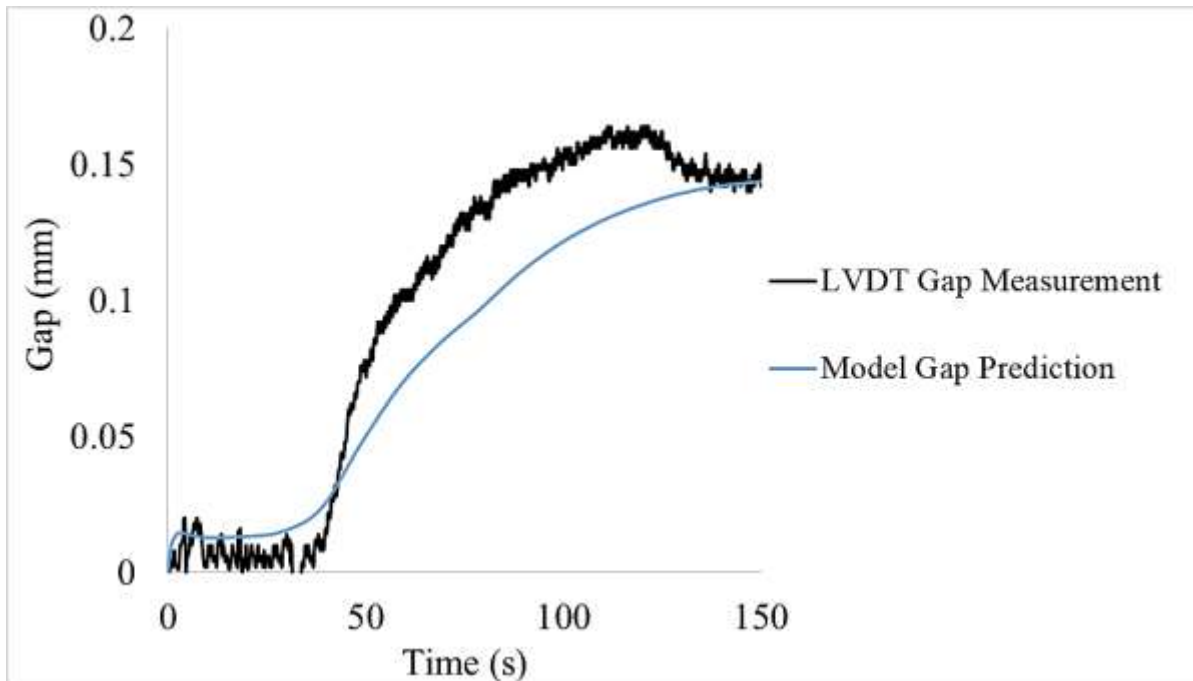


Figure 6.13: Comparison between the water-cooled chill-casting interface gap size measurements with LVDTs and the model predictions

Turning to a macro-view, Figure 6.14 shows the evolution of the displacement of the casting, the chill, and the sand mould cap with time together with the temperature contours, predicted by the 3-D model with water-cooled chill conditions, at 20, 50, 100, and 150 s. The displacements have been magnified by a factor of 10 to make the comparison easier. Similar to what was observed in the case of the solid chill model, the gap along the horizontal section at the top of the bulkhead, forms immediately and increases with time up to the end of the simulation at 150 s. Same as for the solid chill case, a pinch point is predicted to develop at the top of the arch. In contrast to the solid chill model, the gap at the bottom of the arch in the water-cooled chill model

cannot be observed during the first 50 s, which again confirms the presence of better contact between the casting and the water-cooled chill in the bottom of the arch.

The contours of temperature show a decrease in the casting temperature with time over the range of time plotted, similar to what was observed in the solid chill casting. In contrast, the temperature contours show far less heating in the chill. As was mentioned earlier, bending due to the development of thermal stresses in the chill is the other contributor to the development of the gap, particularly along the horizontal portion of the casting-chill interface. This is also observed but to a lesser extent in the water-cooled chill model. Figure 6.15 compares the formation of the gap along the horizontal interface between the solid and water-cooled chills. As can be seen, the gap behaves similarly for the first approximately 20 s. The gap in the water-cooled chill then remains approximately constant at 0.2 mm, whereas the gap in the solid chill continues to grow to a maximum of approximately 0.45 mm at the end of the simulation. Clearly, the water-cooling limits the bending in the chill.

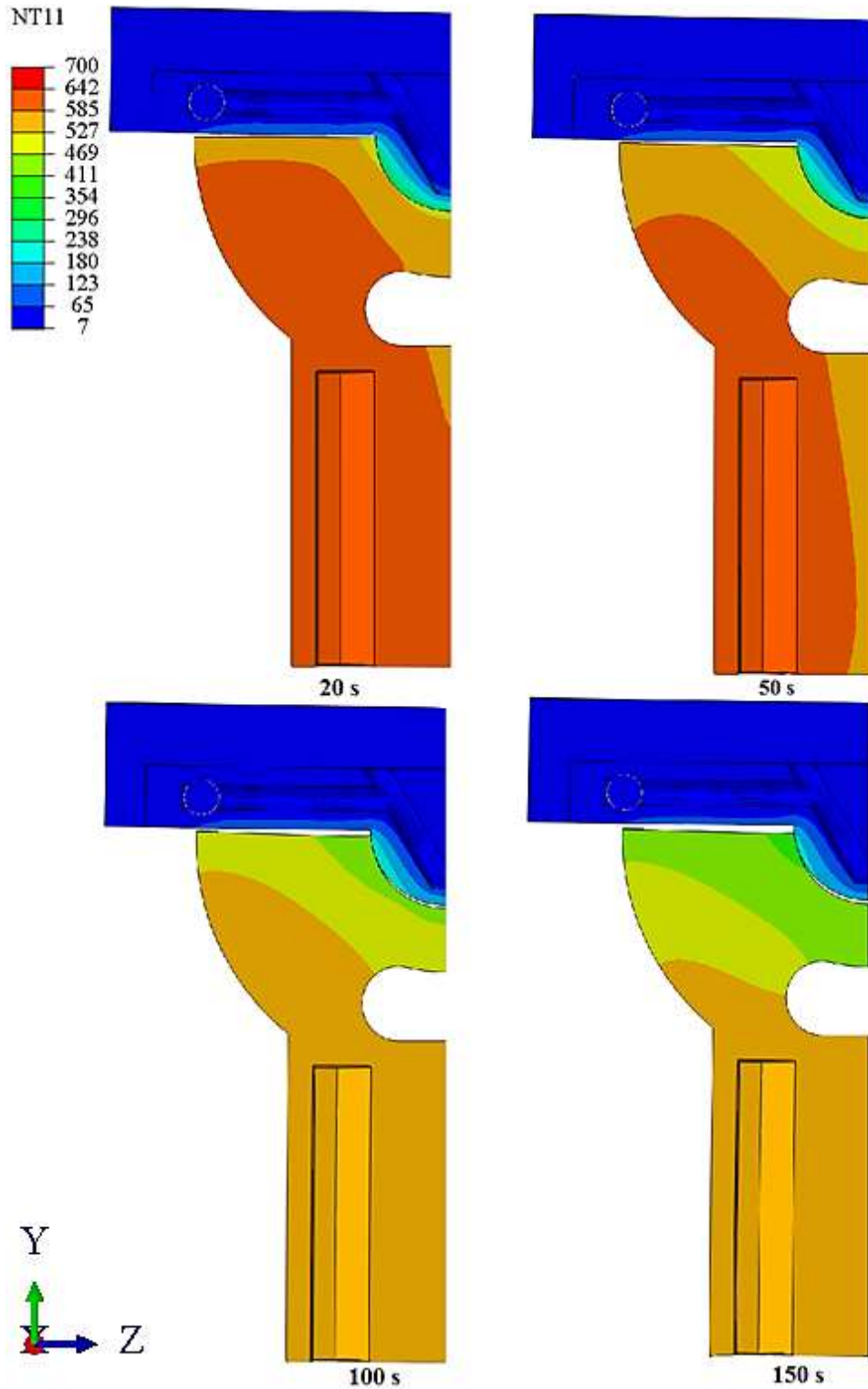


Figure 6.14: The evolution of the displacement in the casting, the chill, and the sand mould cap with time, and the temperature contours predicted by the water-cooled chill model (The deformation is magnified by a factor of 10, and the temperature unit is in °C.)

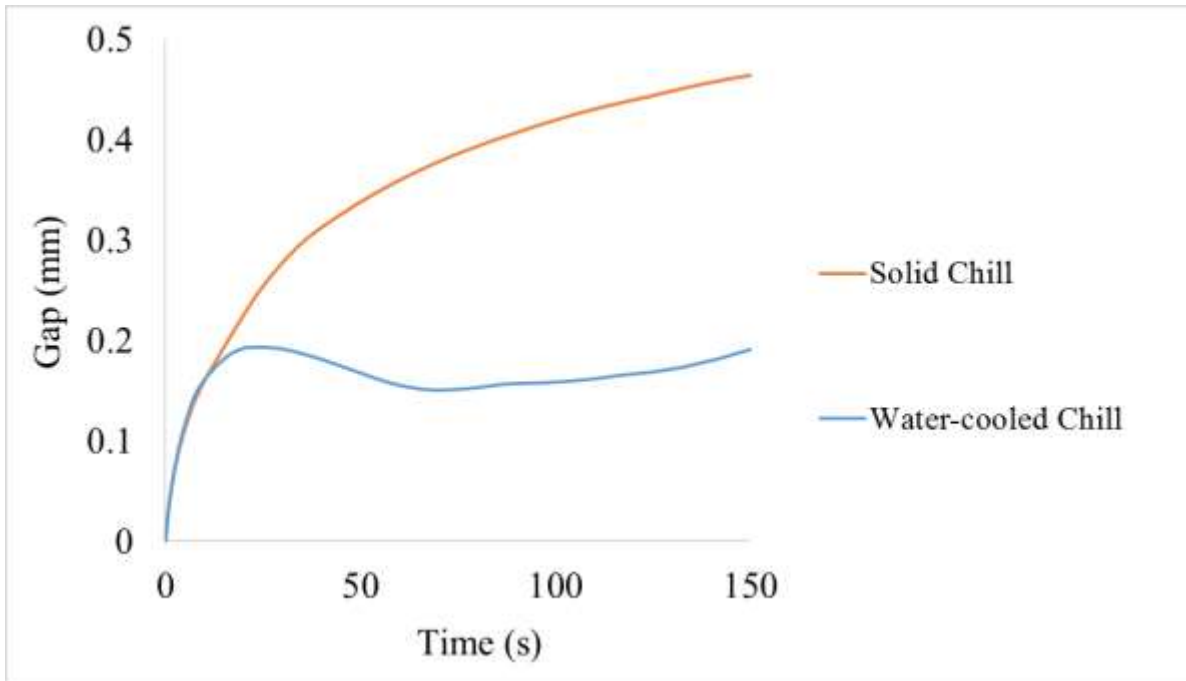


Figure 6.15: Comparison between the gaps predicted by the models at the horizontal casting-chill interfaces

Figure 6.16 shows a sequence of contour images illustrating the evolution of the contact pressure at the pinch point on the surface of the casting at 20, 50, 100, and 150 s. A pressure in the range of 20 to 43 MPa develops by 20 s. The contact area then gradually increases with time. The peak pressure appears to reach a maximum of approximately 52 MPa.

The development of the average contact pressure at the contact surface with time has been plotted in Figure 6.17. The results show that the average contact pressure at the pinch point increases slightly from 0 MPa to 1.1 MPa during the first 5 s, then continues to rise with a higher rate between 5 to 10 seconds to ~5 MPa. A more drastic increase in the average contact pressure takes place between 10 s to 62 s, to 23 MPa, and then reaches the peak value of ~25.5 MPa at 120 s, and finally, slightly decreases to 24.5 MPa at 150 s. Note as both the contact area and pressures are increasing as shown in Figure 6.17, the average results are different than the contour results.

Comparing these results with the results for the solid chill indicates that the contact pressure is much slower to develop in the water-cooled chill – e.g. the peak pressure takes approximately ~62 s to develop for the water-cooled chill compared with ~35 s for the solid chill. This is consistent with the water-cooling limiting thermal expansion of the chill, which is a

contributor to the development of the contact pressure, and the delay observed in the formation of the gap at the bottom of the arch.

In summary, the results presented so far show that the same two factors mentioned earlier for the solid chill case, are also responsible for the development of the interface gap in the water-cooled chill case. These include:

- 1) The contact pressure developed at the pinch point location; and
- 2) The thermal induced deformation of the chill

Both of these factors appear to have been reduced by water-cooling the chill. Moreover, the water-cooling also maintains a much higher temperature difference across the casting chill interface, which is the driving force for heat transfer.

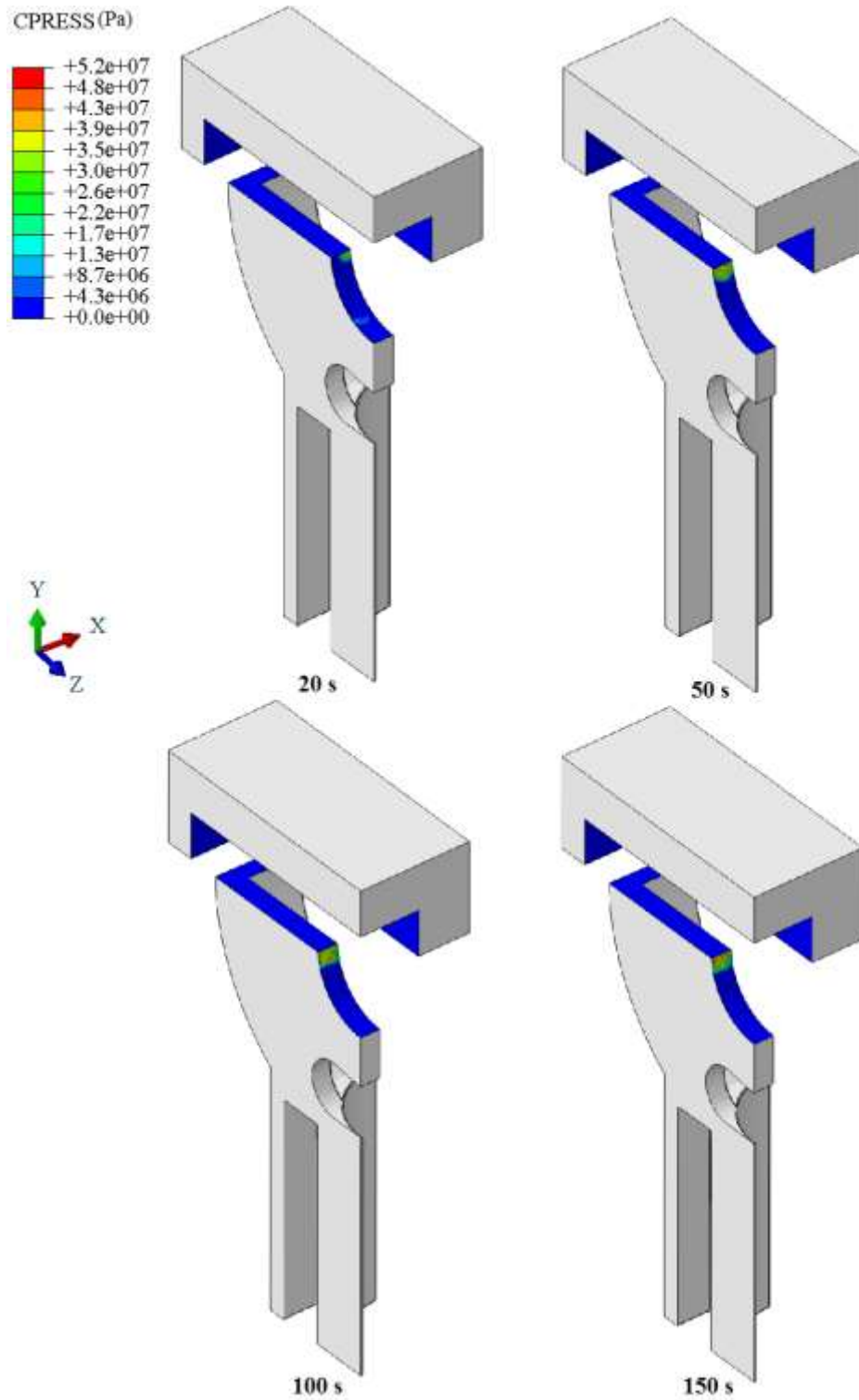


Figure 6.16: The evolution of the contact pressure at the pinch point predicted by the water-cooled chill model (The pressure unit is in Pa.)

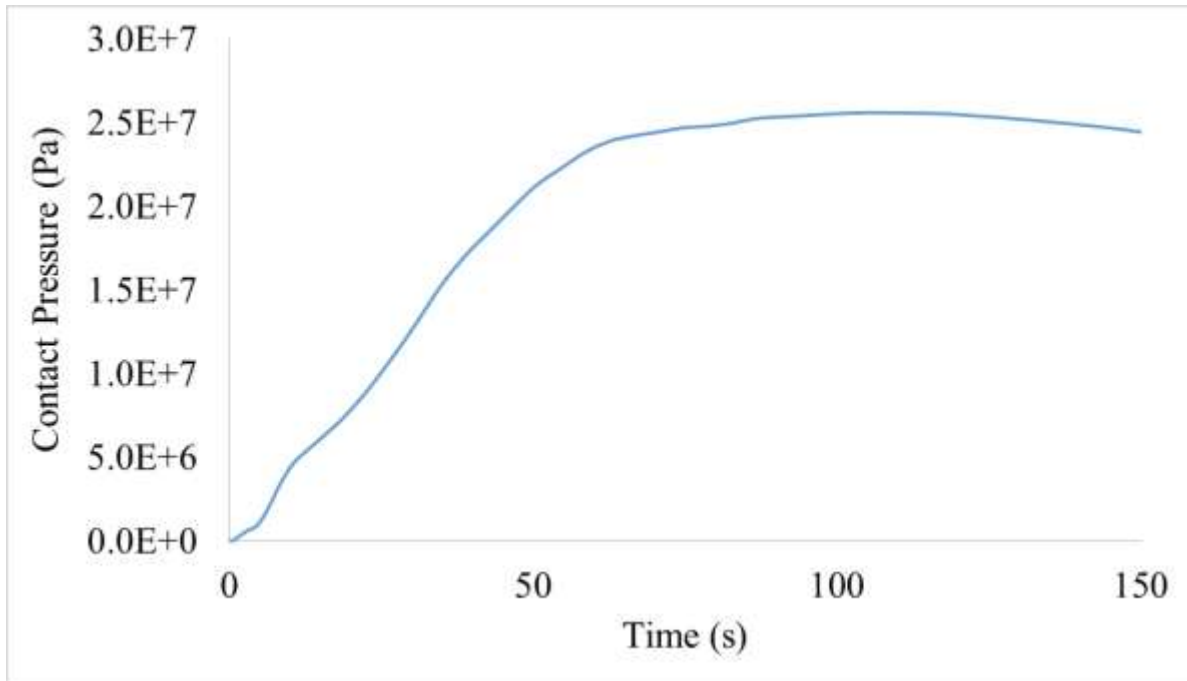


Figure 6.17: The evolution of the contact pressure at the pinch point/contact area (the values are the average of the contact pressure on the contact area) predicted by the water-cooled chill casting model

6.3. Delayed Water-Cooled Chill Castings

Figure 6.18 presents the cooling curves for the experiment in which water cooling was delayed for 10 s after the pouring process was finished. The casting cooling curves for this experiment show the same general behaviour as was observed with the solid chill and the water-cooled chill. It is interesting to note that the solidification times achieved with the delayed water-cooled chill are very similar, if not somewhat longer than with the solid chill.

Referring to the “Chill Interface TC”, a sharp initial increase can be seen at the interface temperature reaching a maximum of 200 °C in the first ~30 s followed by a rapid temperature drop to ~50 °C, which is due to switching the water on. The interface temperature then slowly increases to approximately 100 °C at 175 s, beyond which it slowly decreases. The peak temperature achieved in the chill at the interface is higher than the one observed in the water-cooled chill and the drop, following the peak, is to a lower temperature. The higher peak is consistent with the delay in water cooling. The larger drop is consistent with a larger interface gap and a reduction in heat transfer to the chill.

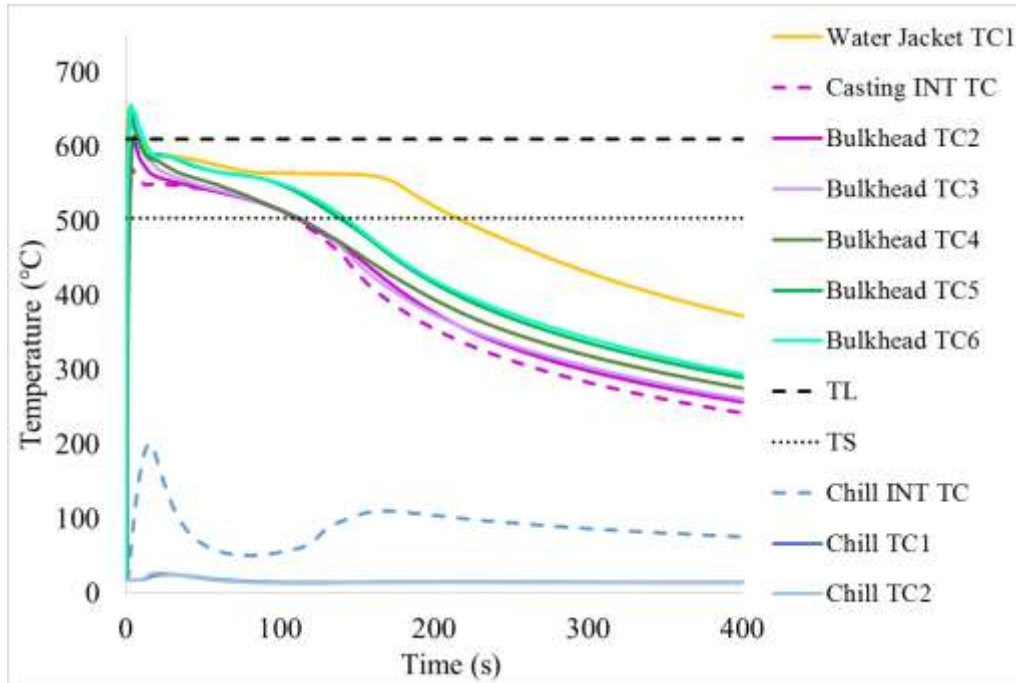


Figure 6.18: Temperature variation with time for various thermocouple locations within the casting and the water-cooled chill with 10 s delay in water-cooling

Figure 6.19 shows the evolution of the interface gap with time for the experiment in which water-cooling was delayed for 10 seconds. The gap starts to form and grow, reaching a peak of ~0.15 mm at approximately 50 s. The gap size then suddenly reduces for a short time, possibly reflecting shrinkage of the chill associated with the water cooling. The gap then quickly grows again, but peaks at a lower value. Note that the behaviour of the chill interface temperature largely reflects the behaviour of the gap; decreasing when the gap increases and increasing when the gap decreases, reflecting the change in the interface resistance to heat transfer associated with the gap. In comparison to the water-cooled chill experiment, there are two peaks in the interface gap and the first peak occurs at an earlier time, potentially consistent with the reduction in cooling rate observed in the delayed water-cooled chill casting compared with the water-cooled chill experiment. Note that the temperature difference across the interface is maintained at a high level, resulting in a much higher driving force for heat transfer than what was observed with the solid chill. As the resulting solidification rates were similar to those achieved with the solid chill, the heat transfer in the delayed water-cooled chill experiments appears to be strongly influenced by the behaviour of the gap.

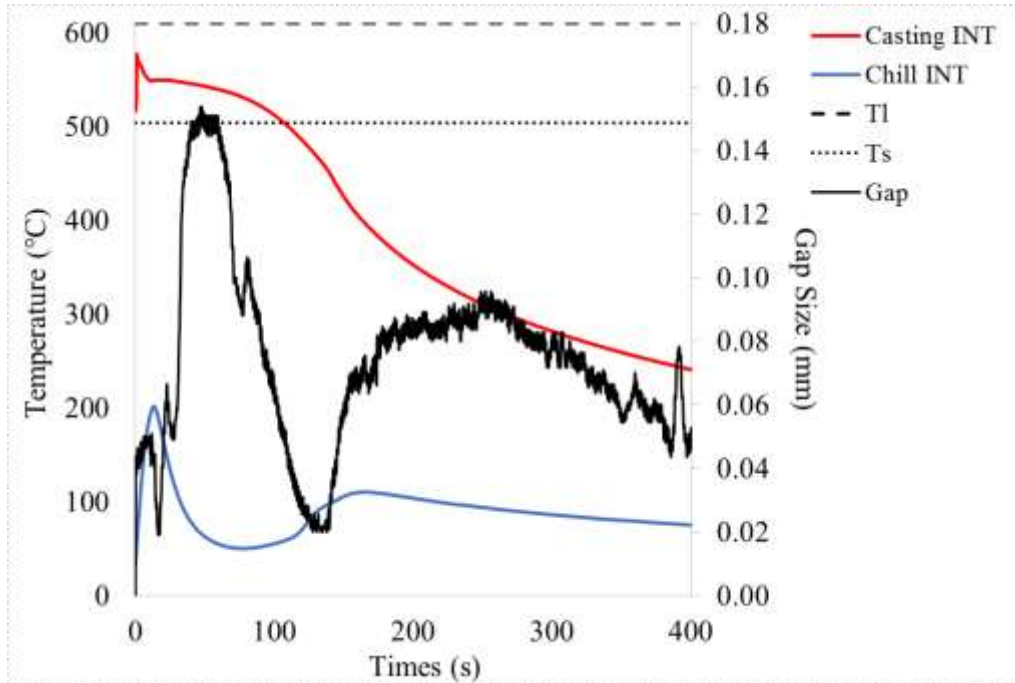


Figure 6.19: The evolution of the casting-chill interfacial gap with time in the delayed water-cooled chill experiment

Application of 3-D Model to the Delayed Water-cooled Chill Experiment – The behaviour of the gap in the delayed water-cooled experiment, again shows complicated behaviour that is also different than what was observed in the two previous cases. To unravel these differences the results from the 3-D model have been used. Figure 6.20 compares the model temperature predictions and the thermocouple readings. The agreement between the model and experimental thermal results is fairly good. The maximum disagreement between the model thermal predictions and the experimental thermal results is 7% in the casting interface and Bulkhead TC2 at 150 s, and 40 °C in the chill interface at 90 s.

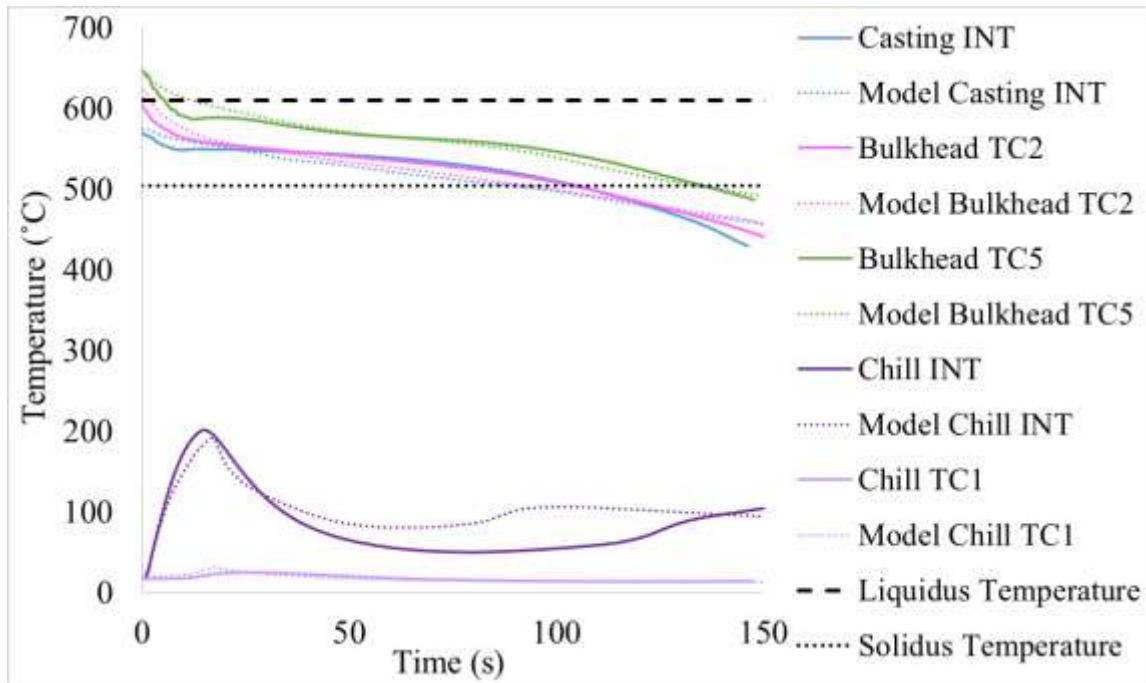


Figure 6.20: Comparison between the delayed water-cooled chill model temperature predictions and the TC data at different locations in the bulkhead area

Figure 6.21 compares the evolution of the interface gap with time obtained from the experiment with that predicted by the model. The model was able to reproduce the trend in the data, but with a larger quantitative discrepancy that was observed in the previous two simulations. The model is in good agreement with the experimental measurements up to 20 seconds, and then starts to deviate from the experimental results. The model predicts a much slower rate of gap growth and predicts that the gap reaches its maximum value at around 96 s, whereas the experimental measurements show that the gap reaches to 0.15 mm at ~40 s.

Note also, the sudden reduction in gap size observed at approximately 50 s (predicted at ~80 s in the model). This sudden reduction occurs much earlier in the delayed water-cooled casting than was observed in the other two castings (at ~100 s in the water-cooled casting and at > 200 s in the solid chill casting). The sudden decrease in gap size is likely due to the large drop in temperature observed in the delayed water-cooled casting associated with switching on the water – i.e. the chill contracts, hence, the pressure at the pinch point decreases and the chill slides back towards the casting. In the case of the water-cooled casting, the drop in chill temperature is far less severe and is associated with rapid growth in the gap. In the case of the solid chill, there is no drop in the chill temperature until approximately 300 s.

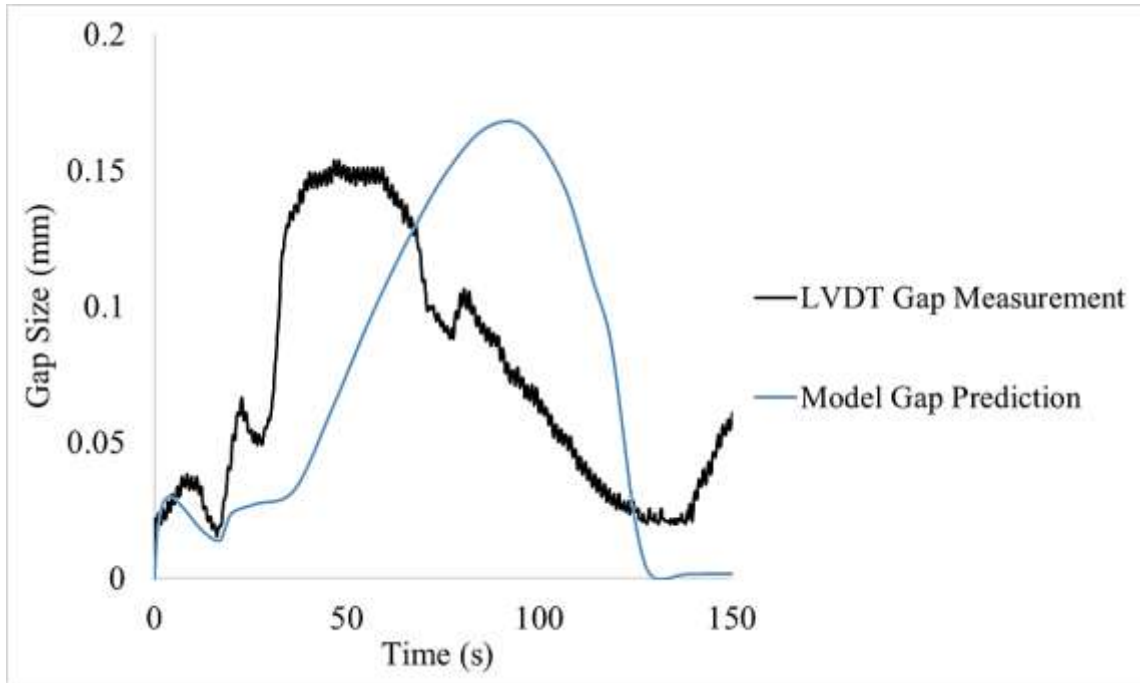


Figure 6.21: Comparison between the delayed water-cooled chill casting interface gap size measurements with LVDTs and the model predictions

Figure 6.22 shows the evolution of the displacement of the casting, the chill, and the sand mould cap with time together with the temperature contours, predicted by the 3-D model with delayed water-cooled chill conditions, at 20, 50, 100, and 150 s. The displacements have been magnified by a factor of 10, as in the previous plots. Similar to what was observed in the other casting formats, the pinch point starts to form from the beginning of the analysis and the gap along the horizontal section of the interface forms immediately and increases with time. As with the solid chill model, the gap at the bottom of the arch is predicted to start to form immediately but then reduces for a short period when the water-cooling starts as a result of thermal contraction of the chill. By 150 s there is no gap observable at the bottom of the arch; however, the gap remains along the flat portion of the interface at the top, due to bending of the chill. As the gap decreases, better physical contact between the casting and the chill is achieved, leading to an increase in the heat transfer between the two.

The contours of temperature show a decrease in the casting temperature with time up to 150 s. The model suggests that the chill temperature increases initially up to ~20 s and then decreases gradually with time as the water-cooling starts. As was previously seen in the other two cases, the bending due to the development of the thermal stresses in the chill also contributes to

the formation of the gap at the horizontal interface in this case. Comparing the deformation results at 20 s for the delayed water-cooled casting with the water-cooled casting, it is clear that there is a larger degree of bending in the delayed water-cooled case. This is likely due to the fact that the delay results in the chill heating up to a greater extent, which in turn causes larger thermal stresses to form.

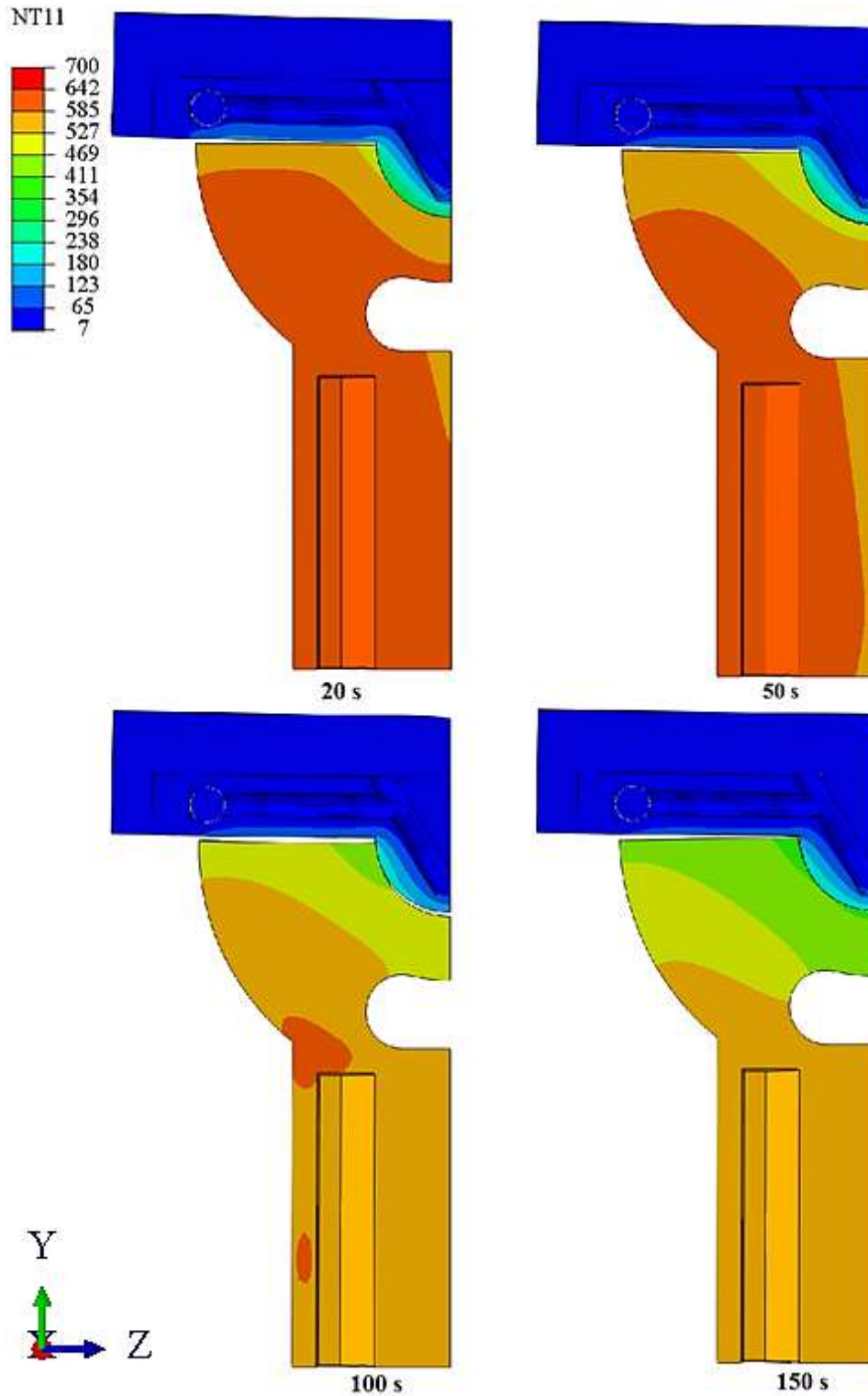


Figure 6.22: The evolution of the displacement in the casting, the chill, and the sand mould cap with time, and the temperature contours predicted by the delayed water-cooled chill model (The deformation is magnified by a factor of 10, and the temperature unit is in °C.)

Figure 6.23 shows the contour images illustrating the evolution of the contact pressure at the pinch point on the surface of the casting at 20, 50, 100, and 150 s. A pressure in the range of 15 to 44 MPa develops by 20 s. The contact area then gradually increase with time until ~100 s. At 150 s, the model predicts there to be no contact pressure at the pinch point, which is consistent with the reduction in gap observed at the bottom of the arch.

The development of the average contact pressure at the contact surface with time has been plotted in Figure 6.24. The results show that the average contact pressure at the pinch point increases slightly from 0 MPa to 12.8 MPa from 0 to 20 s, at which the water-cooling causes a decrease in the chill temperature, and the contact pressure drops slightly due to the thermal contraction of the chill. The contact pressure then continues to increase at approximately the same rate between 20 to ~86 seconds to ~25 MPa. The contact pressure then starts to decrease until 130 s when the model predicts that there is no more contact pressure at the interface. Note that the average results for the delayed water-cooling are different than the results for the other two cases. The rapid increase in chill temperature and then the abrupt reduction in chill temperature appears to have a significant impact on the dynamics of gap formation and subsequently heat transfer across the interface.

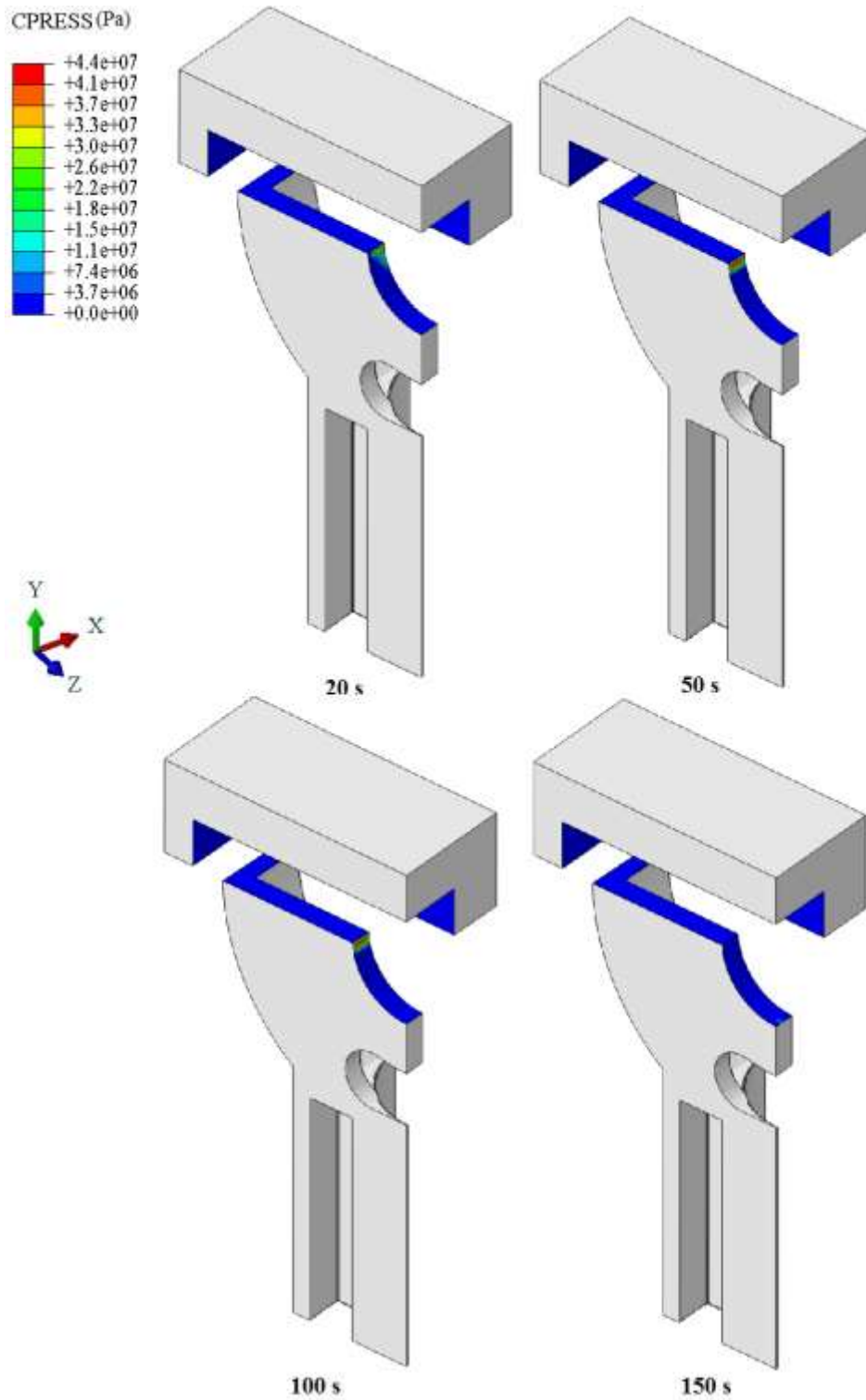


Figure 6.23: The evolution of the contact pressure at the pinch point predicted by the delayed water-cooled chill model (The pressure unit is in Pa.)

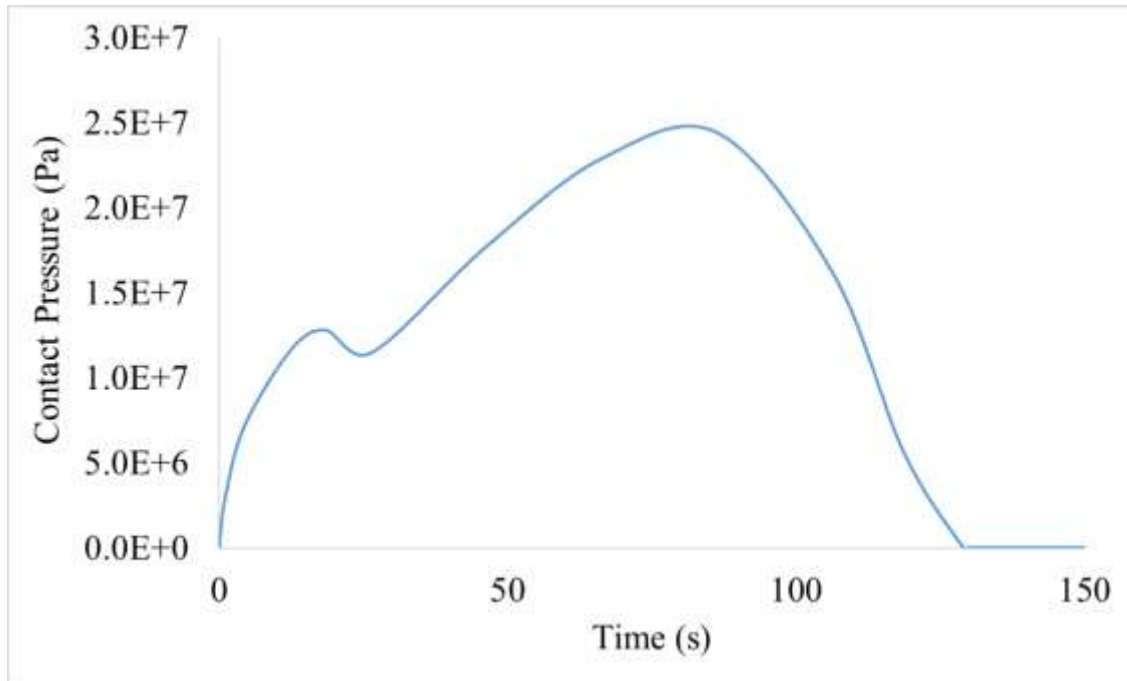


Figure 6.24: The evolution of the contact pressure at the pinch point/contact area (the values are the average of the contact pressure on the contact area) predicted by the delayed water-cooled chill casting model

6.4. The Effect of Water Cooling on Cooling Rate and Interface Gap Size

Figure 6.25 to Figure 6.28 present a comparison between the thermocouple results obtained from the solid chill casting, the water-cooled chill casting and the delayed water-cooling casting at different distances from the chill. The results are presented for the “Casting Interface TC”, for the “Bulkhead TC2”, which is located 10 mm from the chill interface, for “Bulkhead TC5”, which is located 30 mm from the interface, and for the “Water-jacket TC1”. All the castings had the same pouring temperature and same initial chill temperature. The cooling curves are limited to the temperature range between solidus temperature and liquidus temperature, which is the temperature range of relevance to refining the solidification microstructure.

These graphs show that increasing the heat extraction capacity of the chill by means of activating the water-cooling from the beginning of the casting process, results in a significant increase in the cooling rate of the casting and a reduction in the solidification time. The solidification time at 2 mm (casting interface) is reduced from 90 to 10 s, at 10 mm from 110 to

90 s, and for 30 mm from 150 to 130 s, for the water-cooled chill compared to the solid chill. Water-cooling could also reduce the solidification time in the water jacket TC1 by ~20 s.

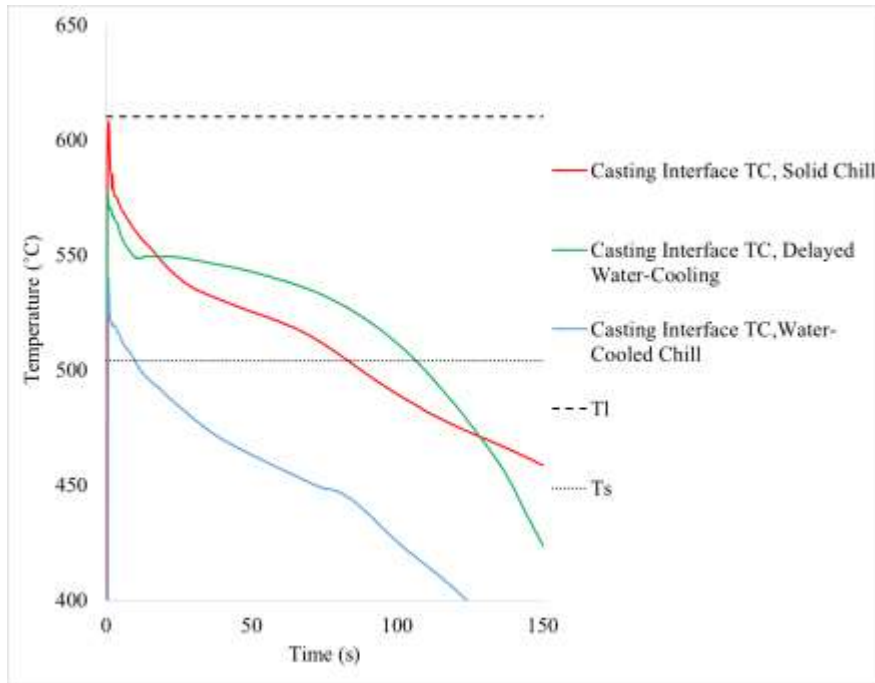


Figure 6.25: Cooling curve comparison between solid chill, delayed water-cooled, and water-cooled chill conditions

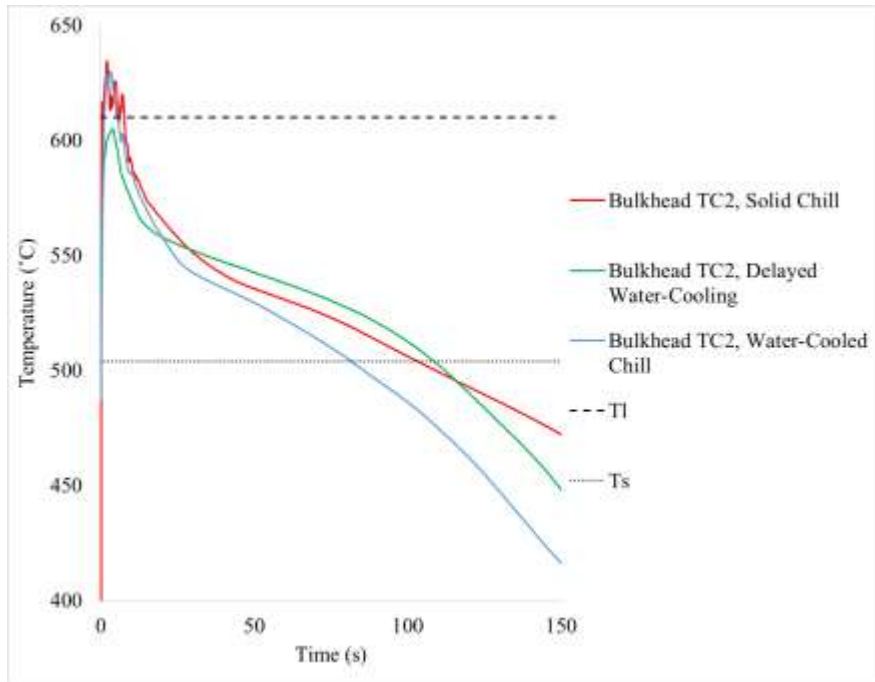


Figure 6.26: Cooling curve comparison between solid chill, delayed water-cooled, and water-cooled chill conditions

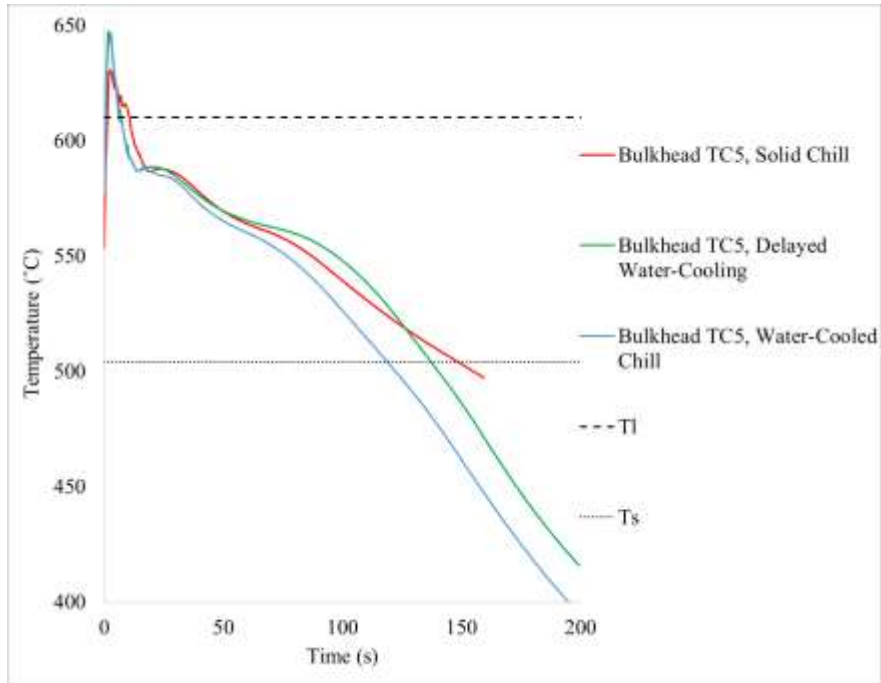


Figure 6.27: Cooling curve comparison between solid chill, delayed water-cooled, and water-cooled chill conditions

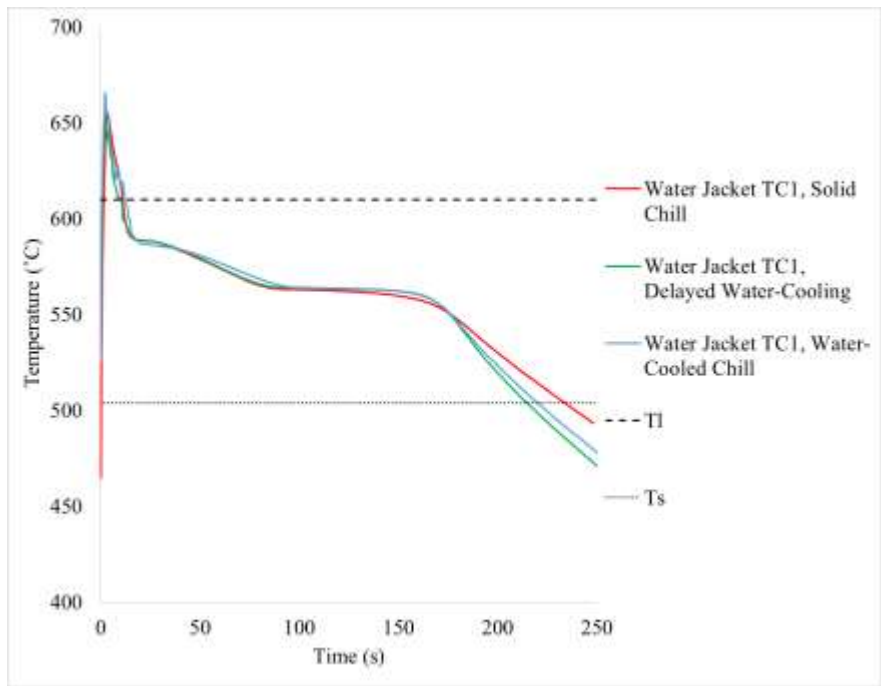


Figure 6.28: Cooling curve comparison between solid chill, delayed water-cooled, and water-cooled chill conditions

In contrast, the 10-second delay in water-cooling was not an effective method to decrease the cooling rate in the bulkhead near the chill, in spite of significantly increasing the heat extraction capacity of the chill and maintaining a high driving force for heat transport. However, the efficacy

of the delayed water-cooling does appear to increase with increasing distance from the chill – e.g. in Figure 6.27 and Figure 6.28, the overall solidification times achieved are lower than those achieved with the solid chill (in the water-jacket area the solidification time is close to that for the water-cooled casting without the delay).

To take a closer look, the evolution in the gap with time in the three casting has been compared in Figure 6.29. Based on this comparison, the early development of the gap is substantially different in the water-cooled casting in comparison to the other two. Little or no gap forms in the water-cooled casting until approximately 40 s, whereas a more substantial gap forms almost immediately in the solid chill and delayed water-cooled chill experiments. Moreover, the substantial growth in gap occurs at approximately 20 s in the solid chill and the delayed water-cooled chill, whereas gap growth does not occur until approximately 40 s in the water-cooled casting. The early and more dramatic loss of contact at the interface increases the resistance to heat transfer and decreases the cooling rate consistent with the decreased solidification rates observed. Based on the results obtained from the models (discussed in sections 6.1 to 6.3), early application of the water-cooling avoids the expansion of the chill and delays development of the contact pressure at the pinch point resulting in a better prolonged physical contact at the interface. All three casting formats ultimately yield similar peak gap sizes of approximately 0.15 mm. Thus, it appears that the early interface gap behaviour dominates the ability of the chills to extract heat from the bulkhead. The reduction in gap size observed with the delayed water-cooled chill casting at approximately 60 s appears to increase its ability to extract heat, but at a later time. In fact, it appears to approach the solidification times achieved with the water-cooled chill casting at locations farther from the chill.

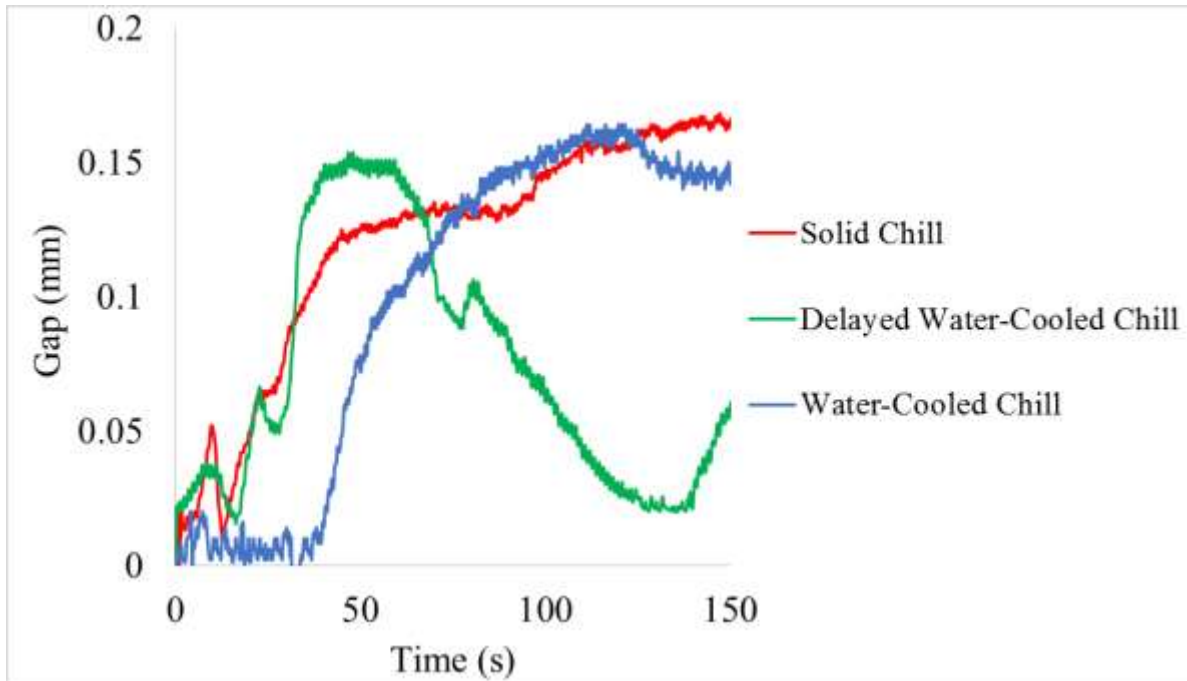


Figure 6.29: Comparison between casting-chill interface gaps obtained from the three experimental conditions

Figure 6.30 compares the size of the gap that was predicted by the model at the flat interface for the three cases (Note: the gap was output from the model at the top left of the casting bulkhead at one point of the horizontal interface). These results suggest that the gap formed in the flat interface in the solid chill case is almost twice the size of the ones developed in the other two cases. This can be explained by the fact that the water-cooling moderates the temperature gradients and thermal stresses that develop in the chill, resulting in a reduction in bending. The thermally induced bending of the chill together with the upward movement of the chill caused by the contact pressure that develops at the pinch point, contribute to the formation of the gap along the flat casting-chill interface. Thus, water-cooling positively impacts the two mechanisms of gap formation along the interface at the top of the bulkhead.

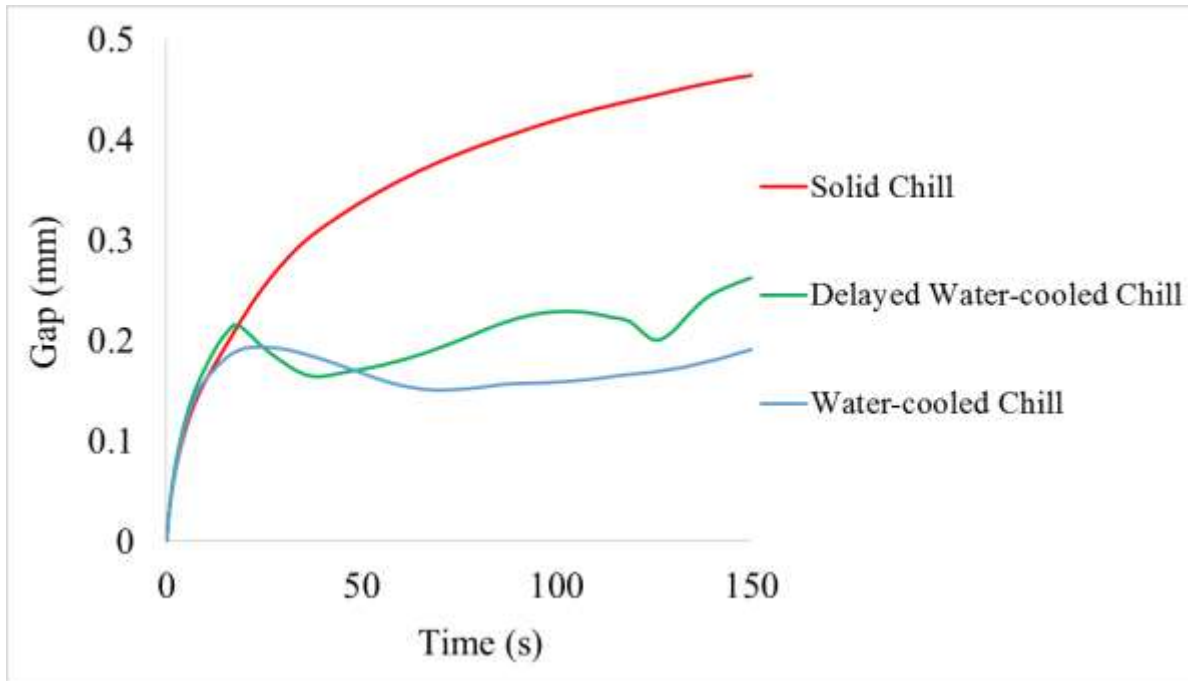
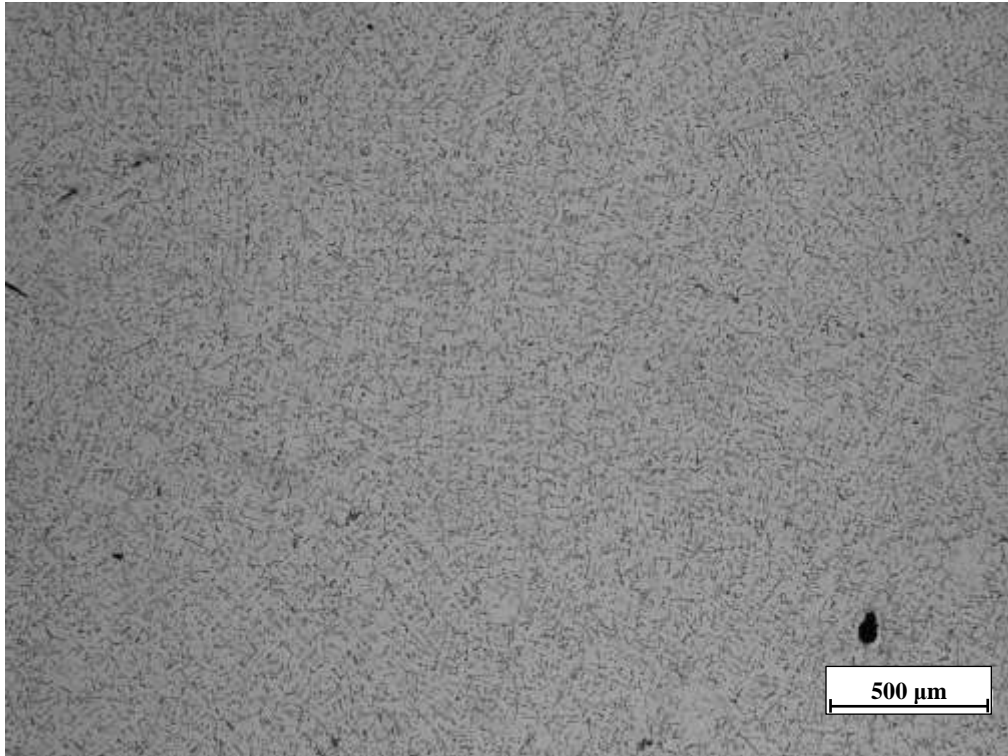


Figure 6.30: Comparison between casting-chill interface gaps obtained from the three experimental conditions

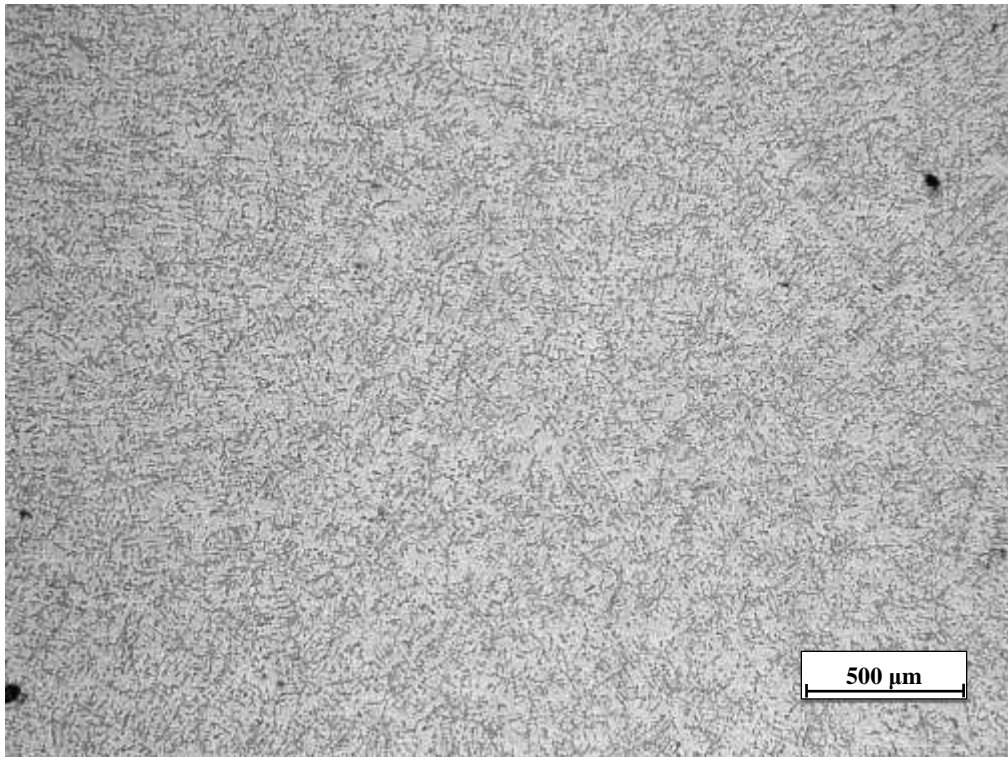
6.5.SDAS Size Comparison

In order to investigate the effect of cooling rate on microstructure, four metallographic specimens were taken from 5, 10, 15, and 20 mm from the chill at three angular locations on the arch: 1) along a line at 45° from the top surface of the chill; 2) along a line at 90°; and 3) along a line 135°.

Figure 6.31 to Figure 6.34 compare the optical microscope images at 5, 10, 15, 20 mm from the chill, respectively. In each figure, caption “a”, refers to the solid chill casting and caption “b” refers to the water-cooled chill casting. With some effort, it can be seen that the SDAS at the locations shown for the solid chill casting are slightly larger than that of the water-cooled chill casting.

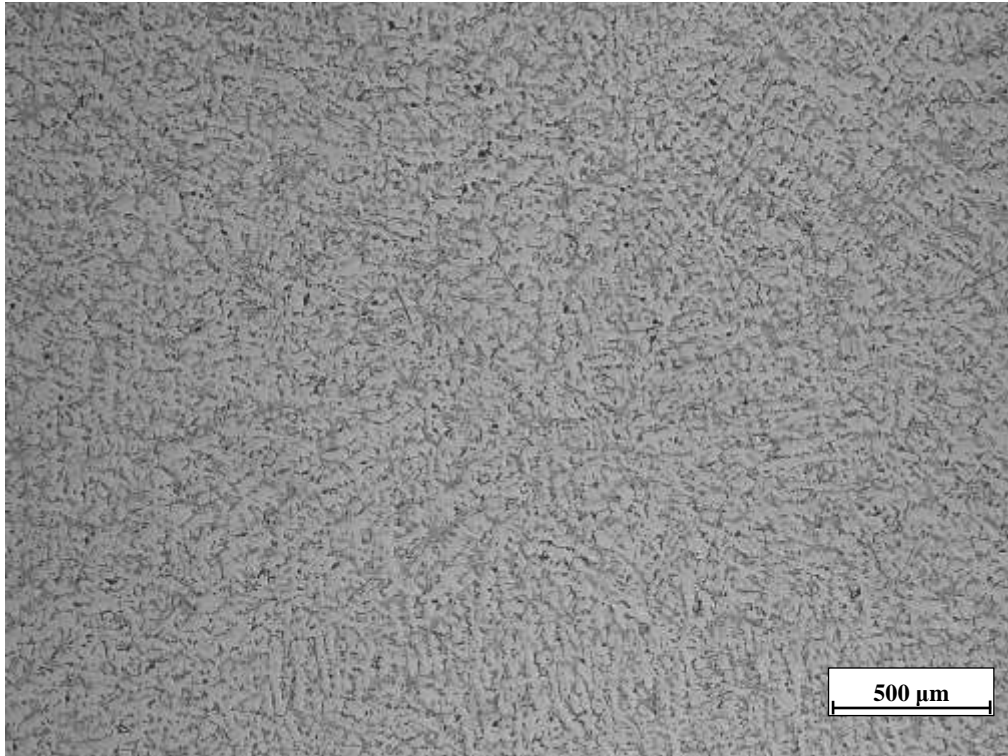


(a)

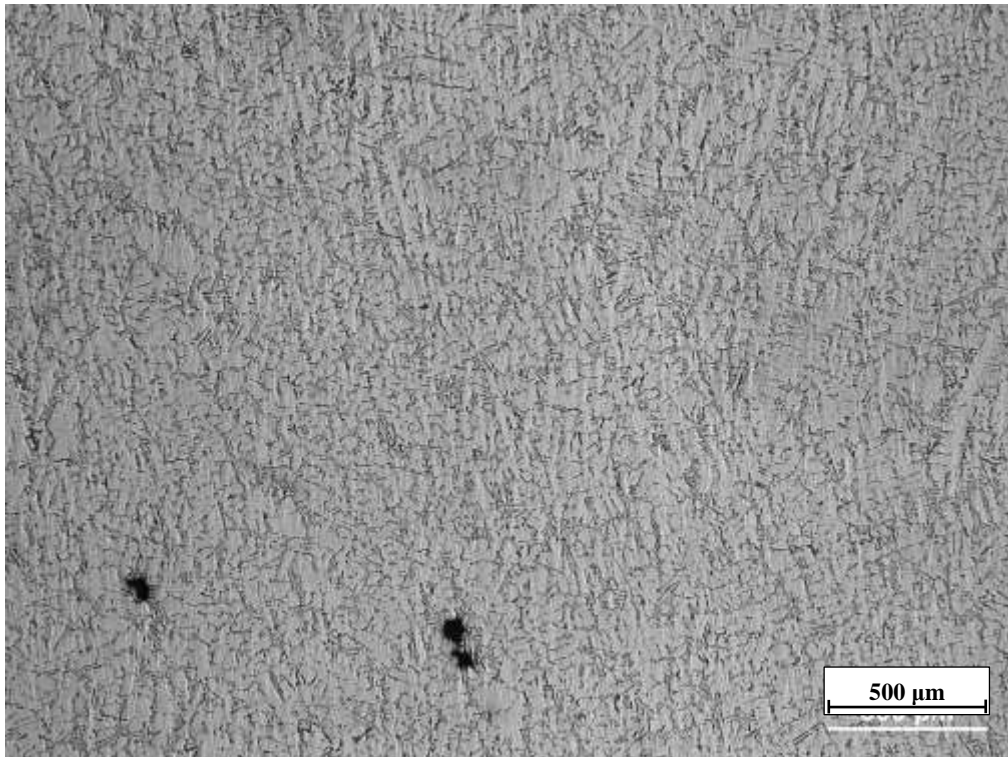


(b)

Figure 6.31: The microstructure of a) solid chill casting and b) water-cooled chill casting at 5 mm distance from the chill

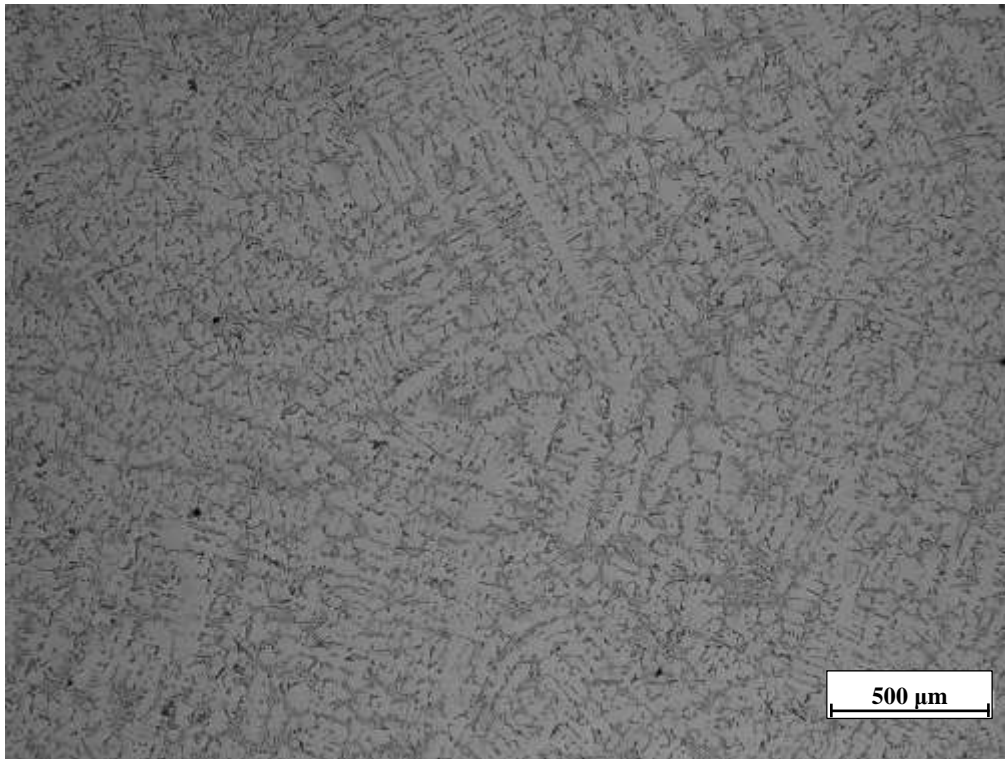


(a)

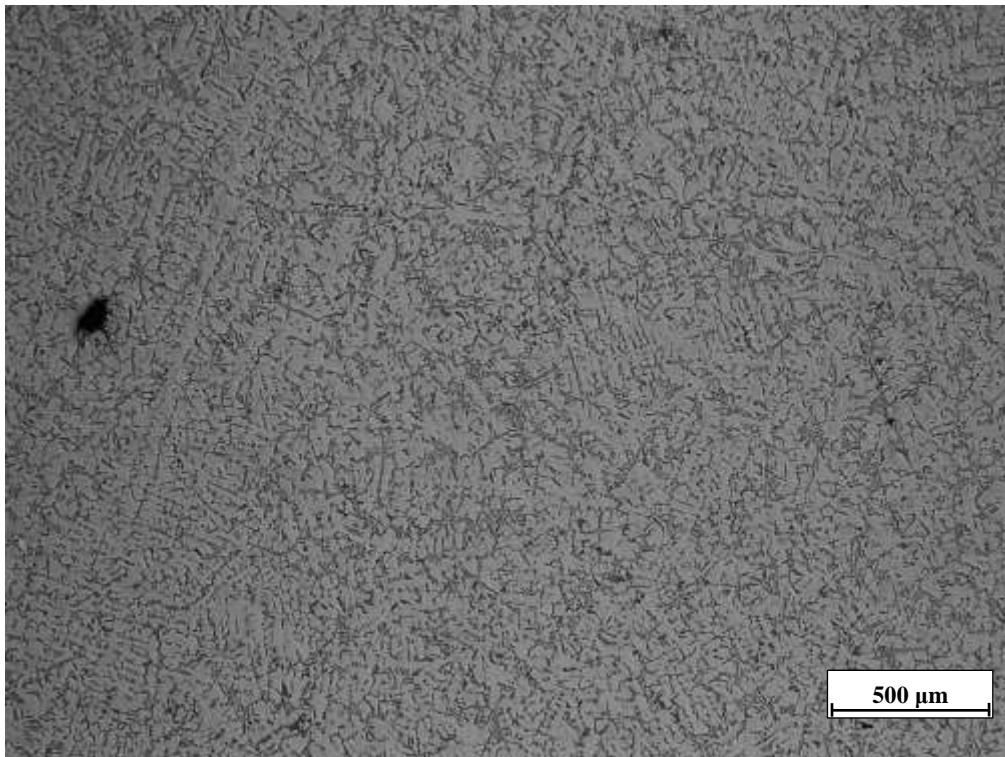


(b)

Figure 6.32: The microstructure of a) solid chill casting and b) water-cooled chill casting at 10 mm distance from the chill

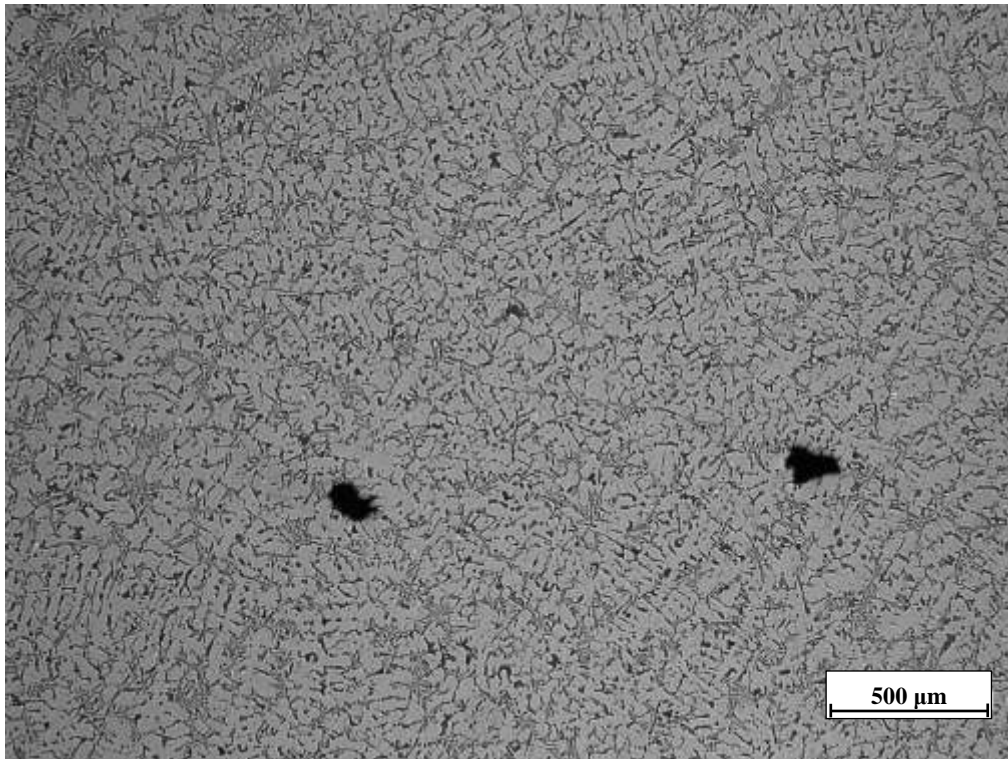


(a)

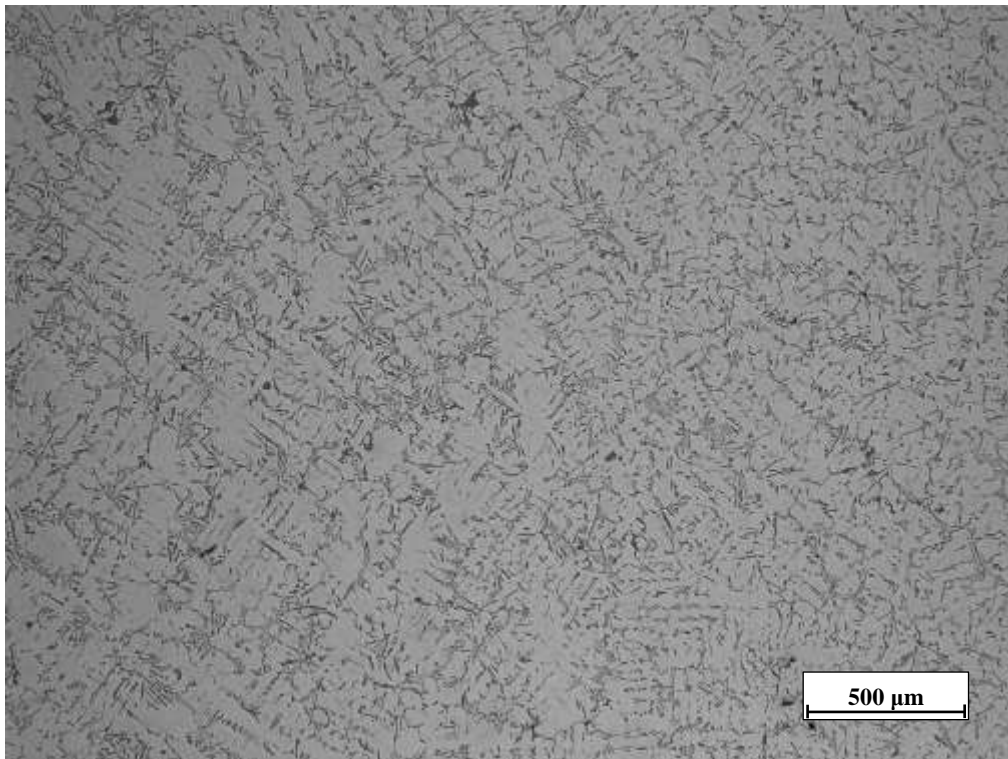


(b)

Figure 6.33: The microstructure of a) solid chill casting and b) water-cooled chill casting at 15 mm distance from the chill



(a)



(b)

Figure 6.34: The microstructure of a) solid chill casting and b) water-cooled chill casting at 20 mm distance from the chill

Figure 6.35 shows the SDAS variation with distance from the chill, for the solid chill casting and the water-cooled chill casting with and without the delay in water-cooling. The error bars represent the standard error. As can be seen, the microstructure of all of the castings becomes progressively coarser with increasing distance from the chill, as would be expected. The comparison between the SDAS measured for the three castings shows that the SDAS sizes for the water-cooled chill condition are 15 to 30% smaller than those of the solid chill and the delayed water-cooled chill castings. The delayed water-cooled chill method appears to have had a minimal influence on the SDAS, except in one location (15 mm from the chill) at which the cooling rate was slightly lower than that of the solid chill casting and the SDAS was decreased by 7%.

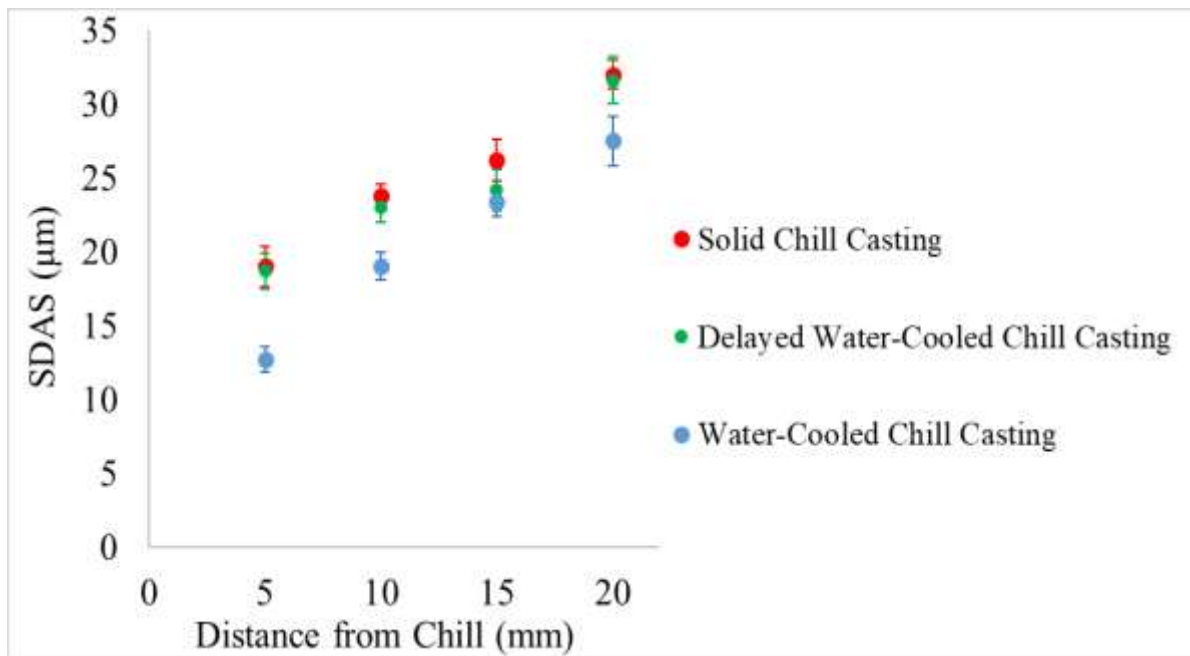


Figure 6.35: Variation of SDAS with distance from the chills

To quantify the effect of cooling rate on microstructure, a mathematical relationship between the cooling rate and SDAS size has been derived. Flemings [55] suggested a mathematical relationship between SDAS and cooling rate as shown below:

$$SDAS = a(\dot{T})^{-n}, 0.3 < n < 0.5 \quad \text{Equation 6.1}$$

where \dot{T} ($^{\circ}C$) is the cooling rate, and a is a constant.

The cooling rates at different locations were calculated by the following expression:

$$\dot{T} = \frac{T_{Liquidus} - T_{Solidus}}{t_{Liquidus} - t_{Solidus}} \quad \text{Equation 6.2}$$

where $T_{Liquidus}$ is the liquidus temperature ($^{\circ}\text{C}$), $T_{Solidus}$ is the solidus temperature ($^{\circ}\text{C}$), $t_{Liquidus}$ is the time (s) at which the melt is at liquidus temperature, and $t_{Solidus}$ is the time (s) at which solidification is complete based on the thermocouple data at the locations being analysed in the casting experiments.

To confirm that the interpretation of the microstructure data in terms of the SDAS is reasonable and in agreement with past work on aluminium foundry alloys, a correlation has been developed between SDAS and cooling rate of the form shown in Equation 6.3. This equation has been widely used in the literature (example references include: [25,107-109]). The results of fitting this correlation to the experimental results are shown in Figure 6.36. These results are in agreement with the relationship suggested by Flemings quite well, yielding values for a and n of 28.57 and -0.49, respectively. The R^2 value for this fitting is 0.95 which indicates a good fit to the experimental data.

$$SDAS = 28.57(\dot{T})^{-0.49} \quad \text{Equation 6.3}$$

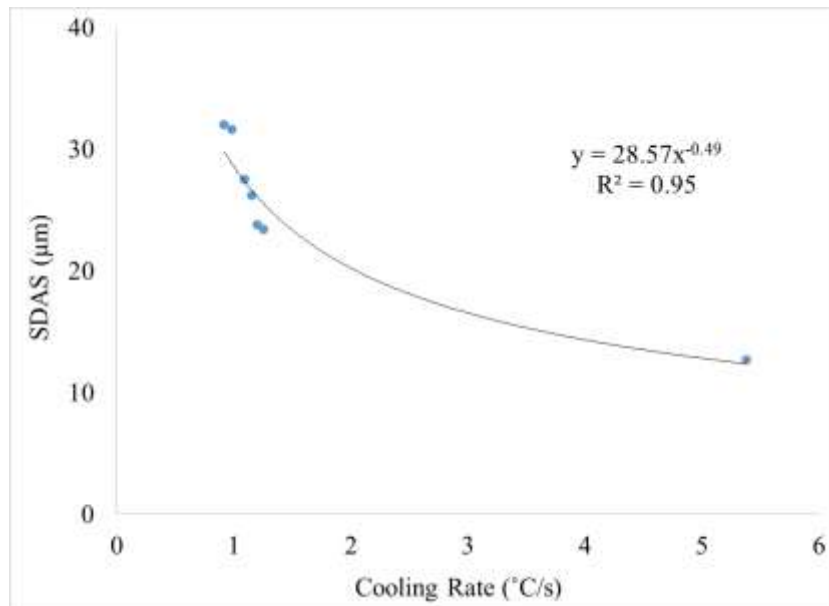


Figure 6.36: Variation of SDAS with cooling rate (data obtained from the three casting experiments)

7. Summary, Conclusions, Contributions and Future Work

In the current research, the efficacy of using a water-cooled chill to refine the microstructure in the bulkhead area in A319 engine blocks was assessed. The objective was to explore whether or not water-cooling the chill would decrease the SDAS in the main bearing bulkhead and thereby, potentially improve the fatigue life of the newer generation of lightweight engine blocks. To achieve this, a total of 12 casting experiments were performed using sand mould packages based on a section of a 4-cylinder engine block, provided by “General Motors Co.” and “Highland Foundry Ltd.”.

Following preliminary development work, the main experimental data were obtained from three castings using the Highland Foundry format. The solid H13 chill used in the experiments is identical to that currently being used in the industry. The H13 water-cooled chill was designed at UBC as a part of this research work. The test castings were instrumented with both thermocouples (at various locations) and LVDTs to measure the displacement of the casting-chill interface at the bottom of the arch (main bearing saddle).

To attempt to fully understand heat transport in the various casting formats examined, it was necessary to develop a series of coupled thermal-stress mathematical models, which were able to predict the temperature and displacement variations with time within the casting and the chill. These models were developed in commercial Finite Element package “ABAQUS” version 2016, which is reported to have advanced contact interface capabilities. A preliminary 2-D thermal-stress model was developed first to explore:

- 1) The role of the mould package components on the formation of the casting-chill interface gap;
- 2) The role of the mechanical and thermal boundary conditions on the formation of the casting-chill interface gap; and,
- 3) The role of the constitutive behaviour of the A319 and the bonded sand mould on interface gap formation.

The 2-D model was followed by the development of a 3-D model. Three versions of the 3-D model were developed:

- 1) A solid chill version;
- 2) A water-cooled chill version (with no delay); and,
- 3) A water-cooled chill version with 10 s delay in water-cooling.

The 3-D model domain was limited to a ¼ section of the casting, the chill, and the sand mould cap, in order to reduce the computational time. The model was verified using the thermocouple and LVDT data collected from the three main experimental test castings. To the author's knowledge, this work is the first to utilize a water-cooled chill in the precision bonded sand mould to cast sections of engine blocks, and the results suggest that it has the potential to refine the microstructure of the final product in main bear bulkhead area.

To quantitatively determine the effect of the reduction in the cooling rate on refining the microstructure of the A319 alloy, a series of metallography tests were carried out on samples extracted from the castings and the SDAS were measured using the "ImageJ" software.

The main conclusions and suggestions for future work are summarized in the next two sections.

7.1. Conclusions

Through the course of this research, it was concluded that:

- 1) The development of the interface gap between the chill and the casting plays a major role in interface thermal resistance behaviour and the ability of the water-cooled chill to refine the bulkhead microstructure.
- 2) The formation of the gap is complicated and is influenced by a number of factors including: the thermal contraction/deformation of the casting; the thermal expansion/deformation of the chill; the constitutive behaviour of the casting; the constitutive behaviour of the bonded sand mould cap; and, the geometry of the casting-chill interface.
- 3) The use of a water-cooled chill, with no delay in the water-cooling process, was shown to increase the cooling rate in the bulkhead area, and decrease the SDAS size by 15 to 30% up to 30 mm from the chill. Therefore, this method can potentially improve fatigue properties of the alloy in the main bearing bulkhead.

- 4) Regarding the LVDT gap measurements, conclusion 3 results from better contact between the casting and the chill in the water-cooled chill experiment in comparison to the solid chill and the 10 s delayed water-cooled chill experiments. Specifically, early gap formation was negligible in comparison to the gaps that formed with the other two formats.
- 5) The 10 s delay in water cooling allowed the chill to briefly heat up and expand resulting in the formation of contact pressure at the pinch point displacing the chill upward.
- 6) The thermal stress analysis revealed two reasons for the loss of contact at the casting-chill interface:
 - a) The development of a pinch point at the sides of the chill arch, where the casting shrinks on the chill while the chill expands, pushing the chill upward. This is believed to be the main contributor to the gap development at the interface.
 - b) The chill bends as a result of the development of thermal stresses due to heat transfer. The bending contributes to the development of the gap along the horizontal portion of the interface.

7.2. Contribution to the State-of-the-Art

In this thesis, a novel water-cooled chill was designed and tested for the purpose of increasing the cooling rate during solidification in the main bearing bulkhead in the precision bonded sand casting process. A sophisticated thermal-stress analysis was conducted in the commercial software package ABAQUS, which was shown to accurately reproduce the behaviour observed in the solid chill, the delayed water-cooled chill and the water-cooled chill experiments in terms of both the evolution of temperature in the casting and the chill, and the gap at the casting chill interface. The model confirmed that water cooling the chill has two important effects to improve heat transport:

- 1) A large driving force for heat transfer is maintained across the casting chill interface; and
- 2) Deformation of the chill is reduced helping to maintain a better physical contact between the casting and the chill, hence, a higher interfacial heat transfer coefficient.

Prior to completing the experimental program and companion numerical analysis presented in this thesis, the role of gap formation on heat transfer between the chill and the main bearing bulkhead in the precision bonded sand casting of engine blocks was not known, nor obvious to one

skilled in the art (practitioners in the engine block casting industry). The results of this work have shed light on the importance of gap formation, and that, its behaviour needs to be considered in process design. As a result of the comprehensive numerical analysis, the role of the contact area/pinch point and bending of the chill on the development of the gap at the casting-chill interface was clearly elucidated for the first time. Developing a strategy to mitigate/reduce gap formation in the main bearing bulkhead-chill interface will not be straightforward. The model developed in this dissertation maybe used to explore different techniques for improving casting-chill interface contact. Together with water-cooling, these might include changes to the geometry of the chill and/or the mould, and preheating the chill prior to water-cooling. These strategies will be explored with the industrial partners that supported this work.

7.3. Recommendations for Future Work

Additional areas of research include:

- 1) Despite several attempts, convergence problems were encountered with ABAQUS when a combined pressure-displacement boundary condition was used. As clearly, both conditions can prevail, further work is needed to resolve this issue.
- 2) Fatigue tests should be performed on samples taken from the castings made in different experimental conditions to quantitatively assess the effect of the current SDAS refinement on the fatigue life of the component.
- 3) The length scales of other microstructural features such as porosity should also be examined, as they are typically fatigue limiting;
- 4) Running the model with different mould designs to explore the possibility of improving the contact at the casting-chill interface by changing the mould design.
- 5) Future work is needed to develop the model in a different software with fluid flow analysis capability to include the mould filling process in the simulation.

References

- [1] F. Farhang Mehr, S. Cockcroft, D. Maijer, A Coupled Thermal-Stress Model of A319 Alloy Chilled Sand Casting, *Shape Casting: 6th International Symposium 2016* (195-202), Springer International Publishing.
- [2] F. Farhang Mehr, S. Cockcroft, C. Reilly, D. Maijer, Evaluation of the Casting/Chill Interface Thermal Behaviour During A319 Alloy Sand Casting Process, *Advances in the Science and Engineering of Casting Solidification*, (2015) 373-380, Springer International Publishing.
- [3] P. Bastani, J. Heywood, C. Hope, US CAFE Standards: Potential for Meeting Light-Duty Vehicle Fuel Economy Targets, 2016-2025, (2012).
- [4] R. Mackay, G. Byczynski, The Use of the Weibull Statistical Method to Assess the Reliability of Cast Aluminum Engine Blocks Made from Different Casting Processes, *Shape Casting: 4th International Symposium*, (2011) 191-198, John Wiley & Sons, Inc.
- [5] C.J. Bettles, C. Forwood, D. StJohn, M. Frost, D. Jones, M. Qian, G. Song, J. Griffiths, J.F. Nie, AMC-SC1: An Elevated Temperature Magnesium Alloy Suitable for Precision Sand Casting of Powertrain Components, *Magnesium technology*, (2003) 223-226.
- [6] R.I. Mackay, D. Cusinato, J.H. Sokolowski, Chemistry optimisation to improve casting durability of engine blocks, *International Journal of Cast Metals Research*, 23 (2009) 137-149.
- [7] R.W. Grenkowitz, M.J. Braskich, A.D. Ackerman, Gravity precision sand casting of aluminum and equivalent metals, *Gravity precision sand casting of aluminum and equivalent metals. United States Patent*, 5,620,044 (1997).
- [8] F. Farhang Mehr, C. Reilly, S. Cockcroft, D. Maijer, R. MacKay, Effect of chill cooling conditions on cooling rate, microstructure and casting/chill interfacial heat transfer coefficient for sand cast A319 alloy, *International Journal of Cast Metals Research*, (2014) 288-300.
- [9] L. Heusler, F. Feikus, M. Otte, Alloy and casting process optimization for engine block application, *AFS Transactions*, 109 (2001) 443-451.
- [10] F. Farhang Mehr, Quantitative assessment of the effect of copper chills on casting/chill interface behavior and the microstructure of sand cast A319 alloy, *Master's Thesis*, The University of British Columbia, Vancouver, Canada (2012).
- [11] P.R.S. Moorey, *Materials and Manufacture in Ancient Mesopotamia: The Evidence of Archaeology and Art: Metals and Metalwork, Glazed Materials and Glass*, BAR, (1985).
- [12] E. Kotzin, M. Lessiter, *Timeline of Casting Technology, Modern Casting (USA)*, (2002) 43-44.

- [13] D.M. Stefanescu, ASM Metals Handbook, Volume 15: Casting, ASM International, (1992).
- [14] S. Sulaiman, A. Hamouda, Modeling of the thermal history of the sand casting process, Journal of Materials Processing Technology, 113 (2001) 245-250.
- [15] D.W. Scott, H. Li, J. Griffin, E.C. Bates, Production and Inspection of Quality Aluminum and Iron Sand Castings, Handbook of metallurgical process design, 24 (2004) 349.
- [16] J. Campbell, Cosworth Research, Casting of metal articles. United States patent US 4,693,292. (1987).
- [17] R.M. Glenn Byczynski, THE NEMAK COSWORTH CASTING PROCESS - INNOVATION, Shape Casting, 3rd International Symposium, (2009) 199-206.
- [18] H. Arami, R. Khalifehzadeh, M. Akbari, F. Khomamizadeh, Microporosity control and thermal-fatigue resistance of A319 aluminum foundry alloy, Materials Science and Engineering: A. 472 (2008) 107-114.
- [19] E.L. Rooy, ASM Metals Handbook, Volume 2: Properties and selection: Nonferrous alloys and special-purpose materials, ASM International, (1992).
- [20] R.I. Mackay, J.H. Sokolowski, Effect of Si and Cu concentrations and solidification rate on soundness in casting structure in Al-Si-Cu alloys, International Journal of Cast Metals Research. 23 (2010) 7-22.
- [21] H. Ye, An overview of the development of Al-Si-alloy based material for engine applications, Journal of Materials Engineering and Performance. 12 (2003) 288-297.
- [22] M. Bamberger, I. Minkoff, M. Stupel, Some observations on dendritic arm spacing in Al-Si-Mg and Al-Cu alloy chill castings, Journal of Materials Science, 21 (1986) 2781-2786.
- [23] N.D. DiMatteo, S.R. Lampman, ASM Metals Handbook, Volume 19: Fatigue and Fracture, ASM International, (1996).
- [24] G.E. Dieter, D. Bacon, Mechanical Metallurgy, (1986), McGraw-Hill New York.
- [25] V. Firouzdor, M. Rajabi, E. Nejati, F. Khomamizadeh, Effect of microstructural constituents on the thermal fatigue life of A319 aluminum alloy, Materials Science and Engineering: A. 454 (2007) 528-535.
- [26] H.R. Ammar, A.M. Samuel, F.H. Samuel, Effect of casting imperfections on the fatigue life of 319-F and A356-T6 Al-Si casting alloys, Materials Science and Engineering: A. 473 (2008) 65-75.
- [27] G.R. Halford, Fatigue and Durability of Structural Materials, AsM International, (2006).

- [28] M.J. Caton, J.W. Jones, H. Mayer, S. Stanzl-Tschegg, J.E. Allison, Demonstration of an endurance limit in cast 319 aluminum, *Metallurgical and Materials Transactions: A*. 34 (2003) 33-41.
- [29] P. Li, P. Lee, D. Maijer, T. Lindley, Quantification of the interaction within defect populations on fatigue behavior in an aluminum alloy, *Acta Materialia*, 57 (2009) 3539-3548.
- [30] G. Cole, A. Sherman, Light weight materials for automotive applications, *Materials Characterization*, 35 (1995) 3-9.
- [31] R. MacKay, J. Sokolowski, Comparison between wedge test castings and component engine block casting properties, *International Journal of Metalcasting*. 4 (2010) 33-50.
- [32] L. Dietrich, J. Radziejewska, The fatigue damage development in a cast Al-Si-Cu alloy, *Materials and Design*, 32 (2011) 322-329.
- [33] D. Casellas, R. Pérez, J.M. Prado, Fatigue variability in Al-Si cast alloys, *Materials Science and Engineering: A*. 398 (2005) 171-179.
- [34] L. Viet-Duc, F. Morel, D. Bellett, E. Pessard, N. Saintier, P. Osmond, Microstructural-based analysis and modelling of the fatigue behaviour of cast Al-Si alloys, *Procedia Engineering*, 133 (2015) 562-575.
- [35] H.R. Ammar, A.M. Samuel, F.H. Samuel, Porosity and the fatigue behavior of hypoeutectic and hypereutectic aluminum-silicon casting alloys, *International Journal of Fatigue*, 30 (2008) 1024-1035.
- [36] R. Atwood, S. Sridhar, W. Zhang, P. Lee, Diffusion-controlled growth of hydrogen pores in aluminium-silicon castings: In situ observation and modelling, *Acta materialia*. 48 (2000) 405-417.
- [37] K. Kubo, R.D. Pehlke, Mathematical modeling of porosity formation in solidification, *Metallurgical and Materials Transactions: B*. 16 (1985) 359-366.
- [38] M.J. Caton, J.W. Jones, J.M. Boileau, J.E. Allison, The effect of solidification rate on the growth of small fatigue cracks in a cast 319-type aluminum alloy, *Metallurgical and Materials Transactions: A*. 30 (1999) 3055-3068.
- [39] P. Lee, A. Chirazi, D. See, Modeling microporosity in aluminum-silicon alloys: a review, *Journal of Light Metals*. 1 (2001) 15-30.
- [40] K.D. Carlson, Z.P. Lin, C. Beckermann, G. Mazurkevich, M. Schneider, Modeling of Porosity Formation in Aluminium Alloys, *Materials Science Forum*, Trans Tech Publications, 519 (2006) 1699-1706.

- [41] D.O. Ovono, I. Guillot, D. Massinon, The microstructure and precipitation kinetics of a cast aluminium alloy, *Scripta Materialia*, 55 (2006) 259-262.
- [42] H. Jiang, P. Bowen, J. Knott, Fatigue performance of a cast aluminium alloy Al-7Si-Mg with surface defects, *Journal of Materials Science*, 34 (1999) 719-725.
- [43] M.A. Meyers, K.K. Chawla, *Mechanical Behavior of Materials*, (2009), Cambridge University Press Cambridge.
- [44] American Society for Metals, *ASM Metals Handbook, Volume 11: Failure Analysis and Prevention*, (1986), ASM International.
- [45] M. Bolliger, K. Buxmann, I. Gyongyos, Mould with roughened surface for casting metals, US 4,250,950 (1981).
- [46] D. Nelson, Effects of residual stress on fatigue crack propagation, *Residual stress effects in fatigue*, ASTM International, 776 (1982) 172-194.
- [47] R. I. Mackay, J. Sokolowski, Experimental observations of dendrite coarsening & Al-Si eutectic growth in progressively quenched structures of Al-Si-Cu casting alloys, *International Journal of Metalcasting*, 2 (2008) 57-75.
- [48] R. Mackay, M. Djurdjevic, J. Sokolowski, Effect of cooling rate on fraction solid of metallurgical reactions in 319 alloy, *Transactions of the American Foundry Society and the 104th annual Casting Congress*, (2000) 521-530.
- [49] E.J. Martínez D, M.A. Cisneros G, S. Valtierra, J. Lacaze, Effect of strontium and cooling rate upon eutectic temperatures of A319 aluminum alloy, *Scripta Materialia*, 52 (2005) 439-443.
- [50] J. Jordon, M. Horstemeyer, N. Yang, J. Major, K. Gall, J. Fan, D. McDowell, Microstructural inclusion influence on fatigue of a cast A356 aluminum alloy, *Metallurgical and Materials Transactions: A*. 41 (2010) 356-363.
- [51] C. Muojekwu, I. Samarasekera, J. Brimacombe, Heat transfer and microstructure during the early stages of metal solidification, *Metallurgical and Materials Transactions: B*. 26 (1995) 361-382.
- [52] J.A. Dantzig, M. Rappaz, *Solidification*, (2009), EFPL Press.
- [53] S. Shabestari, M. Malekan, Assessment of the effect of grain refinement on the solidification characteristics of 319 aluminum alloy using thermal analysis, *Journal of Alloys and Compounds*. 492 (2010) 134-142.
- [54] M. Malekan, S. Shabestari, Effect of grain refinement on the dendrite coherency point during solidification of the A319 aluminum alloy, *Metallurgical and Materials Transactions: A*. 40 (2009) 3196.

- [55] M.C. Flemings, Solidification processing, (1974), McGraw-Hill, New York.
- [56] O. Lashkari, L. Yao, S. Cockcroft, D. Maijer, X-ray microtomographic characterization of porosity in aluminum alloy A356, *Metallurgical and Materials Transactions: A*. 40 (2009) 991-999.
- [57] P. Scarber Jr, H. Littleton, Simulating Macro-Porosity in Aluminum Lost Foam Castings, *AFS Transactions*, (2008) 08-145.
- [58] J.G. Kaufman, E.L. Rooy, *Aluminum Alloy Castings: Properties, Processes, and Applications*, (2004), ASM International.
- [59] M. Dash, M. Makhlof, Effect of key alloying elements on the feeding characteristics of aluminum-silicon casting alloys, *Journal of Light Metals*, 1 (2001) 251-265.
- [60] R. Mackay, R. Hausenbusch, J. Sokolowski, Alloying with silicon and copper in aluminum alloys, *Materials Science Forum*, 539 (2007) 392-397, Trans Tech Publications.
- [61] L. Yao, S. Cockcroft, J. Zhu, C. Reilly, Modeling of Microporosity Size Distribution in Aluminum Alloy A356, *Metallurgical and Materials Transactions: A*. (2011) 1-12.
- [62] C. Hallam, W. Griffiths, A model of the interfacial heat-transfer coefficient for the aluminum gravity die-casting process, *Metallurgical and Materials Transactions: B*. 35 (2004) 721-733.
- [63] G. García-García, J. Espinoza-Cuadra, H. Mancha-Molinar, Copper content and cooling rate effects over second phase particles behavior in industrial aluminum-silicon alloy 319, *Materials and Design*, 28 (2007) 428-433.
- [64] K. Gall, N. Yang, M. Horstemeyer, D.L. McDowell, J. Fan, The debonding and fracture of Si particles during the fatigue of a cast Al-Si alloy, *Metallurgical and Materials Transactions: A*. 30 (1999) 3079-3088.
- [65] M. Shneider, W. Schaefer, E. Sjolander, S. Seiffeddine, I. Svensson, Simulation of microstructure and mechanical properties of aluminum components during casting and heat treatment, *IOP Conference Series, Materials Science and Engineering*, 33 (2012).
- [66] F. Lau, W. Lee, S. Xiong, B. Liu, A study of the interfacial heat transfer between an iron casting and a metallic mould, *Journal of Materials Processing Technology*, 79 (1998) 25-29.
- [67] E. Velasco, S. Valtierra, J.F. Mojica, J. Talamantes, S. Cano, R. Colas, Casting-chill interface heat transfer during solidification of an aluminum alloy, *Metallurgical and Materials Transactions: B*. 30 (1999) 773-778.
- [68] M. Taha, N. El-Mahallawy, M. El-Mestekawi, A. Hassan, Estimation of air gap and heat transfer coefficient at different faces of Al and Al-Si castings solidifying in permanent mould, *Materials science and technology*, 17 (2001) 1093-1101.

- [69] M.A. Gafur, M.N. Haque, K.N. Prabhu, Effect of chill thickness and superheat on casting/chill interfacial heat transfer during solidification of commercially pure aluminium, *Journal of Materials Processing Technology*, 133 (2003) 257-265.
- [70] T.S.P. Kumar, K.N. Prabhu, Heat flux transients at the casting/chill interface during solidification of aluminum base alloys, *Metallurgical and Materials Transactions: B*. 22 (1991) 717-727.
- [71] N. El-Mahallawy, A. Assar, Effect of melt superheat on heat transfer coefficient for aluminium solidifying against copper chill, *Journal of Materials Science*, 26 (1991) 1729-1733.
- [72] F. Incropera, D. De Whitt, *Fundamentals of Heat and Mass Transfer*, (1996), New York, NY: John Wiley and Sons.
- [73] W. Griffiths, The heat-transfer coefficient during the unidirectional solidification of an Al-Si alloy casting, *Metallurgical and Materials Transactions: B*. 30 (1999) 473-482.
- [74] W. Griffiths, A model of the interfacial heat-transfer coefficient during unidirectional solidification of an aluminum alloy, *Metallurgical and Materials Transactions: B*. 31 (2000) 285-295.
- [75] S. Kulkarni, K. Radhakrishna, Evaluation of metal–mould interfacial heat transfer during the solidification of aluminium–4.5% copper alloy castings cast in CO₂–sand moulds, *Materials Science-Poland*. 23 (2005) 821-838.
- [76] Y. Heichal, S. Chandra, Predicting thermal contact resistance between molten metal droplets and a solid surface, *Journal of heat transfer*. 127 (2005) 1269.
- [77] G. Wang, E. Matthys, On the heat transfer at the interface between a solidifying metal and a solid substrate, *Melt-Spinning, Strip casting, and Slab casting*, (1996), TMS Pub., Warrendale, PA.
- [78] T. Rajan, K. Narayan Prabhu, R. Pillai, B. Pai, Solidification and casting/mould interfacial heat transfer characteristics of aluminum matrix composites, *Composites Science and Technology*. 67 (2007) 70-78.
- [79] T. Kim, Z. Lee, Time-varying heat transfer coefficients between tube-shaped casting and metal mold, *International Journal of Heat and Mass Transfer*. 40 (1997) 3513-3525.
- [80] K. Ho, R. Pehlke, Mechanism of heat transfer at a metal-mold interface, *Transactions of the American Foundrymens Society*. 92 (1984) 587-598.
- [81] T. Loulou, E. Artyukhin, J. Bardon, Estimation of thermal contact resistance during the first stages of metal solidification process: I-experiment principle and modelisation, *International Journal of Heat and Mass Transfer*. 42 (1999) 2119-2127.

- [82] M. Prates, H. Biloni, Variables affecting the nature of the chill zone, *Metallurgical and Materials Transactions: B.* 3 (1972) 1501-1510.
- [83] K. Ho, R.D. Pehlke, Metal-mold interfacial heat transfer, *Metallurgical and Materials Transactions: B.* 16 (1985) 585-594.
- [84] J.E. Spinelli, I.L. Ferreira, A. Garcia, Evaluation of heat transfer coefficients during upward and downward transient directional solidification of Al–Si alloys, *Structural and Multidisciplinary Optimization.* 31 (2006) 241-248.
- [85] Y. Nishida, W. Droste, S. Engler, The air-gap formation process at the casting-mold interface and the heat transfer mechanism through the gap, *Metallurgical and Materials Transactions: B.* 17 (1986) 833-844.
- [86] M. Trovant, S. Argyropoulos, Finding boundary conditions: A coupling strategy for the modeling of metal casting processes: Part I. Experimental study and correlation development, *Metallurgical and Materials Transactions: B.* 31 (2000) 75-86.
- [87] M. Trovant, S. Argyropoulos, Finding boundary conditions: a coupling strategy for the modeling of metal casting processes: Part II. Numerical study and analysis, *Metallurgical and Materials Transactions: B.* 31 (2000) 87-96.
- [88] C.A. Santos, J. Quaresma, A. Garcia, Determination of transient interfacial heat transfer coefficients in chill mold castings, *Journal of Alloys and Compounds.* 319 (2001) 174-186.
- [89] H.M. Şahin, K. Kocatepe, R. Kayıkcı, N. Akar, Determination of unidirectional heat transfer coefficient during unsteady-state solidification at metal casting–chill interface, *Energy conversion and management.* 47 (2006) 19-34.
- [90] J. Isaac, G. Reddy, G. Sharma, Experimental investigation of the influence of casting parameters on the formation and distribution of air gap during the solidification of castings in metallic molds, *Transactions of the American Foundrymen Society.* 93 (1985) 29-34.
- [91] J. Majumdar, B. Raychaudhuri, S. Dasgupta, An experimental method for measuring mould/metal gap variation with time in a metal casting process, *Journal of Physics D: Applied Physics,* 10 (1977) 1175.
- [92] G. Stolz, Numerical solutions to an inverse problem of heat conduction for simple shapes, *Journal of heat transfer.* 82 (1960) 20-25.
- [93] A.M. Assar, On the interfacial heat transfer coefficient for cylindrical ingot casting in a metal mould, *Journal of Materials Science,* 11 (1992) 601-606.
- [94] C. Kang, Y. Kim, Model experiments for the determination of the heat-transfer coefficient and transition thermal analysis in the direct rolling process, *Journal of Materials Processing Technology.* 84 (1998) 210-224.

- [95] M. Pokorny, C. Monroe, C. Beckermann, L. Bichler, C. Ravindran, Prediction Of Hot Tear Formation In A Magnesium Alloy Permanent Mold Casting, *International Journal of Metalcasting*. 2 (2008) 41-52.
- [96] A. Fardi Ilkhchy, M. Jabbari, P. Davami, Effect of pressure on heat transfer coefficient at the metal/mold interface of A356 aluminum alloy, *International Communications in Heat and Mass Transfer*. 39 (2012) 705-712.
- [97] M. Fackeldey, A. Ludwig, P. Sahm, Coupled modelling of the solidification process predicting temperatures, stresses and microstructures, *Computational materials science*. 7 (1996) 194-199.
- [98] S. Thompson, S. Cockcroft, M. Wells, Advanced light metals casting development: solidification of aluminium alloy A356, *Materials science and technology*. 20 (2004) 194-200.
- [99] B. Zhang, D. Maijer, S. Cockcroft, Development of a 3-D thermal model of the low-pressure die-cast (LPDC) process of A356 aluminum alloy wheels, *Materials Science and Engineering: A*. 464 (2007) 295-305.
- [100] J. Dantzig, S. Lu, Modeling of heat flow in sand castings: Part I. The boundary curvature method, *Metallurgical Transactions: B*. 16 (1985) 195-202.
- [101] K.C. Mills, *Recommended Values of Thermophysical Properties for Selected Commercial Alloys*, (2002), Woodhead Publishing.
- [102] J. Sengupta, S. Cockcroft, D. Maijer, A. Larouche, Quantification of temperature, stress, and strain fields during the start-up phase of direct chill casting process by using a 3D fully coupled thermal and stress model for AA5182 ingots, *Materials Science and Engineering: A*. 397 (2005) 157-177.
- [103] E. Rincon, H. Lopez, M. Cisneros, H. Mancha, M. Cisneros, Effect of temperature on the tensile properties of an as-cast aluminum alloy A319, *Materials Science and Engineering: A*. 452 (2007) 682-687.
- [104] J. Thole, C. Beckermann, Measurement of elastic modulus of PUNB bonded sand as a function of temperature, *International Journal of Metalcasting*. 4 (2010) 7-18.
- [105] E. Rincon, H. Lopez, M. Cisneros, H. Mancha, Temperature effects on the tensile properties of cast and heat treated aluminum alloy A319, *Materials Science and Engineering: A*. 519 (2009) 128-140.
- [106] C. Monroe, C. Beckermann, J. Klinkhammer, Simulation of Deformation and Hot Tear Formation using a visco-plastic Model with Damage, *Modeling of Casting, Welding, and Advanced Solidification Processes-XII*, eds. SL Cockcroft and DM Maijer, TMS, Warrendale, PA. (2009) 313-320.

- [107] A. Hadadzadeh, M.A. Wells, Mathematical modeling of thermo-mechanical behavior of strip during twin roll casting of an AZ31 magnesium alloy, *Journal of Magnesium and Alloys*. 1 (2013) 101-114.
- [108] J. Pavlović-Krstić, R. Bähr, G. Krstić, S. Putić, The effect of mould temperature and cooling conditions on the size of secondary dendrite arm spacing in Al-7Si-3Cu alloy, *Metalurgija*. 15 (2009) 106-113.
- [109] S. Shabestari, M. Malekan, Thermal analysis study of the effect of the cooling rate on the microstructure and solidification parameters of 319 aluminum alloy, *Canadian Metallurgical Quarterly*. (2005) 305-312.